0,4

ISAS - INTERNATIONAL SCHOOL FOR ADVANCED STUDIES

1

Physical and cosmological relevance of rare and extreme sources

Ilaria Cagnoni
International School for Advanced Studies (SISSA-ISAS)
Via Beirut 2-4, 34014 Trieste, Italy.

Supervisors: A. Celotti and M. Elvis

Thesis submitted for the degree of "Doctor Philosophiæ"
October 2001

Physical and cosmological relevance of rare and extreme sources

Ilaria Cagnoni
International School for Advanced Studies (SISSA-ISAS)
Via Beirut 2-4, 34014 Trieste, Italy.

Supervisors: A. Celotti and M. Elvis

Thesis submitted for the degree of "Doctor Philosophiæ"
October 2001

Contents

List of Figures

List of Tables

Chapter 1

Introduction

This introductory chapter is devoted to the presentation of the scientific framework related to this thesis and to the methodology adopted.

1.1 Public data

We start this introduction describing the methodology and the approach we adopted because it is common in all the thesis. In recent years, thanks to the increasing availability of data coming from satellites, surveys projects and pointed observations at different energy bands and thanks to the creation of large databases, an enormous amount of data has become available to the scientific community. The quantity of data is foreseen to greatly increase in the next years thanks to the new X-ray satellites (*Chandra* and *XMM-Newton*), to the ongoing surveys at radio and optical energies and to the international effort aimed at the creation of an optical database containing observations coming from different facilities. These archival data is full of potentialities far from being fully exploited and we decided to make use of it throughout this thesis. The approach adopted is to use sources catalogs derived from public archival data at many different energy bands (X-rays, extreme ultraviolet (EUV), optical, infrared (IR) and radio) to select:
- rare or extreme sources (as we did in the first and second part of this thesis);
- a flux limited sample (second part of this thesis);
- or the multiple detections of a particular source to reconstruct its history (third part of this thesis).

1.2 Scientific framework

We devote this section to a quick introduction of the underlying scientific framework this thesis belongs to. Since most of the work done is related (but not limited) to active galactic nuclei (AGNs) we start with the definition of this class of sources and with a brief overview of the present knowledge of the field.

1.2.1 AGNs unified models

Active Galactic Nuclei are sources characterized by enormous luminosities (up to 10^{48}-10^{49} erg s^{-1}) produced in extremely compact regions ($r < 0.1$ pc). It was indeed the extreme luminosity ($\sim 10^{44}$ erg s^{-1}) generated in the compact core of Seyfert galaxies that made Carl Seyfert (1943) realize that such (active) galaxies formed a distinct class, while optical spectroscopy follow-up revealed the presence of broad ($\sim$ 3000 – 10000 km s^{-1}) and narrow ($<$ 1000 km s^{-1}) emission lines. It became soon clear that such a high luminosity could not be ascribed to stellar nuclear fusion and the most widely accepted scenario is nowadays the extraction of gravitational energy from the gas orbiting near a supermassive ($M > 10^6 M_\odot$, where $M_\odot$ is the solar mass) black hole. The infalling gas looses angular momentum through viscous processes in an accretion disk and dissipates energy radiating in the optical, UV to soft X-ray energy band (e.g. Rees 1984). Such emission is confined in a compact region (e.g. $\sim 10^{15}$ cm for a Seyfert galaxy) thus explaining the observed compact core. To justify the different width of the optical lines, different Doppler broadening for the narrow and broad sets of lines had to be assumed. The easiest way to decrease the Doppler shift from the broad to the narrow lines is to think that they are emitted from gas with different orbital velocity: closer to the central black hole ($\sim 10^{16}$ cm) for the broad line emitting region (BLR) and farther ($\geq 10^{17}$ cm) for the narrow line region (NLR).

Some Seyfert galaxies were observed to lack broad lines in their optical spectra, and the terms Seyfert 1 (or Sy 1) and Seyfert 2 (or Sy 2) were used to indicate objects with or without broad lines. A great improvement in the understanding of Seyfert galaxies was the observation in direct and polarized light of the Seyfert galaxy NGC 1068 (Antonucci & Miller 1985); the broad lines, absent in the spectrum of this Sy 2 appeared when observed in polarized light. This was interpreted as obscuring material intersecting our line of site and hiding the broad line region, revealed only in polarized light because some scattered emission was able to escape the obscuring material and reach us. The cornerstone for unification models was set and the idea

of an optically thick obscuring torus composed by dust and gas and able to absorb the IR to soft X-ray emission of the central parts of the AGNs (and re-radiate in the IR through dust emission) started to be used to explain the difference between Sy 1s and Sy 2s. After the discovery of Seyfert galaxies a large variety of objects (similar to Seyfert galaxies for their high luminosity produced in a compact region) with different optical, radio or X-ray properties was found. It was soon clear that a similar unification approach, as the one adopted by Antonucci & Miller (1985) for Seyfert galaxies, was useful to make some order in the "chaos" of AGN taxonomy.

Unified models for AGNs have an underlying basic assumption: AGNs have less intrinsic diversity than we observe and the observed variety is the result of a small number of intrinsic differences combined to "apparent" differences that can be traced back to physically unimportant parameters (e.g. orientation). The goal of unification models is to discover the minimum number of intrinsic physical parameters that can explain the observations.

The first difference among AGNs that unification models have to face is the spread in radio and optical luminosity (Figure 1.1), such that some AGNs are addressed as radio loud (RL) and others as radio quiet (RQ)[1]. Even if recent results (Lacy et al. 2001) suggest a continuous sequence from RL to RQ AGNs, we adopt such a classification in this thesis. The SED of RL and RQ AGNs is similar except for the importance of the radio emission (e.g. Figure 1.1) while the most striking difference among the two classes is the presence of collimated (Mpc-scale long) jets in RL objects.

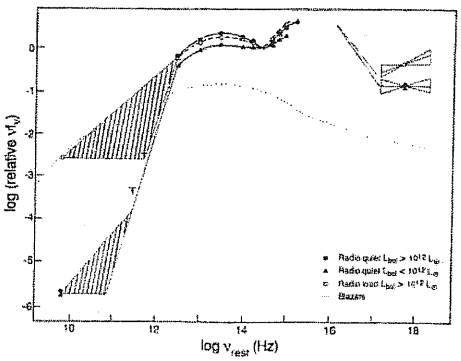

Figure 1.1: (From Sanders et al. 1989) Continuum spectral energy distribution of RL and RQ PG quasars.

To give a flavor of unification among AGNs, we summarize a view of one possible extremely simplified unification scheme in Table 1.1 based on the presence/absence of a jet and on an obscuring torus (for an AGN unification

[1]The dividing line is usually set to $F_{5GHz}/F_B = 10$ (Kellermann et al. 1980), where F_{5GHz} is the radio flux measured at 5 GHz and F_B is the optical flux in the B band.

Table 1.1: A possible unification scheme.

Radio properties	Orientation Face-On	Edge-on
Radio Quiet	Seyfert 1	Seyfert 2
	QSO	QSO-2s?
		ULRIG?
Radio Loud	BL Lac	FRI
	BLRG	NLRG
	Quasar	FRII

review see e.g. Urry & Padovani 1995 and Antonucci 1993).

As proposed by Antonucci & Miller (1985) for Sy galaxies, in this scheme Seyfert 1s and broad line radio galaxies (BLRGs) differ from Seyfert 2s and narrow line radio galaxies (NLRGs) by the orientation of the obscuring torus which hides the emission from the central regions (accretion disk and BLR) with the effect of absorbing the broad lines in the optical spectrum. BL Lacs and quasars correspond to low and high luminosity (Fanaroff-Riley I and II, or FRI and FRII; Fanaroff & Riley, 1974) radio galaxies, FRI and FRII respectively, seen with the jet pointing in our direction.

The real picture is much more complex and such simple unified models have troubles explaining many observed features. In the next paragraphs I will only address the problems relevant for this thesis.

An example of weakness in unified models of AGNs is the number density of QSO-2s, which have been elusive for many years but are now starting to be found in surveys (e.g. Boyle et al. 1998; Franceschini et al. 2000; Della Ceca et al. in preparation); however doubts on their very existence are often cast (e.g. Halpern, Turner & George, 1999) and their observed number density is far lower than what models need to reproduce the number counts in the $2-10$ keV band (e.g. Gilli, Risaliti & Salvati 1999; Miyaji, Hasinger & Schmidt, 2000).
Could this be due to a luminosity dependent thickness of the torus?
Or to a decoupling of optical and X-ray spectral properties?
This last hypothesis is suggested by the optical identification of the $5-10$ keV HELLAS sources with a flattest X-ray spectra (usually attributed to the effect of neutral hydrogen absorption); instead of being all optical type 2 objects, some of them were identified with blue QSO with broad optical emission lines (La Franca et al. 2001), the prototype of unabsorbed type 1 AGNs in unification models.

Could this be due to a varying composition of the absorbing medium?
Recently Maiolino et al. (2001) found evidence for a lower than Galactic dust (responsible for optical absorption) to gas (responsible for X-ray absorption) ratio in a number of AGNs with extremely low X-ray over optical flux ratios.
Is the composition of the obscuring torus different in different object? Why?
Do objects with higher than Galactic dust to gas ratios exist?

Another recently debated issue in unified models is the accretion process powering AGNs. The standard picture is accretion through an optically thick and geometrically thin accretion disk (Shakura & Sunyaev, 1973), but this is not the only theoretically allowed mechanism (e.g. Chen et al. 1995). For lower accretion rates the radiative efficiency is much lower than the thin disk case. The energy is advected inward before it can escape and the disk "inflates" becoming geometrically thick (Narayan & Yi, 1994): such an accreting scenario is called advection dominated accretion flow (ADAF). The ADAF mechanism can explain the spectra of some Galactic black hole X-ray binaries, which are thought to be a scaled down version of Seyfert galaxies and QSOs (e.g. Esin et al. 1998) and evidences for such process acting in AGNs are looked for (e.g. Narayan et al. 1998; Lu & Yu 1999; Di Matteo et al. 2000).
Do AGNs accrete via the ADAF mode?
What fraction of them?

Also on the blazars side unification models have unanswered questions. The BL Lacertae objects, when first selected at radio or X-ray energies (e.g. Stickel et al. 1991, Wolter et al. 1991) seemed to belong to two different classes of sources, but few years later Giommi and Padovani interpreted such a duality as the result of selection effects (Giommi & Padovani 1994). Radio selected and X-ray selected BL Lacs, together with quasars, seem to form a continuous sequence of blazars with SED progressively shifted toward higher energies with decreasing source luminosity (e.g. Figure 2.2 taken from Fossati et al. 1998).
Which physical parameter is responsible for such a shift in the SED with source luminosity?
How far does this blazars sequence extend?
Do all blazars follow such a trend or do bright but low energy peaked BL Lacertae exist?

To address these (but not only, see § 1.2.2, § 2.1 and § 2.2) issues, we

started our study of sources with extreme values of X-ray over optical flux ratios (i.e. *ROSAT* blank field sources).

Another big problem related to unification models of AGNs is evolution.
Is the unification scheme static or does it change with cosmic time?
Are the various classes of AGNs related by orientation effects and physical parameters only or do they evolve one into the other one?
A particularly debated subject is the apparently different evolution of X-ray and radio selected BL Lacertae objects (Wolter et al. 1994; Stickel, Meisenheimer & Kuehr, 1994)
Do X-ray and radio selected objects have a different evolution? Why?
Do high redshift BL Lac exist? In which number?

To investigate these (and other, see § 9) questions from a new point of view, we started the selection of a faint optical blazar sample, subject of the second part of the thesis, while the third part is devoted to the detailed study of one of the best known representatives of the BL Lac class: MRK 421.

1.2.2 Relevance of this thesis outside the AGN field

The work presented here is potentially relevant not only in the AGN field, but it could also have a strong cosmological importance. Sources with extreme X-ray over optical flux ratios could be failed clusters or high redshift and bright clusters of galaxies (§ 2.1).
Failed clusters are large overdensities of matter collapsed without forming galaxies and could be present only in a top-down (smaller scale structures formed from the division of larger scale structures) scenario for the Universe formation and the finding of even only one example of such sources could mine the widely accepted hierarchical clustering model (large scale structures formed from the merger of smaller scales ones; e.g. Peebles 1980) (see § 2.2).
The number density of high redshift and luminous clusters of galaxies, on the other side, is a powerful constraint for the matter density in the Universe (§ 2.2 and § 7.4 for a detailed discussion).

Other fields that might be involved in the results of this thesis are the gamma ray bursts (GRB) models and neutron stars physics, as explained in § 2.1 and § 2.2.

The next section is dedicated to the presentation and discussion of the potentiality offered by the study of rare of extreme sources, a common subject to all the parts of this thesis.

1.3 Importance of rare and extreme sources

The study of rare sources could appear, at first sight, an irrelevant subject and in fact rare objects are usually neglected in statistical studies, mainly for the difficulty of studying them. For example the same kind of sources presented in the first part of this thesis, *ROSAT* "blank field sources" were found in X-ray surveys (e.g. Bade et al., 1995) but being optically faint and thus "difficult" to study, they were not further investigated. It is widely known that some classes of rare objects, such as high redshift and massive clusters of galaxies are key tools for cosmological models (§ 7.4 and 7.4 for a discussion), but other classes of rare sources could prove as important. Besides the always attractive possibility of discovering among rare objects exotic sources challenging or mining our present understanding of the astrophysical processes and emission mechanisms, rare sources could be theoretically predicted but never observed sources (e.g. isolated old neutron stars accreting from interstellar matter) or the most extreme representatives of known classes of objects. Being extreme, they could represent a test for theoretical models and provide example of extreme emission processes or physical conditions.

All the sources we investigated in this thesis are rare and extreme: blank field sources were selected on the basis of their extreme X-ray over optical flux ratio and constitute $< 0.1\%$ of all the sources in the X-ray catalog used for their selection (§ 2.3) and blazars are a rare ($\sim 5\%$) and extreme variety of AGNs (e.g. the most variable, the most polarized and with emission on the broadest energy band, Urry & Padovani 1995).

We investigated in this thesis a minority of sources, but we think that important consequences for cosmology and for the physics of AGNs can derive from such a study.

1.4 Scheme of the thesis

The work presented in this thesis is grouped into three main areas:
the study of sources with extreme X-ray over optical flux ratios in Part I;
the selection of a faint blazar sample in the optical band in Part II
and the detailed spectral and variability study of the BL Lacertae objects MRK 421 in the EUV band in Part III.

Part I

ROSAT blank field sources

Chapter 2

Nature and importance of *ROSAT* blank field sources

The X-ray sky is not as well known as sometimes thought. There might exist classes of "common" sources though to be "rare" because of the difficulty of finding them. A surprisingly high fraction of estreme X-ray loud sources ($\sim 7-8\%$ of ROSAT high Galactic latitude sources at all fluxes: Bade et al. 1995; Schmidt et al. 1998) has a still mysterious nature. We call 'blank field sources' or 'blanks' all the bright X-ray sources ($F_X > 10^{-13}$ erg cm^{-2} s^{-1}) with no optical counterpart on the Palomar Sky survey (to O=21.5[1]) within their 39″ (99%) radius error circle. For comparison, at these X-ray fluxes a normal type 1 AGN should appear in the Palomar with $O \sim 18$. The nature of these sources has never been systematically investigated before, and their nature is still mysterious. We decided to select these sources and to study them to understand their nature because of the important cosmological and astrophysical consequences that could derive from their identification.
This chapter introduces *ROSAT* blank field sources, reviews the open possibilities on their nature (§ 2.1) and the important consequences that could derive from the identification of these extreme and rare sources (§ 2.2). We end this chaper describing the selection criteria used for the definition of the sample (§ 2.3). We continue this part of the thesis presenting the analysis of *ROSAT* archival data in § 3 and the results of the new data we obtained both in optical and IR (§ 4) and in X-rays (§ 6). We conclude with a discussion on the results we found (§ 7).
We will use H_0=75 km s^{-1} Mpc^{-1} and $q_0 = 0.5$; errors represent 1σ confidence levels, unless explicitly stated otherwise.

[1] O-band effective wavelength = 4100 Å; passband = 110 Å

2.1 Nature of *ROSAT* blank field sources

Blank field sources are extreme X-ray loud objects: the only extragalactic population that can reach such f_X/f_V are BL Lacertae objects, as evident from the Maccacaro et al. (1988) normograph. We reported in Figure 2.1 such normograph showing (red line) the minimum f_X/f_V implied by the adopted selection criteria.

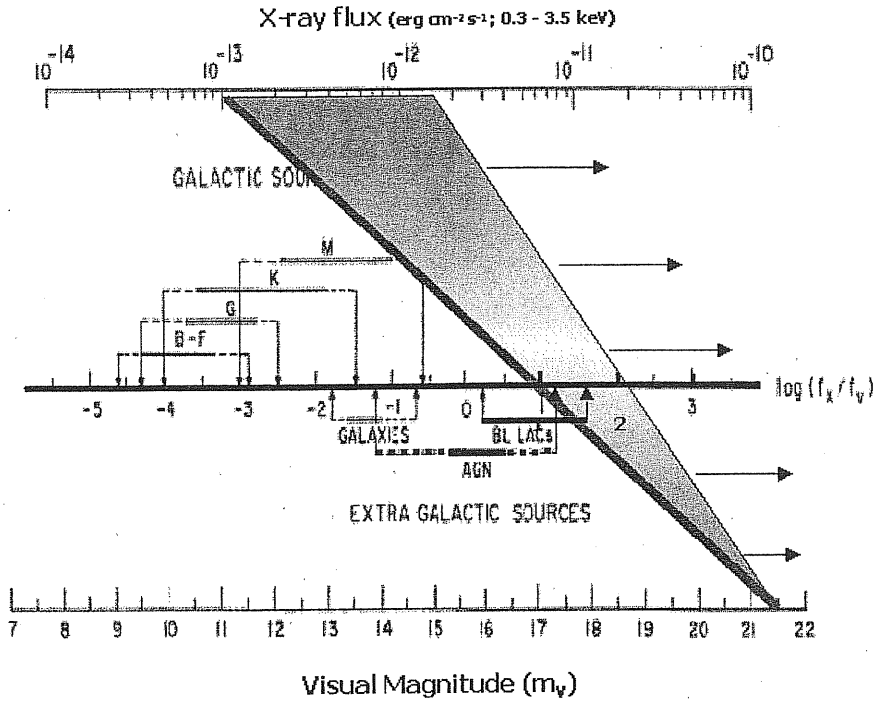

Figure 2.1: Maccacaro et al. 1988 normograph with the red line showing the minimum f_X/f_V for our blank field sources.

Normal quasars and AGN have 0.1< f_X/f_V <10; normal galaxies have only $10^{-2} < f_X/f_V < 10^{-1}$; while a high luminosity cluster of galaxies ($L_X = 10^{45}$ erg s^{-1}) would have a first ranked elliptical with $L_{gal} = 10L^*(= 10^{11.5}L_\odot)$ giving $f_X/f_V \sim 8$. None of these reach the $f_X/f_V > 10$ of the blank field sources we have found. The only known class of X-ray emitting objects that can reach such extreme f_X/f_V are BL Lacertae objects, which can have f_X/f_V up to ~ 35.

Besides "normal" BL Lacertae objects, which can be found for $f_X/f_V < 35$, there are some other interesting possibilities regarding the nature of blank field sources and they are:

1 **Extreme BL Lacertae objects**, to reproduce the most extreme f_X/f_V allowed by the blank field sources (Figure 2.1) a BL Lac object with a

SED peaking at energies higher than the *ROSAT* band is needed. This peak could be both the synchrotron one and some extreme BL Lacs are known to have such properties (Costamante et al. 2001) or the inverse Compton one. No examples of such extreme BL Lacs are known so far, but the study of *ROSAT* blank field sources could potentially discover them.

2 **Isolated Old Neutron Stars** (IONS), dead neutron stars brought back to life by accretion from the interstellar medium (e.g. Treves et al. 2000). Being nearby ($\sim$ 100 pc) these will be quasi-isotropically distributed on the sky. IONS are expected to have $F_X/F_V > 100 - 1000$ (Maoz, Ofek & Shemi, 1997). We would expect extremely soft X-ray spectra and emission in the UV. The expected number counts for IONS are highly uncertain, ranging from $\sim 1/\mathrm{deg}^2$ (Madau & Blaes 1994) to much smaller values (e.g. Colpi et al. 1998).

3 **Peculiar AGNs**

Normal type 1 AGNs with $F_X > 10^{-13}$ erg cm^{-2} s^{-1} have $O \sim 18$ and could be included among blank field sources if their O-band absorption is $A_O > 3.5$ mag, which corresponds to a local $N_H > 4 \times 10^{21}$ cm^{-2}. Possibilities for absorbed AGNs still visible in *ROSAT* PSPC with $F_X > 10^{-13}$ erg cm^{-2} s^{-1}are:

3a Quasar-2s, i.e. high luminosity, high redshift, heavily obscured quasars, the bright analogs of the well known Seyfert 2s at $z >> 0.5$. We would expect: (a) strong optical reddening; (b) soft X-ray absorption (although lower than that measured in the source frame); (c) recovery of the X-ray intrinsic emission in the PSPC energy range (giving flat PSPC slopes). Quasar-2s should then have flat PSPC spectra and an observed soft X-ray to 2500 Å ratio which will be enhanced by the redshift K-correction. QSO-2s are visible in the PSPC because their redshift has the apparent effect of lowering the absorption. We simulated the Quasar-2 case assuming an absorbed ($N_H = 5 \times 10^{22}$ cm^{-2} in the rest frame) power law model ($\Gamma = 1.7$) at z=1.0 with an unabsorbed $L_{(0.5-2.4\mathrm{keV})} = 1.8 \times 10^{45}$ erg s^{-1}. We also included a neutral iron line at $E_{Fe} = 6.4$ keV and equivalent width of 0.15 keV in the rest frame. The simulated QSO-2 is detected by the *ROSAT* PSPC with a count rate of ~ 0.01 counts s^{-1} corresponding to a 0.5-2.4 keV flux of 2.57×10^{-13} erg cm^{-2} s^{-1}, and would thus be included among blank field sources.

3b Low Mass Seyfert 2 (LMSy 2), i.e. Seyfert 2 galaxies powered by a relatively low mass obscured black hole ($M_{bh} \sim 10^7 M_\odot$). These would

be the obscured analogs of the Narrow Line Seyfert 1s. Their low mass would shift the peak of the thermal big blue bump disk emission ($T_{peak} \sim M_{bh}^{1/4}$) up to peak around 100 eV. As a result the Seyferts spectrum would be enhanced in the soft X-ray band and suppressed in the optical. (c.f. the NLSy1 RE 1034+396, Puchnarewicz et al. 1995; 2001). Obscuration, even by large amount of molecular matter and cold gas ($N_H = 10^{22} - 10^{23}$ cm^{-2}), would still allow the detection of the intrinsically strong soft X-ray source emission, but would harden the observed X-ray spectra.
We simulated the LMSy2 case assuming an absorption of 5×10^{22} cm^{-2}, a thermal component of kT = 150 eV, a power law with a photon index slope of 2.2. We normalized the model to have a ratio between the thermal and power law component matching what observed in Narrow Line Sy 1s (Nicastro, Fiore & Matt, 1999) and to have an unabsorbed luminosity of $L_{(0.5-2.4\mathrm{keV})} = 4\times10^{42}$ erg s^{-1} at local redshift (z=0.002 assumed to derive the luminosity). The simulated LMSy2 is detected in the *ROSAT* PSPC with a count rate of 0.015 counts s^{-1} corresponding to a 0.5 -2.4 keV flux of 2.4×10^{-13} erg cm^{-2} s^{-1}.
AGNs with no big blue bump, e.g. ADAFs in which the radiation is inefficient (Narayan & Yi, 1994).

4 Unusual clusters

4a High Redshift Clusters of Galaxies in order for the 4000 Å break to be shifted at longer wavelengths than the Palomar O band and thus for the cluster to be fainter than O=21.5, and have $f_X/f_V > 10$, the redshift has to be larger than ~ 0.4.

4b Failed Clusters (Tucker, Tananbaum & Remillard 1995) in which a large overdensity of matter has collapsed but has not formed galaxies

5 Extreme variables

5a X-ray Bursts, short lived X-ray flares, which may be afterglows of gamma ray bursts.

5b Exotic and strongly variable sources, which were caught very bright in the ROSAT WGACAT, and very faint in the Palomar.

Quite possibly the class of blank field sources contains examples of several, or all, of these objects.

2.2 Importance of blank field sources

The possibility of identifying blank field sources with objects listed above would make the study of this minority population a subject of primary importance in cosmology and astrophysics.

1 BL Lacertae objects:

"normal" BL Lacs are expected for low f_X/f_V, but given the range of f_x/f_V spanned by blank field sources (Figure 2.1) more extreme BL Lacertae objects, with the SED peaking at energies higher than the *ROSAT* band are needed. Looking at Fossati et al (1998) blazar sequence (Figure 2.2), this would mean to "stretch" the sequence toward higher energies (BL Lacs with the synchrotron peak at $1 < E \leq 10$ keV) or toward lower energies (BL Lacs with the inverse Compton peak at $1 < E \leq 10$ keV). While few example of extreme BL Lacertae of the first type are known to date (Costamante et al. 2001), no example of the second kind have ever been found. According to Fossati's sequence, they would be extremely luminous sources and the high cut in X-ray flux adopted for our sources is suitable for their selection.

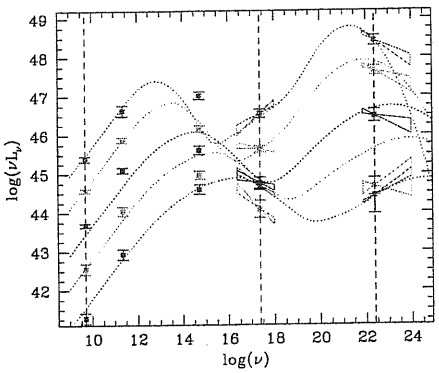

Figure 2.2: (From Fossati et al. 1998) blazars average SEDs with analytic SEDs superimposed

2 Isolated Old Neutron Stars:

Blank field sources could be identified with old isolated neutron stars, a very actively sought but still elusive class of sources. The search for IONS has produced a half a dozen strong candidates (Stocke et al. 1995; Walter, Wolk & Neuhauser 1996; Haberl et al. 1997; Haberl, Motch & Pietsch 1998; Schwope et al. 1999; Motch et al. 1999, Haberl, Pietsch & Motch 1999), but none of these can be unambiguously claimed as an accreting, isolated neutron star, so that the ex-

istence of this class of sources is not yet observationally proved. The expected number of IONSs depends strongly on the properties of their progenitors (young neutron stars in the pulsar phase), such as the velocity distribution and the magnetic field decay. These are both subjects of great current interest in pulsar physics. So the spatial density, or an upper limit, of IONSs can be used to constrain neutron stars physics (e.g. Colpi et al. 1998; Livio, Xu & Frank, 1998; Popov et al. 2000).

3 Peculiar AGNs:

3a If blank field sources are identified with obscured AGNs, such as type 2 QSOs or Low Mass Sy2s (option 2 of the list above), they would have important consequences on the unified models of AGNs and on the cosmic X-ray background models. It is widely accepted nowadays that absorbed AGNs play a key role in the production of the cosmic X-ray background above ~ 2 keV and should be the site where a large fraction of the energy of the universe is generated (Fabian & Iwasawa 1999). Low Mass Seyfert-2 galaxies and QSO-2s, in particular, are the "missing links" of the unifying models of AGN (Urry & Padovani 1995) and their existence is still debated (e.g. Halpern, Turner & George 1999).

The existence of a large number of QSO-2s is also necessary for the models of synthesis of the X-ray background with AGN to reproduce the observed number counts at bright fluxes (Comastri et al. 2001, Gilli, Salvati & Hasinger 2001). Thus proof of their existence and a knowledge of their number density is fundamental to our knowledge of the X-ray sky.

3b Advection dominated accretion flows (ADAF), are one of the possible scenarios for the accretion process which is thought to power the AGNs (e.g. Narayan & Yi, 1994). In an ADAF most of the energy is stored in the gas and advected toward the center and only a small fraction is radiated. The result is a suppression of the optical-UV-EUV emission (the so called Big Blue Bump, BBB) (e.g. Figure 2.3).

The ADAF model provide good fit to the spectra of Galactic black holes X-ray binaries (BHXBs), which are believed to be a low-mass accretion version of Seyfert galaxies and QSOs. If this is true some Sy and/or QSO could be accreting material via the ADAF mode and one example of this could be Sagittarius A* (Narayan et al. 1998). Finding ADAFs among blank field sources could strengthen the AGN-BHXRB connection and could be important in determining how important and

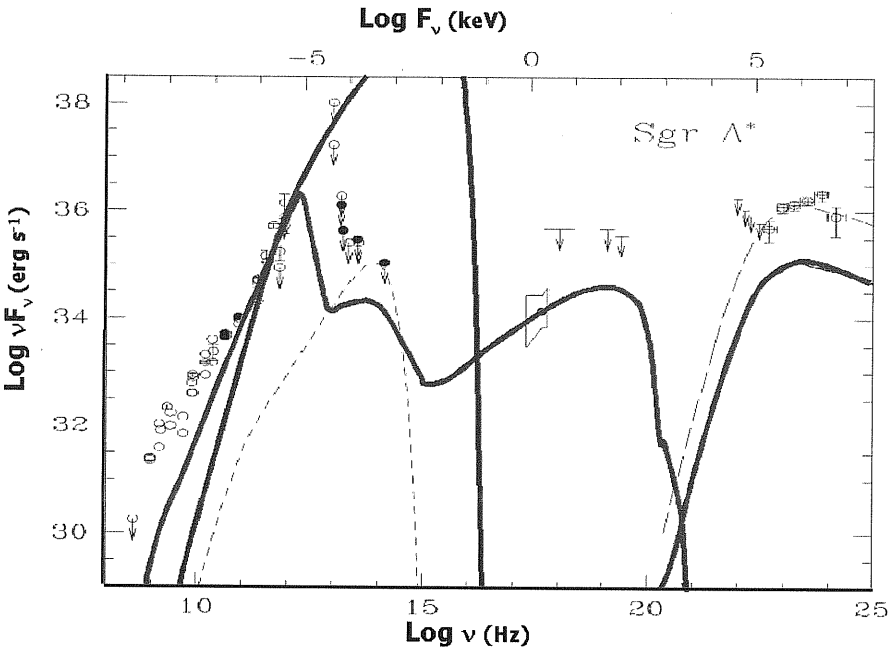

Figure 2.3: Example of ADAF emission (red) compared to the standard Shakura-Sunyaev (1973) thin disk emission (blue).

frequent is the ADAF accretion in nature.

4 Unusual clusters:

4a High luminosity, massive high redshift clusters of galaxies are crucially important tools in cosmology. Their distribution and evolution is fully determined by the spectrum of primordial perturbations and cosmological parameters Ω_0 and Λ (e.g. Press & Schechter 1974). In particular, models of low Ω universe (with or without cosmological constant) predict a higher density of massive clusters at high redshifts than the high Ω models (e.g. Henry 2000, Borgani & Guzzo 2001). The space density of high luminosity high redshift clusters will crucially constrain the cosmological parameters.

A sample of high redshift clusters is also the only means of determining the evolution of the clusters X-ray luminosity function (e.g. Rosati et al., 1998) and would greatly improve any search for evolution in the luminosity-temperature ($L_X - T$) relation, which is related to physical mechanisms of cooling and heating in the central cluster region (e.g. Tozzi & Norman, 2001). Since the statistics is very scanty, adding one more high z high L cluster would greatly improve such studies.

Only few bright high redshift clusters have been found so far (e.g. in

the EMSS, Gioia & Luppino 1994; in the RDCS Rosati et al. 1999, Della Ceca et al. 2000; in the WARPS Ebeling et al. 2000) and only 11 of them at $z > 0.5$ have a measure of their temperature (e.g. Della Ceca et al. 2000, Cagnoni et al. 2001, Stanford et al. 2001).
Using 'blanks' to locate high z clusters of galaxies efficiently is a promising path to pursue.

4b The existence and number-density of failed cluster (Tucker, Tanambaum & Remillard 1995) is connected to the efficiency of galaxy formation, which relates to and potentially constrains a number of interesting questions such as: the spectrum of the fluctuations that gave rise to galaxies, the baryonic or non-baryonic nature of dark-matter, the value of Ω and the relative distribution of dark and baryonic matter. The theory of galaxy formation requires that galaxies form from clouds of gas with cooling time shorter than the Hubble time. This implies a protogalactic mass $< 10^{12} M_{\odot}$ (e.g. White & Frenk 1991 and references therein); in principle more massive clouds, with a cooling time longer than the Hubble time could have never collapsed to form stars in appreciable number. The result would be a large cloud of gas with no visible galaxies.
The discovery of even only one failed cluster among our blank field sources would pose serious difficulties for the hierarchical clustering formation, which does not predict their existence and would favor a top-down scenario.

5 Extreme variables:

5a Popular Gamma Ray Bursts (GRBs) scenarios such as binary coalescence of compact stars (e.g. Janka & Ruffert, 1996) or collapsars (e.g. Hartmann & MacFadyen, 1999) predict strongly collimated flows, which should also lead to strongly collimated bursts and afterglow emission. If afterglows turn out to be less beamed than GRBs, then we expect to find a higher rate of afterglows than GRBs and this rate depends on the beaming angle. This possibility can be tested with a search for afterglows fortuitously detected during *ROSAT* PSPC pointings (e.g. Greiner et al. 2000 for a systematic search for GRBs afterglows in the *ROSAT* All-Sky Survey, RASS). The *ROSAT* lightcurves of GRB afterglows could also constrain the the X-ray flux decaying rate and check if it is consistent with the power law slope of $\sim 1.0 - 1.5$ seen for the brighter *Beppo-SAX* afterglows (Frontera et al. 2000).

5b The remaining open possibility of highly variable sources could also bring the discovery of exotic objects and it is extremely interesting too.

2.3 Sample selection

To define our sample of 'blank field sources' we searched the *ROSAT* PSPC "WGACAT95" (or simply WGACAT, White Giommi & Angelini 1995), a catalog containing a total of $\sim 62,000$ sources generated from *ROSAT* PSPC pointed observations using a sliding cell, detect algorithm. We used the following selection criteria:

1. bright X-ray sources with $f_X > 10^{-13}$ erg cm^{-2} s^{-1};
2. well detected with a signal to noise ratio greater than 10 and a quality flag[2] greater than 5;
3. high Galactic latitude ($|b| > 20°$);
4. not within $2''$ of the target position (at which point the source density reaches the background level) to select only random, serendipitous sources;
5. location in the 'inner circle' of the PSPC ($r < 18'$) to have smaller positional error circles;
6. north of $\delta = -18°$ in order to have measurements in the Automated Plate-measuring Machine (APM) catalog of the POSS (McMahon & Irwin 1992);
7. unidentified, with WGACAT class= 9999 and no SIMBAD or NASA Extragalactic Database identification.

The first six criteria selected 1624 sources ($\sim$ 3% of the total). Since these sources were selected purely on their X-ray properties, they form a well defined sample from which to study the incidence of minority X-ray populations, including any blank field source. Adding the requirement that a source be unidentified left 940 X-ray sources that could be examined for having extreme X-ray over optical flux ratios. We than searched the APM catalog of objects detected on the Palomar Sky Survey for X-ray sources without any optical counterpart in the O filter (to O=21.5) in a radius of $26''$, which corresponds to about 95% confidence for X-ray sources within $18'$ of the PSPC detector center (Boyle et al. 1995).

We note that with a B band (similar to the Palomar O-band) source density of 1000-2000 src deg^{-2} at $B \sim 21.5 - 22$ (e.g. Prandoni et al. 1999; Huang et al. 2001) there is a $\sim 15 - 35\%$ for each PSPC $26''$ error circle [3] of

[2] Since the sliding cell algorithm is sensitive to point sources, it can find spurious sources where extended emission is present. WGACAT includes a quality flag, DQFLAG, that notes dubious detections based on a visual inspection of the fields.

[3] $\sim 36 - 74\%$ when using the $39''$ 3σ radius error circle (see below).

containing a source by chance. This implies than many other PSPC sources would be 'blanks' if we had a smaller uncertainty on the X-ray position. The *ROSAT* HRI, thanks to its smaller positional uncertainty, would be a better choice for the selection of a sample of blank field sources, but no HRI catalogs were available when this project was started.

The selected sample consists of 81 members listed in Table 2.1. After a visual inspection 10 of these sources proved to be false due to limitations of the detection algorithm; false sources can be false detections near to bright sources (Fig. 2.4 right) or detections close to the inner circle boundary due to the spread of a bright source falling in the outer circle (Fig. 2.4 left). The final sample is thus composed of 71 sources.

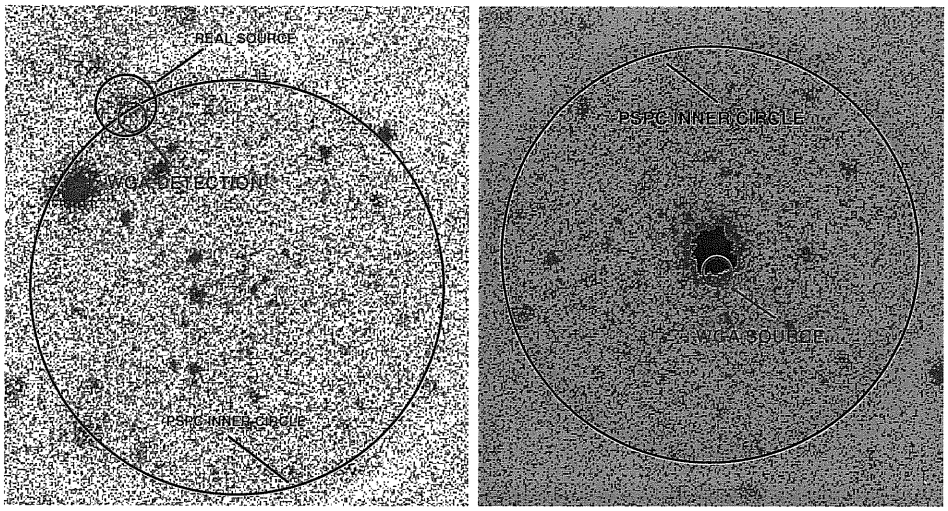

Figure 2.4: Example of two WGACAT false sources (see text)

On closer inspection some of the 71 *ROSAT* fields were found to have WGACAT coordinates not in agreement with other position estimates and in some cases the displacement was larger than the 26″ radius error circle used for the cross-correlation. Some of our blank field sources were thus false blank: no optical counterparts were found because of the wrong X-ray positions. This shift in WGACAT coordinates is related to an error in converting the header of the old format event files into RDF format; this error caused an offset in the source declination up to 1′. These problems were at the time already solved in Revision.2 of *ROSAT* PSPC data, available in the HEASARC database.

2.3.1 Revised Sample

In order to quantify how many of the 71 sources had WGACAT coordinates with an offset $\geq 26''$ we used the incomplete Galpipe catalog (Fabbiano et

al. in preparation) and, found improved Revision.2 coordinates for 54 of the 71 blank field sources (76% of the sample). Out of these 54 sources, 39 have a shift between WGACAT and Galpipe positions smaller than 26″ the WGACAT position (Table 2.1).[4]

Table 2.1: The 81 sources selected from WGACAT.

Source name (1WGA J)	WGACAT coords Ra Dec (J2000)	GALPIPE coords Ra Dec (J2000)	shift (″)	WGACAT95 problem?[a]	false source?
0315.7-5528	03 15 46.3 -55 28 02	3 15 47.6 -55 28 55.4	59.6	Y (wp701036a01)	-
0313.5-5525	03 13 34.5 -55 25 39	3 13 33.5 -55 26 38.4	77.5	Y (wp701036a01)	-
0454.9-5323	04 54 57.7 -53 23 45	4 54 58.0 -53 24 20.8	49.6	Y (wp600436n00)	-
0452.9-5313	04 52 55.4 -53 13 45	4 52 55.1 -53 14 19.6	51.5	Y (wp600436n00)	-
0453.0-5312	04 53 05.0 -53 12 41	4 53 05.1 -53 13 27.5	65.9	Y (wp600436n00)	-
0514.1-4825	05 14 11.4 -48 25 38	5 14 11.3 -48 26 05.9	40.7	Y (wp800368n00)	-
0511.6-4500	05 11 36.3 -45 00 34	– –	–	-	Y
0512.6-4448	05 12 39.1 -44 48 40	– –	–	-	-
0439.5-4329	04 39 35.0 -43 29 25	4 39 34.8 -43 29 22.3	2.7	-	-
0055.6-3725	00 55 41.5 -37 25 27	– –	–	-	Y
0323.4-3656	03 23 29.3 -36 56 43	3 23 29.0 -36 56 28.1	15.5	-	-
0335.4-3449	03 35 24.8 -34 49 51	3 35 23.6 -34 49 39.6	14.3	-	-
0441.0-1616	04 41 05.2 -16 16 20	4 41 05.1 -16 16 13.7	6.3	-	-
0303.3-1530	03 03 20.6 -15 30 01	3 03 20.8 -15 30 55.7	55.4	Y (wp800566n00)	-
0152.6-1358	01 52 40.8 -13 58 21	1 52 42.0 -13 58 01.7	27.6	-	-
0152.7-1357	01 52 43.7 -13 57 16	1 52 44.0 -13 57 16.7	4.36	-	-
0153.1-1351	01 53 11.1 -13 51 11	1 53 10.8 -13 51 01.7	9.8	-	-
0953.7-0453	09 53 46.0 -04 53 39	9 53 46.2 -4 53 34.7	5.8	-	-
1204.7-0321	12 04 44.8 -03 21 39	– –	–	-	-
0516.7-0012	05 16 46.3 -00 12 26	5 16 46.5 -00 12 37.7	12.1	-	-
0515.1+0001	05 15 06.5 +00 01 31	5 15 08.5 00 01 37.2	30.6	-	-
1235.3+0044	12 35 23.1 +00 44 10	12 35 23.5 00 43 58.2	13.5	-	-
1228.4+0141	12 28 29.8 +01 41 55	12 28 29.2 01 41 44.7	13.0	-	-
1204.6+0153	12 04 37.5 +01 53 06	– –	–	-	Y
1150.4+0156	11 50 24.5 +01 56 11	– –	–	-	-
1204.3+0157	12 04 20.2 +01 57 48	– –	–	-	Y
1218.0+0343	12 18 03.0 +03 43 08	– –	–	-	Y
1218.1+0551	12 18 11.8 +05 51 26	12 18 12.1 05 51 19.0	9.7	-	-

[4]Even if ∼ 30% of the sources in our sample have an offset > 26″ between WGACAT and Galpipe positions, this does not mean that 30% of all WGACAT sources have such a large positional error. In fact only 431 observations out of 3644 (∼ 12%) were affected by this problem.

Table 2.1: The 81 sources selected from WGACAT.

1420.0+0625	14 20 05.2 +06 25 10	14 20 05.6 06 25 25.0	16.6	-
1220.3+0641	12 20 18.5 +06 41 27	12 20 18.1 06 41 16.0	11.1	-
1416.2+1136	14 16 12.9 +11 36 05	14 16 13.2 11 36 11.7	6.7	-
1416.2+1146	14 16 15.1 +11 46 23	14 16 15.7 11 46 34.1	11.1	-
1025.9+1239	10 25 57.7 +12 39 46	– –	–	-
1214.4+1316	12 14 28.0 +13 16 39	12 14 27.8 13 16 31.2	8.3	-
0420.6+1453	04 20 36.1 +14 53 52	– –	–	Y (wp200441)
0426.1+1655	04 26 07.5 +16 55 08	04 26 07.3 16 55 07.2	2.71	-
0432.4+1723	04 32 29.5 +17 23 38	04 32 29.6 17 23 47.8	10.0	-
0257.8+1944	02 57 52.8 +19 44 49	02 57 53.7 19 44 45.9	13.9	-
0221.1+1958	02 21 09.1 +19 58 22	02 21 09.0 19 58 15.3	6.7	-
1022.9+1944	10 22 55.6 +19 44 27	10 22 56.2 19 44 28.0	7.6	-
1018.9+2159	10 18 58.2 +21 59 40	– –	–	-
1535.0+2336	15 35 05.9 +23 36 53	15 35 06.1 23 36 53.7	1.7	-
1103.5+2459	11 03 34.6 +24 59 15	11 03 35.4 24 59 09.6	18.3	-
1256.1+2600	12 56 09.9 +26 00 37	– –	–	Y (wp201514n00)
1348.8+2638	13 48 52.4 +26 38 11	– –	–	-
1339.2+2717	13 39 14.3 +27 17 25	13 39 13.9 27 18 10.2	91.4	Y (wp701459n00)
1340.1+2743	13 40 11.9 +27 43 32	13 40 10.3 27 43 38.9	33.4	-
1203.5+2800	12 03 31.3 +28 00 39	12 03 31.3 28 00 51.1	21.6	Y (wp700232)
1221.5+2806	12 21 35.6 +28 06 10	12 21 35.8 28 06 17.8	12.1	Y (wp700223)
1243.6+3204	12 43 40.7 +32 04 48	12 43 41.1 32 04 56.2	12.5	-
1241.5+3250	12 41 33.5 +32 50 42	12 41 34.2 32 49 43.5	128.	-
1050.6+3310	10 50 39.9 +33 10 00	– –	–	-
1226.9+3332	12 26 56.9 +33 32 41	12 26 57.0 33 32 51.1	19.7	-
1220.6+3347	12 20 38.2 +33 47 23	12 20 38.4 33 47 26.7	5.6	-
1657.7+3519	16 57 47.4 +35 19 00	– –	–	-
1103.3+3558	11 03 20.3 +35 58 40	– –	–	Y (p200127)
1415.1+3608	14 15 11.9 +36 08 00	14 15 12.6 36 08 10.1	17.1	-
1216.9+3743	12 16 57.0 +37 43 47	12 16 57.1 37 43 35.4	26.7	-
1334.4+3808	13 34 28.4 +38 08 50	13 34 29.0 38 08 58.2	13.7	-
0951.4+3916	09 51 28.2 +39 16 38	09 51 28.7 39 16 36.8	7.9	-
1101.7+3923	11 01 47.6 +39 23 16	– –	–	-
1210.3+3930	12 10 22.4 +39 30 22	– –	–	-
1501.9+4009	15 01 58.2 +40 09 38	– –	–	Y (wp201536n00)
1631.7+4146	16 31 46.4 +41 46 01	16 31 47.7 41 46 26.7	64.8	Y (wp701552n00)
0909.7+4302	09 09 43.5 +43 02 48	– –	–	-
1412.3+4355	14 12 21.3 +43 55 05	14 12 21.3 43 55 05.2	0.6	-

depends on the SED peaks positions with respect to the X-ray band. Most of the X-ray selected BL Lacertae objects would have the synchrotron peak in X-ray band and show a slightly concave spectrum, with $\alpha_S \leq \alpha_H$ or a spectrum consistent with a power-law $\alpha_S = \alpha_H$. Radio-selected objects, on the other hand, would show in the X-ray band the "inter-peaks" region of their SEDs and have $\alpha_S \geq \alpha_H$ or $\alpha_S = \alpha_H$.

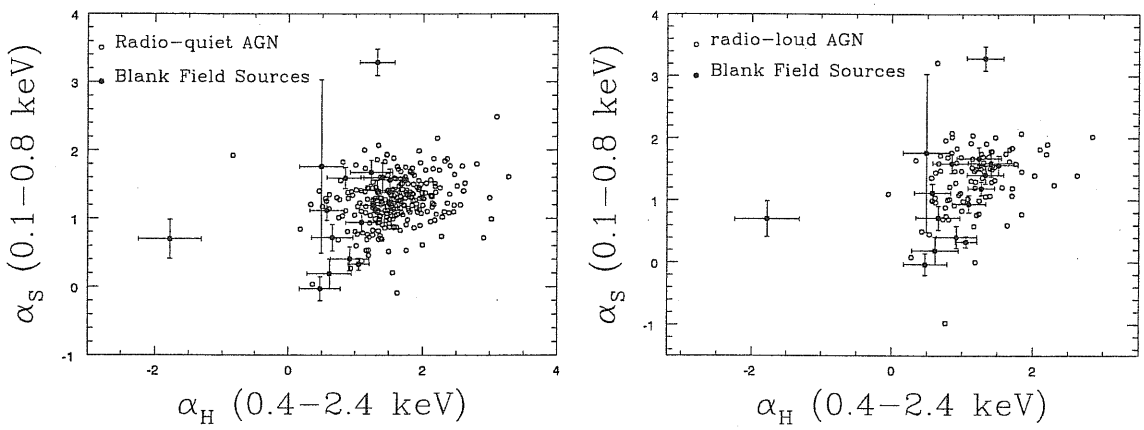

Figure 3.1: *ROSAT* PSPC effective spectral indices of blank field sources (filled black circles) derived as in Fiore et al. (1998), compared to a reference sample of (left) radio-quiet quasars and to (right) radio-loud quasars from Fiore et al. (1998) (red open circles)

3.1.1 X-ray Spectra

We extracted the spectra of the 16 blank field sources from the archival revision 2 *ROSAT* PSPC data at HEASARC using XSELECT 2.0. When the source was detected in more than one PSPC observations we extracted a combined spectrum. We used a local background, i.e. a region free of any evident object close to the source, to fit the PSPC spectra of each source within XSPEC 11.0.1 with three different models:
(1) an absorbed power law model of the form

$$F(\nu) = k \times \nu^{-\Gamma} \exp -[\Sigma_{\rm H} {\rm N(H)} \sigma_{\rm H}]$$

where $F(\nu)$ is in photons cm^{-2} s^{-1} keV^{-1}, Γ is the photon index, k is the normalization at 1 keV and the absorption is characterized by an hydrogen column density N(H) and an absorption cross section $\sigma_{\rm H}$ for each element. We fitted the data leaving all the parameters free in the fit and again fixing the absorbing column to the Galactic value from the Bell Labs HI survey (Stark et al. 1992, found with w3nh at HEASARC).

(2) a black body model of the form

$$F(\nu) = k \times 8.0525 E^2 dE/((KT)^4(\exp(E/KT) - 1))$$

where k is the normalization and KT is the temperature in keV.
As evident in Figure 3.3 there is a $\geq 3\sigma$ indication, for an absorbing column in excess of the Galactic value for three blank field sources (filled points in Figure 3.3).
(3) an absorbed and redshifted Raymond-Smith optically thin thermal plasma with absorption fixed to the Galactic value.
The results of these fits are reported in Tables 3.3 and the spectra of the blank field sources fitted with the absorbed power law model and their residuals are reported in Figure 3.2.

Combined spectra

In order to gain statistics and improve the goodness of the fit, we divided the sources into 2 groups according to the indications given by the results of the spectral fits with an absorbed power law model with free absorption (Figure 3.3):

(1) - the 'absorbed' sample: sources with an indication of heavy absorption in excess of the Galactic value ($\alpha_H \leq 0.62$ and $\alpha_S \leq 0.70$). This sample is composed of the three sources represented as red points in Figure 3.3 (1WGA J1243.6+3204; 1WGA J1216.9+3743 and 1WGA J0951.4+3916);

(2) - the 'unabsorbed' sample: sources with absorption consistent with the Galactic value ($\alpha_H > 0.62$ and $\alpha_S > 0.70$, blue points in Figure 3.3).
For these combined spectra we omitted the three sources with Galactic column density larger than 4.26×10^{20} cm^{-2} (black points in Figure 3.3).

We computed the average spectra of these two groups of sources (Figure 3.4). We divided the unabsorbed sources into two groups, i.e. the sources observed before and after the change in the PSPC gain occurred on October 1991, computed two separate combined spectra and then fitted the 2 spectra simultaneously. All the sources in the absorbed sample were observed after October 1991.

Fitting this composed spectra with the models described in § 3.1.1, we obtained the results summarized in Table 3.3. The spectra of each individual source did not have enough statistics to discriminate between the competing models. Combining the spectra we found that the best fit model for both samples is an absorbed power law model with photon index ~ 2, but the absorbing column is, as expected, different in the two cases. The 'absorbed' sample requires absorption of $\sim 2 \times 10^{21}$, well in excess of the Galactic value, while the 'unabsorbed' sample does not. The Raymond-Smith model

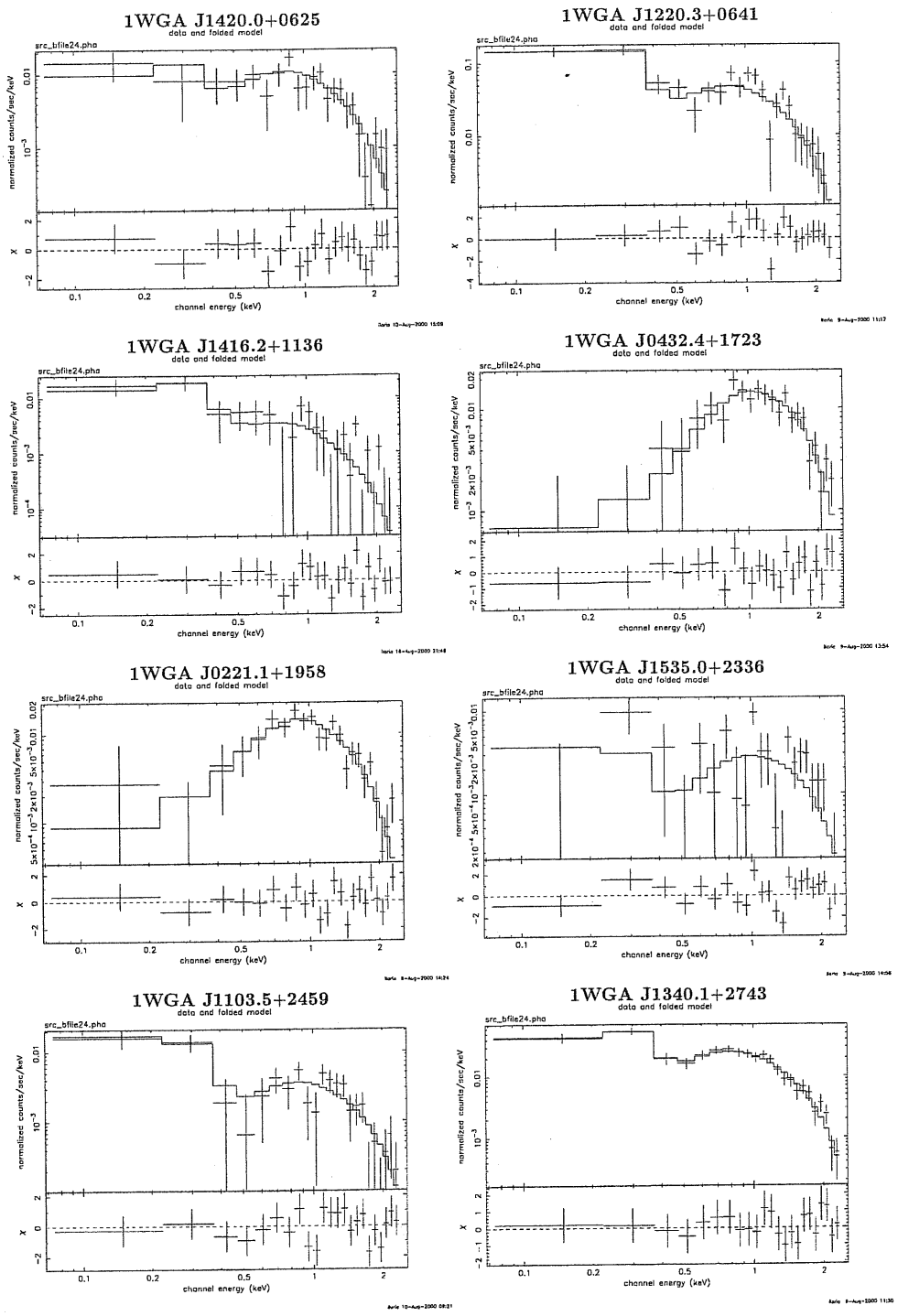

Figure 3.2: *ROSAT* PSPC energy spectra of the 16 blank field sources (upper panel); the solid lines represents the best fit with and absorbed power law model. The lower panels show the residuals.

1WGA J1243.6+3204

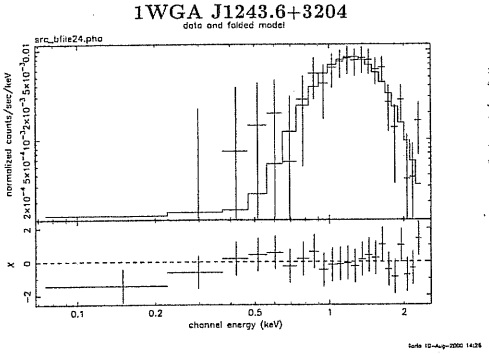

1WGA J1226.9+3332

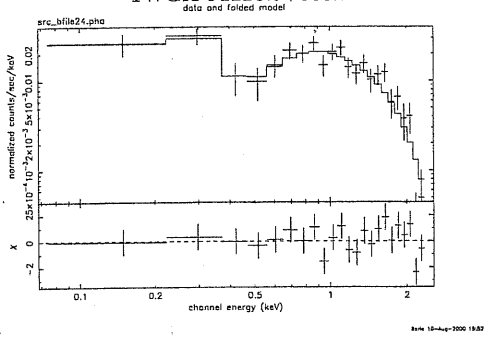

1WGA J1220.6+3347

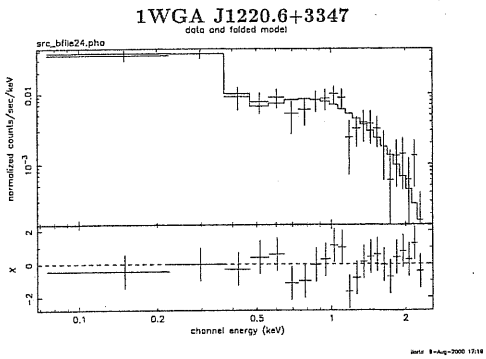

1WGA J1216.9+3743

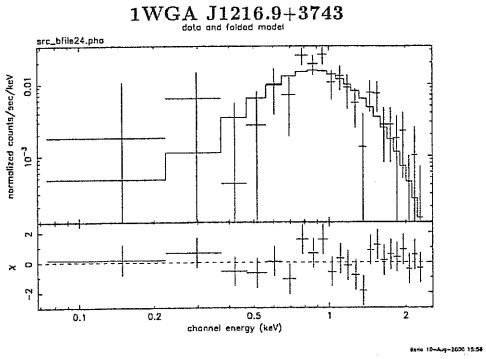

1WGA J0951.4+3916

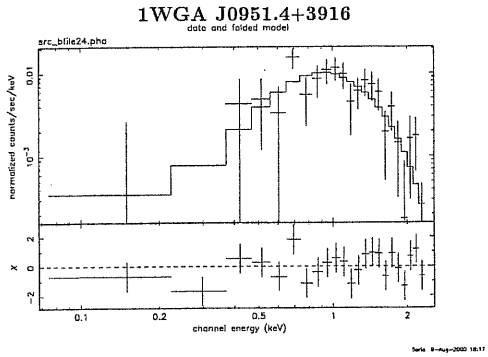

1WGA J1412.3+4355

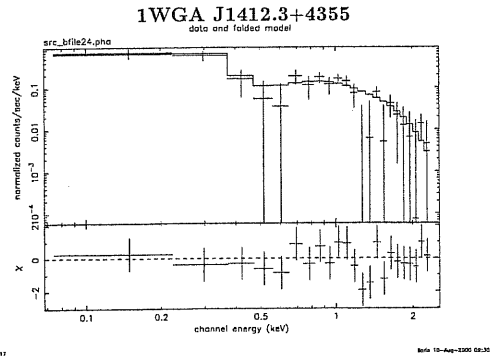

1WGA J1415.2+4403

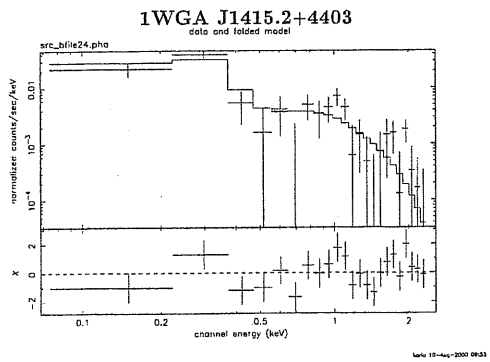

1WGA J1233.3+6910

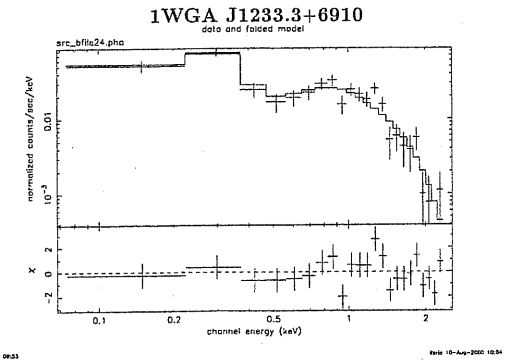

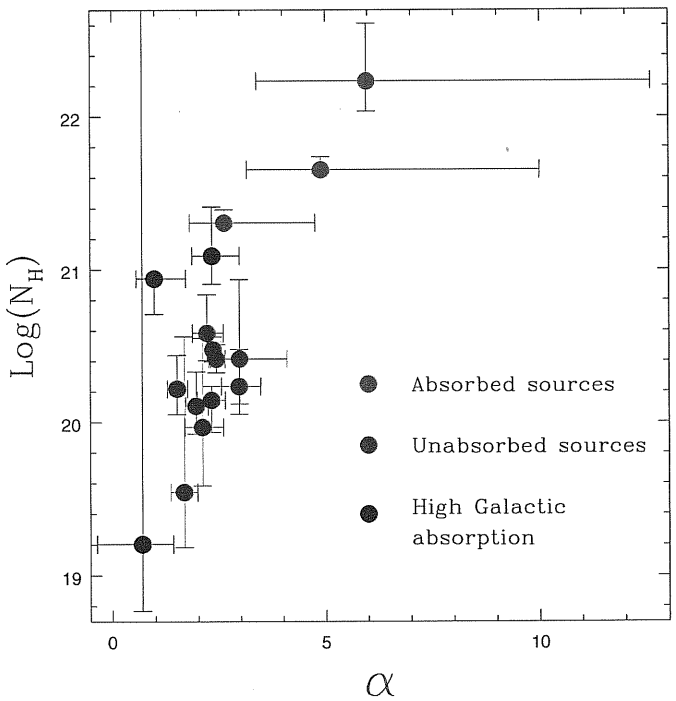

Figure 3.3: Energy spectral slope versus absorption column as derived from the fit with an absorbed power law model. Red circles represent sources with indication of heavy absorption in excess of the Galactic value; black circles sources with high Galactic column density and the blue ones the sources with absorption consistent with the Galactic value

is a poor description of the combined spectra for both samples, with the temperature reaching the maximum allowed value, while the black body model is acceptable for the 'absorbed' sample, but it completely fails to describe the 'unabsorbed' sources. The large χ^2 value obtained for the 'unabsorbed' sample suggests a more complex spectral shape.

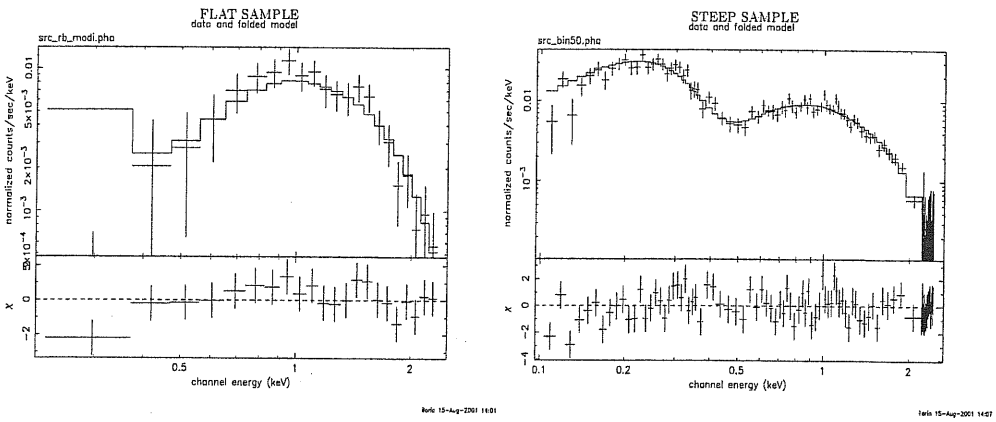

Figure 3.4: *ROSAT* PSPC combined energy spectra of the 'absorbed' (left) and 'unabsorbed' (right) samples and the residuals to the fit (bottom panels) (see text for details).

Table 3.3: Spectral fits with: an absorbed power law, a black body and an absorbed Raymond-Smith model

Source name	Absorbed power law					Black body			Raymond-Smith			
1WGA J	Γ^a	k^b	N_H^c	$N_{H(gal)}^d$	χ_r^{2e}	KT^f	k^b	χ_r^{2e}	KT^f	z	k^b	χ_r^{2e}
1420.0+0625	$2.21^{+0.38}_{-0.34}$	$0.52^{+0.06}_{-0.08}$	$3.84^{+2.23}_{-1.58}$	2.18	0.82	258^{+34}_{-26}	$1.41^{+0.16}_{-0.13}$	0.84	$3.051^{+1.60}_{-0.92}$	$1.20^{+0.80}_{-0.47}$	$6.2986^{+5.78}_{-12.60}$	0.79
	$1.79^{+0.17}_{-0.19}$	$4.66^{+0.46}_{-0.51}$	fixed	–	0.82							
1220.3+0641	$1.95^{+0.28}_{-0.25}$	$2.22^{+0.27}_{-0.17}$	$1.28^{+0.66}_{-0.54}$	1.56	1.34	174	8.12	2.55	$2.66^{+61.34}_{-2.07}$	$2.00^{h}_{-0.27}$	$68.2^{+5.0}_{-14.0}$	1.84
	2.07 ± 0.10	$23.39^{+1.67}_{-2.66}$	fixed	–	1.29							
1416.2+1136	$2.98^{+1.11}_{-0.69}$	$0.14^{+0.06}_{-0.03}$	$2.61^{+3.11}_{-1.78}$	1.81	0.90	145 ± 14	$0.80^{+0.13}_{-0.14}$	0.90	$1.12^{+0.29}_{-0.08}$	$2.00^{h}_{-0.43}$	$7.79^{+1.46}_{-15.59}$	0.96
	$2.68^{+0.27}_{-0.24}$	$1.54^{+0.31}_{-0.54}$	fixed	–	0.86							
0432.4+1723	$1.03^{+0.68}_{-0.46}$	$0.92^{+0.44}_{-0.17}$	$9.42^{+12.40}_{-5.34}$	13.1	0.77	559^{+11}_{-8}	$4.34^{+1.44}_{-0.84}$	0.88	$62.64^{h}_{-50.07}$	0.26^{h}_{h}	$8.55^{+16.83}_{-17.11}$	0.77
	$1.20^{+0.23}_{-0.26}$	$10.56^{+6.29}_{-1.33}$	fixed	–	0.95							
0221.1+1958	$2.33^{+0.65}_{-0.47}$	$0.96^{+0.34}_{-0.16}$	$12.29^{+9.03}_{-5.23}$	9.59	0.96	1120	2.99	1.66	$2.52^{+1.05}_{-0.61}$	$0.55^{+0.49}_{-0.18}$	$5.42^{+5.54}_{-10.83}$	0.94
	2.15 ± 0.28	$9.21^{+0.37}_{-1.00}$	fixed	–	0.93							
1535.0+2336	$0.70^{+0.72}_{-1.05}$	$0.14^{+0.04}_{-0.04}$	$0.16^{+2.37}_{-0.16}$	4.26	1.67	343^{+43}_{-35}	$2.25^{+0.14}_{-0.31}$	1.2	$64^{h}_{-61.32}$	0.34^{h}_{h}	$1.52^{+3.4}_{-3.05}$	1.75
	$0.47^{+1.72}_{-1.68}$	1.40 ± 0.66	fixed	–	1.66							
1103.5+2459	1.67 ± 0.31	$0.16^{\pm}0.02$	$0.35^{+0.82}_{-0.29}$	1.38	0.92	214^{+74}_{-42}	$0.55^{+0.09}_{-0.07}$	1.62	$3.46^{+1.50}_{-0.99}$	$2.00^{h}_{-0.58}$	$4.65^{+0.70}_{-9.29}$	1.22
	$2.10^{+0.17}_{-0.18}$	$1.76^{+0.20}_{-0.25}$	fixed	–	0.94							
1340.1+2743	2.35 ± 0.18	$1.18^{+0.09}_{-0.04}$	$2.99^{+0.58}_{-0.54}$	1.09	0.53	208	3.54	2.06	$2.83^{+0.80}_{-0.34}$	$1.24^{+0.25}_{-0.30}$	$15.5^{+3.2}_{-4.1}$	0.61
	1.72 ± 0.06	$10.83^{+0.42}_{-0.55}$	fixed	–	1.25							
1243.6+3204	$5.97^{+6.62}_{-2.59}$	$18.3^{+366.7}_{-36.7}$	$171.3^{+149.5}_{-78.3}$	1.23	0.49	770^{+40}_{-58}	$3.51^{+7.01}_{-5.22}$	0.77	$63.76^{h}_{-34.85}$	$0^{+1.24}_{h}$	$2.01^{+0.27}_{-4.02}$	1.78
	$0.07^{+0.22}_{-0.53}$	$3.14^{+0.35}_{-0.61}$	fixed	–	0.84							
1226.9+3332	$1.51^{+0.24}_{-0.23}$	$1.06^{+0.12}_{-0.05}$	$1.66^{+0.84}_{-0.64}$	1.38	1.08	299^{+31}_{-24}	$3.35^{+0.27}_{-0.25}$	1.84	$8.07^{+10.01}_{-2.85}$	$0.81^{h}_{-0.58}$	$9.75^{+13.19}_{-19.51}$	1.07
	1.42 ± 0.11	$11.05^{+0.40}_{-0.98}$	fixed	–	1.04							
1220.6+3347	2.31 ± 0.33	$0.37^{+0.03}_{-0.06}$	$1.40^{+0.29}_{-0.68}$	1.27	0.63	147^{+8}_{-7}	1.52 ± 0.12	1.55	$1.86^{+0.32}_{-0.35}$	$2.00^{h}_{-0.25}$	$12.7^{+1.3}_{-1.8}$	1.17
	2.26 ± 0.11	$3.70^{+0.29}_{-0.59}$	fixed	–	0.60							

Table 3.3: Spectral fits with: an absorbed power law, a black body and an absorbed Raymond-Smith model

1216.9+3743	$4.90^{+5.10}_{-1.74}$	$2.17^{+4.35}_{-19.43}$	$44.78^{+8.72}_{-2.43}$	1.69	0.81	274^{+43}_{-32}	$1.86^{+0.15}_{-0.33}$	0.87	$1.10^{+0.29}_{-0.20}$	$0.14^{+0.12}_{-0.10}$	$1.12^{+0.68}_{-2.25}$	0.67
	$1.34^{+0.25}_{-0.31}$	$5.76^{+0.40}_{-1.27}$	fixed	–	1.16							
0951.4+3916	$2.62^{+2.14}_{-0.81}$	$0.82^{+1.72}_{-1.64}$	$20.19^{+3.99}_{-1.09}$	1.55	0.93	362^{+55}_{-76}	$1.64^{+0.20}_{-0.36}$	1.05	$1.41^{+1.33}_{-0.27}$	$0.00^{+0.09}_{h}$	$0.83^{+0.45}_{-0.23}$	1.35
	$0.92^{+0.25}_{-0.28}$	$4.21^{+0.39}_{-0.67}$	fixed	–	1.29							
1412.3+4355	$2.10^{+0.49}_{-0.42}$	$0.63^{+0.07}_{-0.10}$	$0.93^{+1.25}_{-0.82}$	1.16	0.74	162^{+19}_{-12}	$26.37^{+3.98}_{-3.07}$	1.09	$2.16^{+0.72}_{-0.42}$	$2.00^{+}h_{-0.40}$	209^{+28}_{-62}	0.85
	2.20 ± 0.15	$63.15^{+7.59}_{-7.84}$	fixed	–	0.71							
1415.2+4403	$2.97^{+0.50}_{-0.43}$	$0.146^{+0.03}_{-0.04}$	$1.72^{+0.96}_{-0.72}$	1.17	1.13	124^{+11}_{-10}	$0.98^{+0.79}_{-0.17}$	1.50	$1.03^{+0.06}_{-0.08}$	$2.00^{h}_{-0.14}$	$6.86^{+1.04}_{-1.33}$	1.36
	$2.70^{+0.22}_{-0.20}$	$1.52^{+0.25}_{-0.48}$	fixed	–	1.12							
1233.3+6910	$2.43^{+0.20}_{-0.18}$	$1.17^{+0.07}_{-0.09}$	$2.60^{+0.57}_{-0.53}$	1.69	1.39	185	4.14	2.38	$2.27^{+0.21}_{-0.24}$	$1.79^{h}_{-0.06}$	$29.7^{+6.4}_{-2.0}$	1.63
	2.12 ± 0.08	$11.39^{+0.50}_{-1.03}$	fixed	–	1.45							
absorbed sample	$2.09^{+0.89}_{-0.37}$	$0.79^{+0.52}_{-0.23}$	$18.47^{+16.32}_{-10.00}$	1.49	0.49	404^{+35}_{-30}	$1.79^{+0.17}_{-0.16}$	0.62	64	0.00	2.69	2.07
	$0.74^{+0.14}_{-0.15}$	$4.54^{+0.13}_{-0.49}$	(1.49)fixed	–	1.12							
unabsorbed sample	$2.10^{+0.05}_{-0.02}$	$-^{f}$	$1.68^{+0.06}_{-0.12}$	1.45	1.38	176	1.16	11.90	2.58	1.79	$-^{f}$	3.92
	2.01 ± 0.03	$-^{g}$	1.45(fixed)	–	1.42							

[a] Photon index

[b] normalizations at 1 keV in 10^{-4} for the power law and the Raymond-Smith models and in 10^{-6} ph cm^{-2} s^{-1} keV^{-1} for the blackbody model

[c] Hydrogen column density for an absorbed power law in 10^{20} atoms cm^{-2}

[d] Galactic hydrogen column density (Stark et al. 1992)

[e] Reduced χ^2

[f] Temperature in KeV

[g] We are simultaneously fitting two datasets (i.e. the sources observed before and after the change in PSPC gain) and we have two different normalizations

[h] value pegged to the hard limit

3.1.2 X-ray fluxes

We computed the X-ray fluxes in the 0.5-2.0 keV (the classical *ROSAT* band), 0.05-2.5 keV (same as WGACAT95) and 0.3-3.5 keV (*Einstein* band) using the best fit absorbed power law model for each source; the results are reported in Table 4.1.

For 4 sources (1WGA J1416.2+1136, 1WGA J1535.0+2336, 1WGA J1103.5+2459 and 1WGA J1415.2+4403) the 0.3-3.5 keV flux we estimated is $\sim$ 40% lower than WGACAT95 flux, making their f_X/f_V not so extreme anymore and compatible with normal type 1 AGNs (red solid line in Figure 3.5).

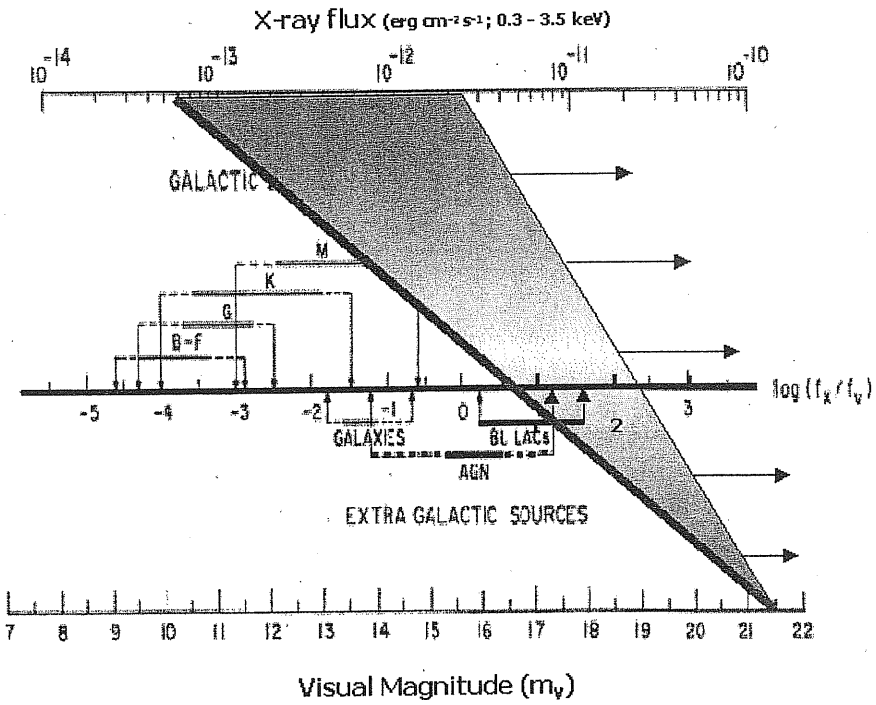

Figure 3.5: Maccacaro et al. 1988 normograph: the colored area shows the f_X/f_V for our blank field sources when using the 0.3-3.5 keV X-ray fluxes. The red solid lines shows the minimum values for the 16 blank field sources in our sample (see text).

But 6 sources (1WGA 1226.9+3332, 1WGA 1220.3+0641, 1WGA 0432.4+1723, 1WGA 1412.3+4355 and 1WGA 1233.3+6910) have $F_X(0.3 - 3.5keV) > 4 \times 10^{-13}$ erg cm^{-2} s^{-1} and their f_X/f_V is not even compatible with BL Lacertae objects.

3.1.3 Variability

We extracted the lightcurves for sources and backgrounds within each PSPC and HRI observation and subtracted them. We binned the lightcurves with

Table 3.4: X-ray (absorbed) fluxes for the 16 blank field sources.

Source name (1WGA J)	F_X^a (0.3-3.5 keV)	F_X^a (0.5-2.0 keV)	F_X^a (0.05-2.5 keV)	$F_{\rm WGA}^b$ (0.05-2.5 keV)
1420.0+0625	1.68	1.05	1.53	2.80
1220.3+0641	8.22	4.74	7.90	14.39
1416.2+1136	0.59	0.30	0.69	1.11
0432.4+1723	4.12	1.80	2.63	1.69
0221.1+1958	2.28	1.47	1.91	1.98
1535.0+2336	0.83	0.36	0.55	1.04
1103.5+2459	0.66	0.38	0.64	1.01
1340.1+2743	8.94	5.60	8.70	10.14
1243.6+3204	1.04	0.83	0.96	1.28
1226.9+3332	4.44	2.43	3.61	3.61
1220.6+3347	1.30	0.79	1.40	2.00
1216.9+3743	1.45	1.22	1.40	2.80
0951.4+3916	1.39	0.99	1.19	2.59
1412.3+4355	24.14	13.69	25.55	1.63
1415.2+4403	0.64	0.32	0.81	1.21
1233.3+6910	4.11	2.41	4.15	2.99

[a] in units of 10^{-13} erg cm^{-2} s^{-1} and computed assuming the best fit absorbed power law model with free absorption.
[b] in units of 10^{-13} erg cm^{-2} s^{-1} and computed using a constant correction factor of 1.5×10^{-11} erg cm^{-2} s^{-1}.

bin sizes ranging from 1000 to 5000 s and calculated the maximum variation factor of the source count rate considering the lightcurve points with errorbars smaller than 40%. No strong variability is seen even comparing multiple PSPC and/or HRI observation, for the 10 sources with multiple observations. The average maximum variability factor is 1.60 ± 0.71, consistent with the sources being constant. The variability factor was computed using all the available lightcurves spanning a minimum time scale of 1ks to a maximum time scale of $\sim$ 2 years. HRI count rates are consistent with PSPC ones, within the large errors due to spectral uncertainties. An extremely variable nature, transient or burst-like, (option 5 in § 2.1) is excluded for all the 16 blanks.

3.2 Extent: ROSAT HRI

This section is to be completed with the HRI positions and with a measure of the extent for the cluster

7 sources have one or more *ROSAT* HRI observations (see Table 3.2). Only one source (1WGA J1216.9+3743) is not visible in the HRI images; all the remaining 6 sources are detected. All of them look pointlike, except for 1WGA J1226.9+3332 (§ 6.2) which is clearly extended and suggests a cluster of galaxies nature and for 1WGA J1233.3+6910 which falls on the detector's edge making any estimate of count rate and extension impossible.

3.3 Radio Information

To check for a possible radio loudness of blank field sources we searched for radio counterparts in the NRAO VLA Sky Survey (NVSS, Condon et al. 1999) and in the FIRST survey (Becker, White & Helfand 1995) within the $39''$ X-ray error circle. Both surveys were conducted at 1.4 GHz. The NVSS is a radio survey covering the sky north of $\delta = -40$ with a limiting flux of $\sim$ 2.5 mJy and a position uncertainty of few arcseconds. FIRST (Faint Images of the Radio Sky at Twenty-cm) is an ongoing survey designed to cover over 10,000 deg^2 of the North Galactic Cap down to $\sim$ 1 mJy with a position accuracy $< 1''$. We found 4 NVSS and 2 FIRST[1] radio counterparts for the blank field sources. We report in Table 3.5 the radio data.

We computed the α_{ro} and α_{ox} for the sources in Table 3.5 using the NVSS radio flux, the X-ray flux at 1 keV (see Table 3.3) and a O magnitude limit of 21.5 (considered to be equal to the V magnitude). We used NVSS fluxes instead of FIRST fluxes because the latter ones can be underestimated

[1]The remaining 2 NVSS sources are in an area not yet covered by FIRST

Table 3.5: The radio counterparts to the blank field sources.

Source (1WGA J)	NVSS coord. Ra, Dec (J2000)	FIRST coord. Ra, Dec (J2000)	NVSS flux[a] (mJy)	FIRST flux[a] (mJy)
1WGA J0432.4+1723	04 32 30.53 17 23 41.0	not covered yet	3.2 ± 0.6	–
1WGA J0221.1+1958	02 21 09.25 19 58 07.2	not covered yet	7.9 ± 0.5	–
1WGA J1340.1+2743	13 40 10.93 27 43 45.7	13 40 10.853 27 43 46.96	4.6 ± 0.5	3.75
1WGA J1226.9+3332	12 26 58.32 33 32 44.3	12 26 58.186 33 32 48.63	4.9 ± 0.6	3.61

[a] @ 1.4 GHz

because of the high spatial resolution of the survey. Even in the NVSS, some of the flux coming from extended sources could be either resolved out or split into two or more components, leading to a systematic underestimate of the real flux densities of such sources (Condon et al. 1998).

For 1WGA J1226.9+3332, identified as a z=0.89 cluster of galaxies (see § 6.2) we measured a R band magnitude of 20.4 and we converted it into V magnitude of 22.2 using and (V-R)=1.83, typical for an elliptical galaxy at z=0.89 (Coleman, Wu & Weedman 1980), obtaining $\alpha_{ro} = 0.60$ and $\alpha_{ox} = 0.68$ (red square in Figure 3.6). For 1WGA J1340.1+2743, a BL Lacertae object (see § 6.1) we used $R \sim 22$ (from Lamer, Brunner & Staubert 1997) and converted it using the mean $V - R \sim 0.65$ found for BL Lacertae objects (Moles et al. 1985) and we obtained $\alpha_{ro} = 0.63$ and $\alpha_{ox} = 0.61$ (red dot in Figure 3.6). We note that both 1WGA J1226.9+3332 and 1WGA J1340.1+2743 are radio-loud sources with $f_{(1.4\mathrm{GHz})}/f_V \sim 1000$.
For the remaining two blanks with a radio counterpart we obtained values of $\alpha_{ro} \geq 0.5$ and $\alpha_{ox} \leq 0.7$ (red arrows in Figure 3.6). For the remaining sources, having upper limits both on their radio flux and optical magnitude, we have no information on the α_{ro}, but we can compute upper limits for their α_{ox} (colored area in Figure 3.6).
Since BL Lacertae objects are the known class of X-ray emitting sources with higher f_X/f_V, we compared the region of the α_{ro}-α_{ox} occupied by the blank field sources with those of X-ray selected BL Lacs (e.g. Laurent-Muelheisen et al. 1999) Figure 3.6 shows that the blank field sources with a radio counterpart (red symbols) tend to fill an extreme region of the α_{ro}-α_{ox} plane, where just few BL Lac objects fall.

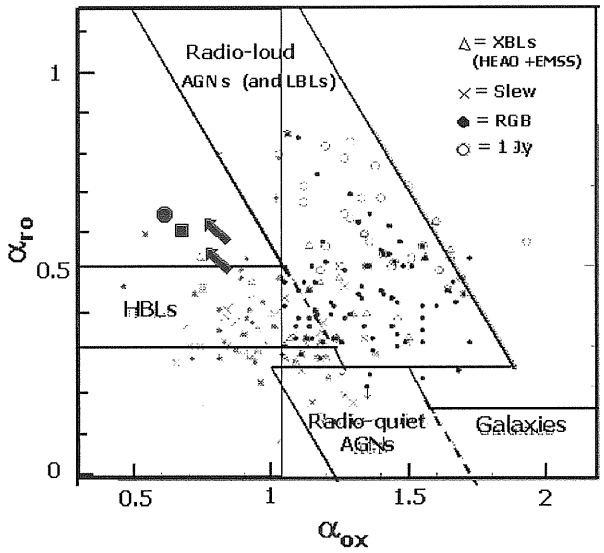

Figure 3.6: Broad band spectral indices for the 4 blank field sourceswith a radio counterpart. The red square represents the high z cluster 1WGA J1226.9+3332 and the red dot the BL Lacertae object 1WGA J1340.1+2743. For the remaining 2 sources with a radio counterpart we computed upper and lower limits for α_{ox} and α_{ro} and represented them on the plot with arrows. The yellow area represents the spread of the upper limits of the α_{ox} computed for the remaining 14 blank field sources

Chapter 4

Optical and IR campaigns

In this and in the following chapters we present the results of the study of the new data we obtained. In particular, this chapter describes the optical and IR follow-up observations we performed to understand the nature of *ROSAT* blank field sources.
The *ROSAT* archival data cannot give us any other information on the nature of blank field sources; to make progress we need to identify these sources with optical or near infrared counterparts. Two of the main hypotheses regarding the nature of blank field sources suggest red colors for them: in particular, if blank field sources are red AGNs (option 3a and 3b in § 2.1) we expect $R - K = 5 - 6$, which corresponds to $A_V \sim 3$ (e.g. Webster et al. 1995, Kim & Elvis 1998, and 1999); if they are (option 4a) high redshift clusters of galaxies we expect $R - K$ ranging from 4 ($z \sim 0$) to 9 (for $z \sim 3$). We obtained optical (R band) and infrared (K band) imaging for the 16 fields in our sample.

4.1 Optical run

THE OPTICAL AND IR RUN ARE THE MOST AFFECTED BY THE STOLEN BOOKS. ALL THE NUMBERS OF MAGNITUDES, POSITIONS AND SO ON WERE WRITTEN THERE

We observed the blank field sources at SAO 48-inch telescope in February 1997 **All the info I had on the data reduction were in the stolen notebooks** in the R band down to $R \sim 22$. The imaged fields are shown in Figure 4.2 (left) and the R band magnitudes of the brightest sources inside the ROSAT error circle are shown in Table 4.1. As evident from the images, there are some candidates in most fields. However about 3 objects are expected by chance at $R \sim 22$ (Huang et al. 2001).

write details of data reduction here

We computed the $log(f_X/f_R)$ for the 16 blank field sources according to the formula:

$$log\left(\frac{f_X}{f_R}\right) = logf_X + \frac{R}{2.5} + 5.50$$

and the majority of the sources fall in the $log((f_X/f_R) = 0.0 \pm 1.0$ range, typical of AGNs in the local universe (e.g. Schmidt et al. 1998; Akiyama et al. 2000; Hornschemeier et al. 2001; Lehmann et al. 2001). Few sources, however have extreme values of (f_X/f_R): 1WGA J1233.3+6910, 1WGA J1226.9+3332, 1WGA J1412.3+4355 and 1WGA J1340.1+2743, not compatible with local type 1 or type 2 AGNs.

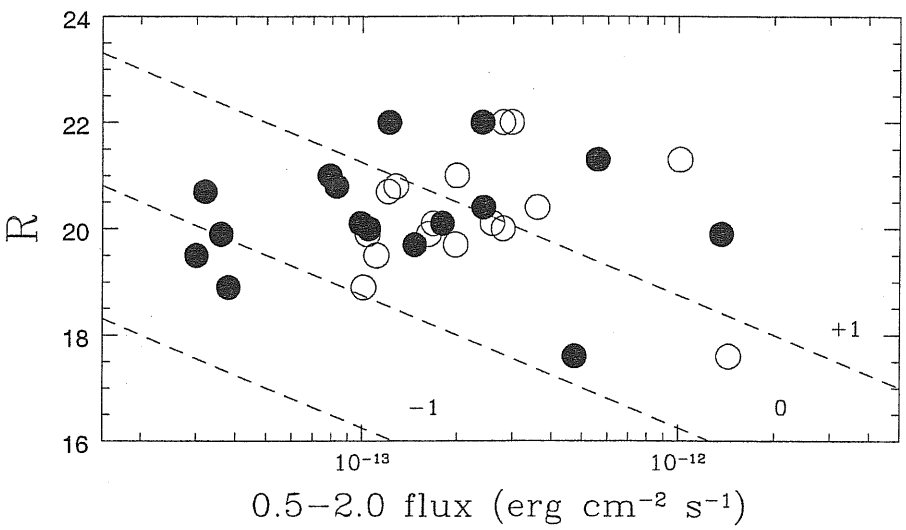

Figure 4.1: R magnitude vs. 0.5-2.0 keV flux for the 16 blank field sources. The filled red symbols represent our estimated flux derived using the best fit absorbed power law model to the spectra; the open blue symbols represent the WGACAT95 fluxes. The 3 dashed lines correspond to $log(f_X/f_R) = +1, 0, -1$ (from top to bottom)

4.2 Infrared run

We observed the blank field sources fields at the IRTF 3.5 m telescope in January 2000. We obtained K band imaging down to $K \sim 19 - 20$.

write details of data reduction here

The images of these fields are shown in Figure 4.2 (right) and the magnitudes of the brightest objects are listed in Table 4.1.

We note that about $\sim 3-7$ objects are expected by chance at $K = 19-20$ in the *ROSAT* 39″ error circle (Huang et al. 2001).

Table 4.1: Available optical and IR magnitudes for the 16 blank field sources.

Source name (1WGA J)	R (mag)	E[a] (mag)	B (mag)	O[a] (mag)	K (mag)	O-E[b] (mag)	R-K (mag)	F_X^c (0.5-2.0 keV)	$F_{\rm WGA}^d$ (0.05-2.5 keV)
1420.0+0625	20.0	-	-	-	?	-	?	1.05	2.80
1220.3+0641	17.6	18.58	-	21.81	13.6	3.23	4.0	4.74	14.39
1416.2+1136	19.5	19.5	20.7**	22.22	?	2.72	?	0.30	1.11
0432.4+1723	20.1	20.0	-	-	?	> 1.5	?	1.80	1.69
0221.1+1958	19.7	-	-	-	15.1	-	?	1.47	1.98
1535.0+2336	19.9	19.6	-	21.8	?	2.2	?	0.36	1.04
1103.5+2459	18.9	18.2	-	-	16.2	> 3.3	2.7	0.38	1.01
1340.1+2743	21.3	-	-	-	?	-	?	5.60	10.14
1243.6+3204	20.8	-	-	-	?	-	?	0.83	1.28
1226.9+3332	20.4	-	-	-	15.4	-	5.0	2.43	3.61
1220.6+3347	?	?	-	21.7	?	?	?	0.79	2.00
1216.9+3743	~ 22	-	-	-	?	?	?	1.22	2.80
0951.4+3916	20.1	19.1	-	-	16.0	-	4.1	0.99	2.59
1412.3+4355	19.9	18.73	20.7	-	?	> 2.77	?	13.69	1.63
1415.2+4403	20.7	-	-	-	?	-	?	0.32	1.21
1233.3+6910	~ 22	-	-	-	?	-	?	2.41	2.99

[a] Palomar data

? K magnitude was written in the stolen notebooks

[b] when only the O or E magnitude is available we computed lower/upper limits on O-E assuming O=21.5 and E=19.5 as Palomar limits

[c] in units of 10^{-13} erg cm^{-2} s^{-1} assuming the best fit absorbed power law model with free absorption.

[d] computed using a constant correction factor of 1.5×10^{-11} erg cm^{-2} s^{-1}.

As evident from the comparison of the R and K band images some sources (e.g. Figure 4.2) appear bright in the K-band images and faint in the R-band. Indeed these sources have large values of R-K. Write numbers here **all the numbers are in the stolen notebooks**

4.3 Number-counts excess

As evident from the images of the blank field sources, some fields (e.g. 1WGA J0432.4+1723, 1WGA J1226.9+3332 and 1WGA J0221.1+1958) show an excess of IR sources. We computed the number counts in the K-band in the FOV of such sources and compared it to field counts from Gardner et al. 1993, Saracco et al. 1997, Huang et al. 1997, Minezaki et al. 1998, Huang et al. 2001. We found evidence of large excess which cannot be explained with magnitudes errors or with Poisson fluctuation. We report in Figure 4.3 the most striking examples of K-band counts excess.

Such an excess can be easily explained with physical clustering of the objects and with a cluster of galaxies nature for 1WGA J1226.9+3332, 1WGA J0432.4+1723 and 1WGA J0221.1+1958.

R K

1WGA J1420.0+0625

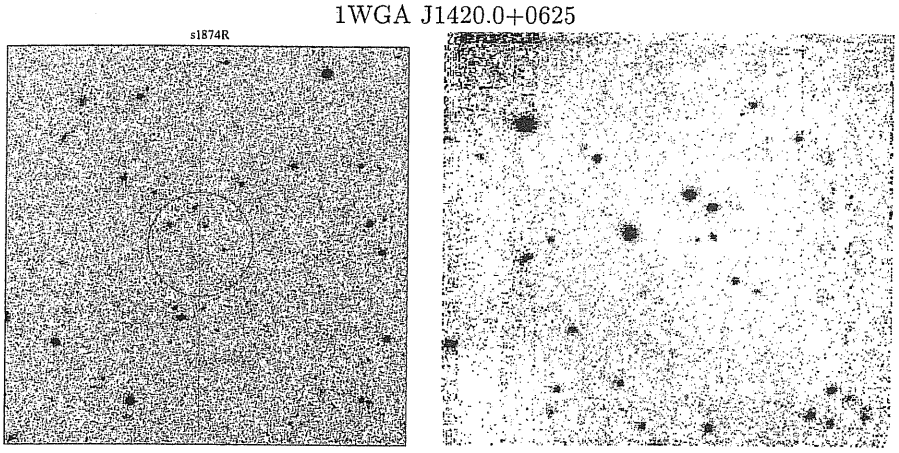

1WGA J1220.3+0641

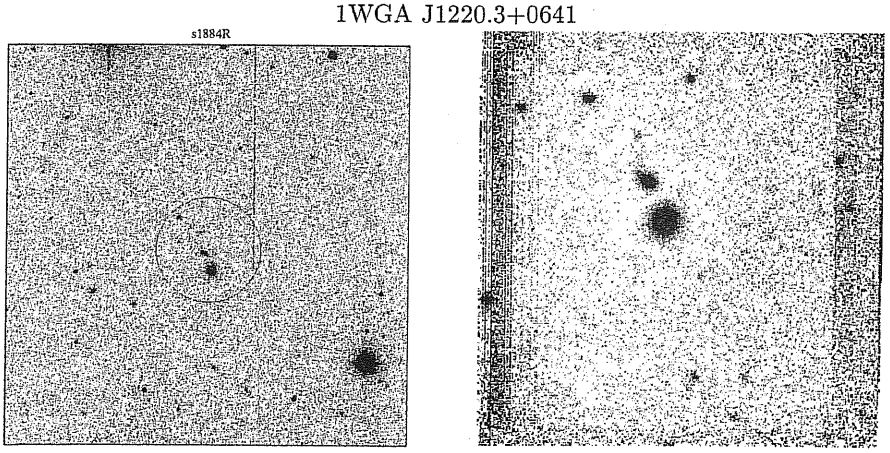

1WGA J1416.2+1136

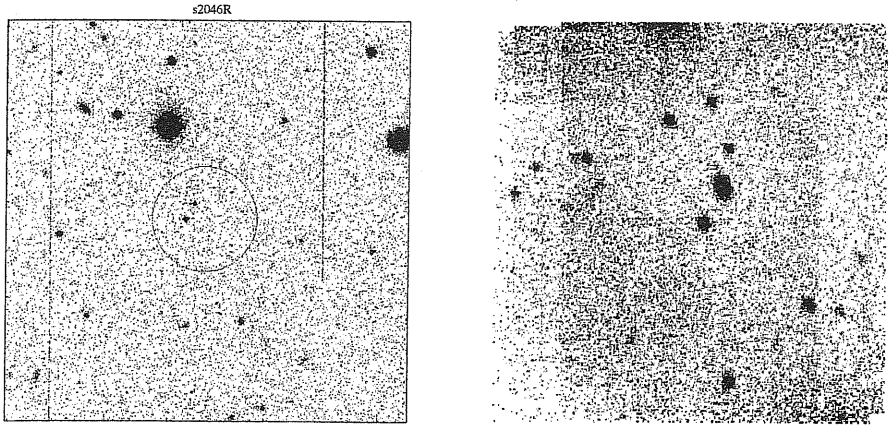

1WGA J0432.4+1723

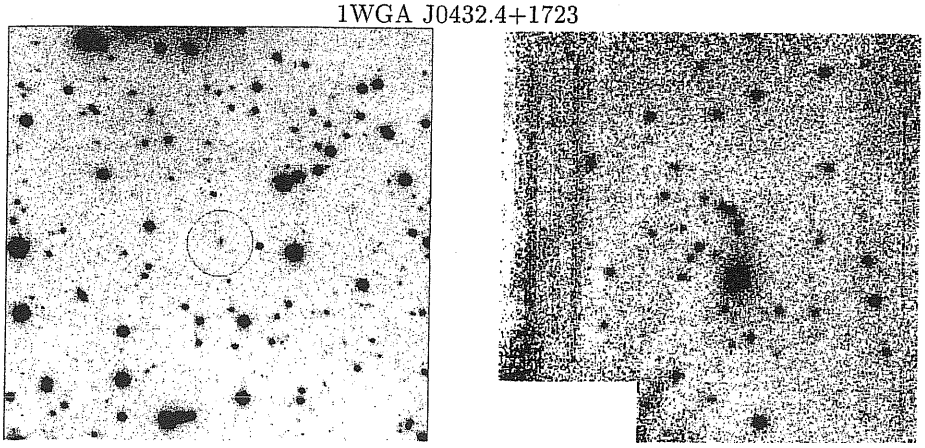

R K

1WGA J0221.1+1958

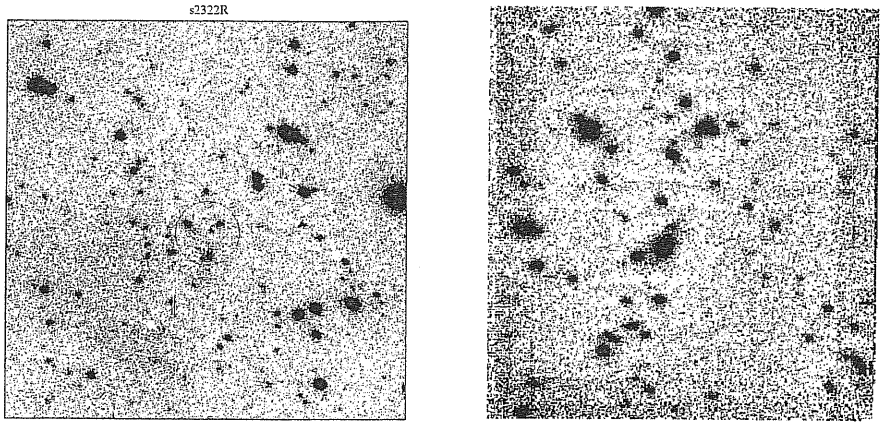

1WGA J1535.0+2336

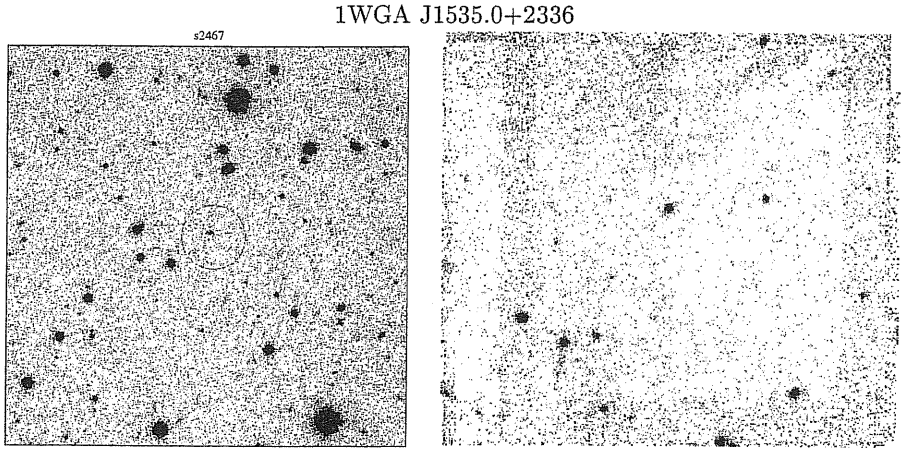

1WGA J1103.5+2459

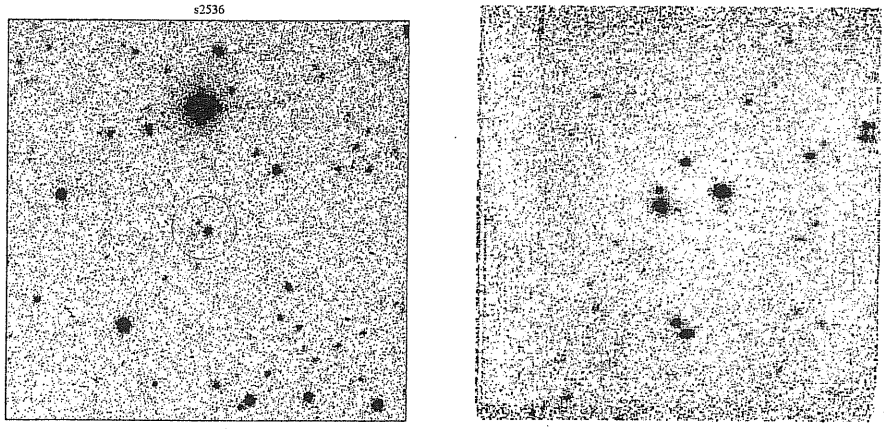

1WGA J1340.1+2743

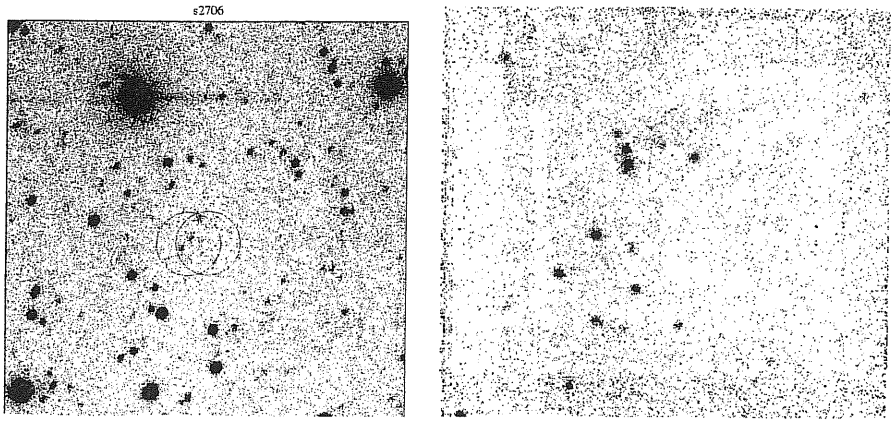

R K

1WGA J1243.6+3204

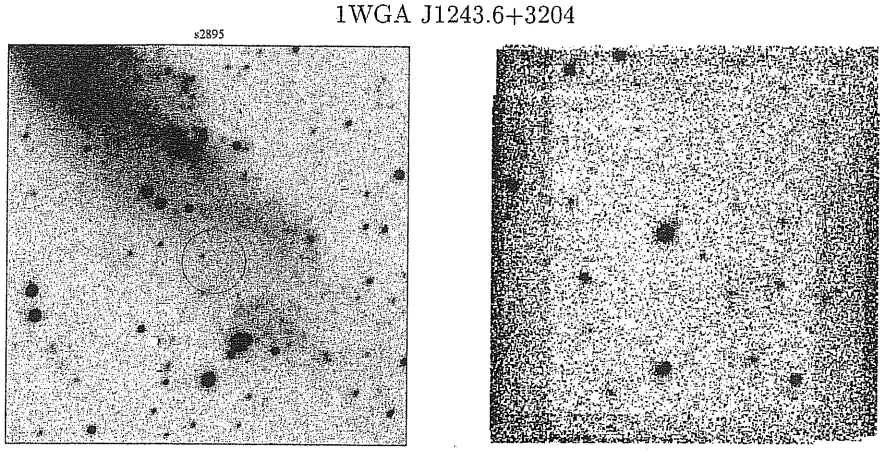

1WGA J1226.9+3332

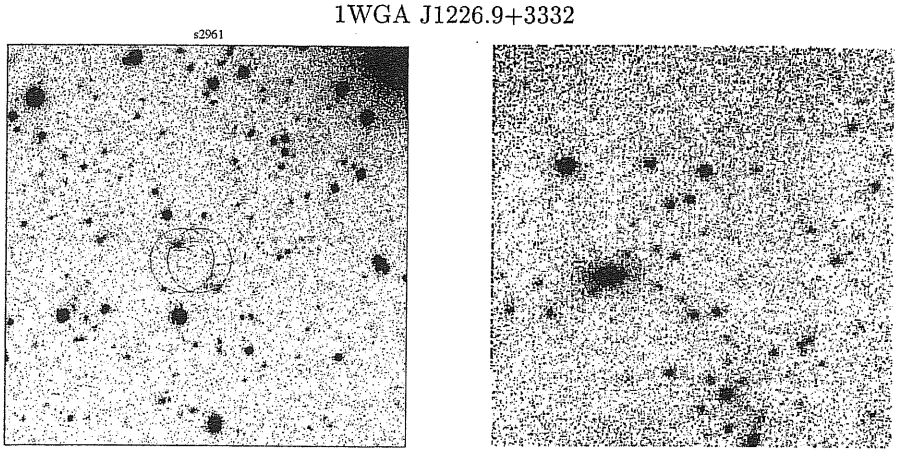

1WGA J1220.6+3347

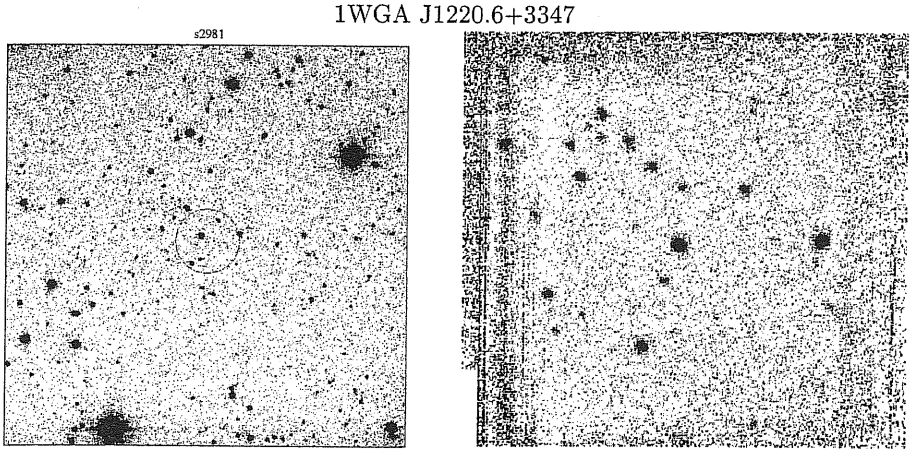

1WGA J1216.9+3743

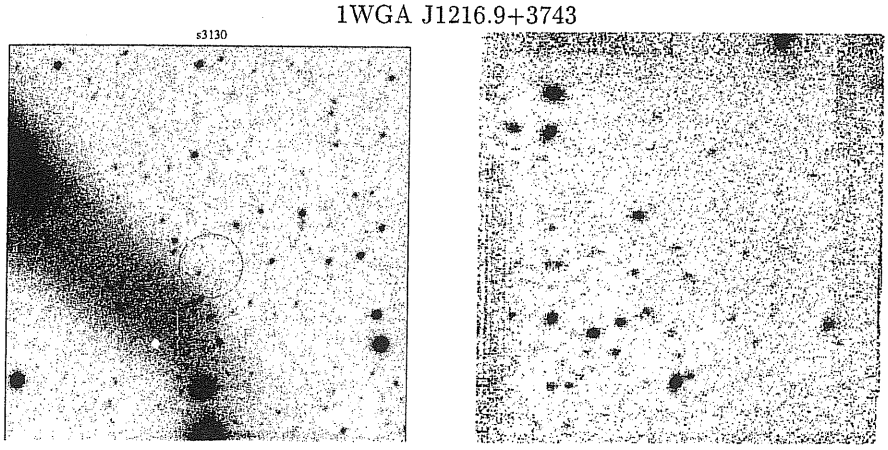

R K

1WGA J0951.4+3916

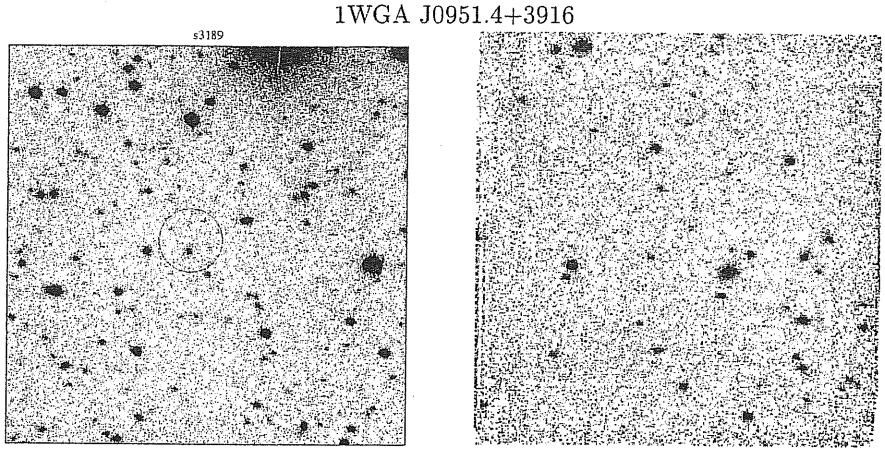

1WGA J1412.3+4355

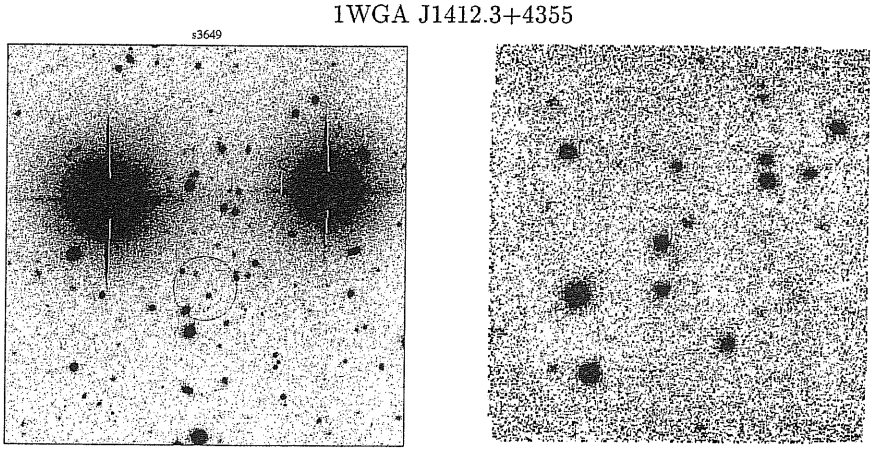

1WGA J1415.2+4403

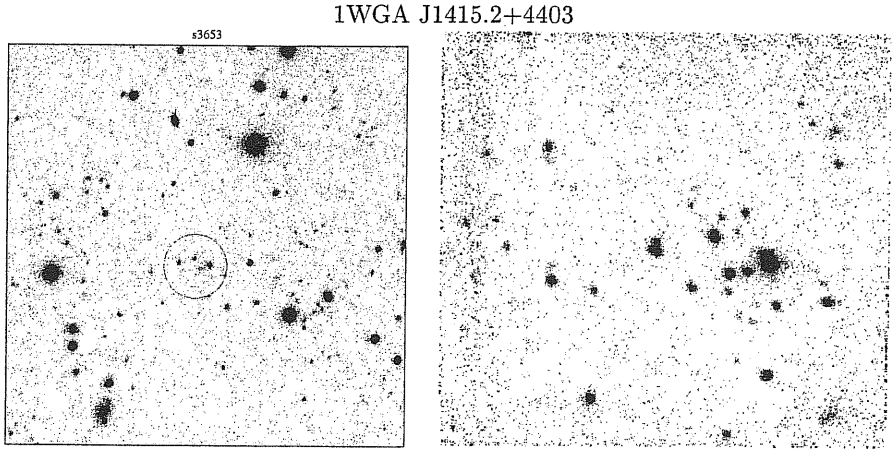

1WGA J1233.3+6910

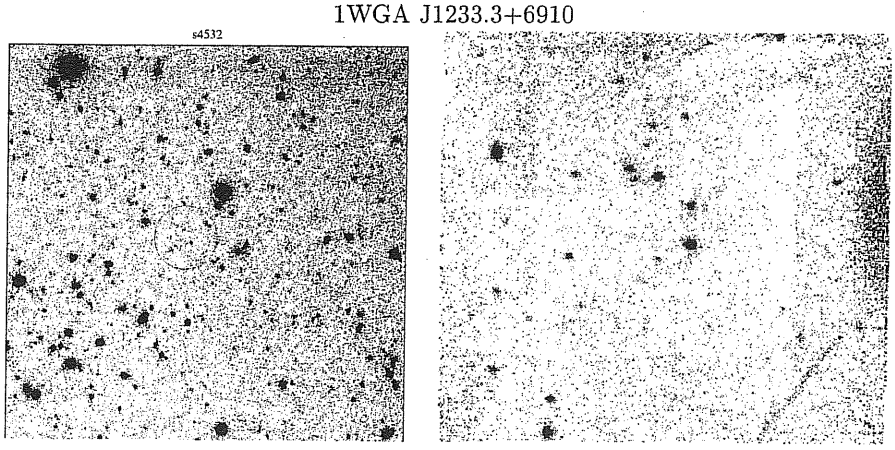

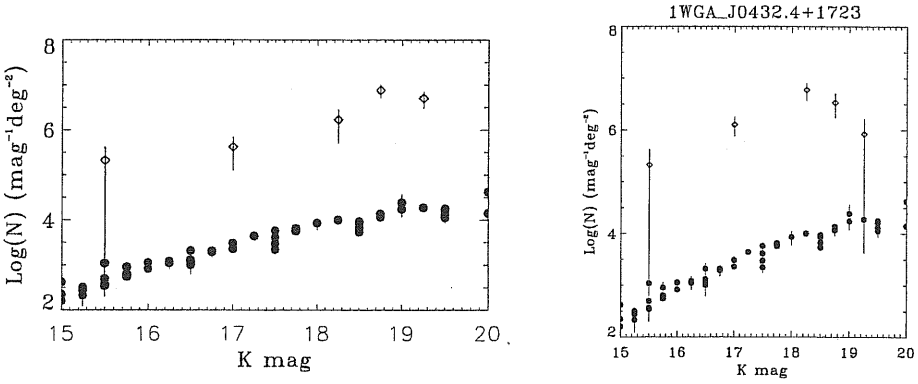

Figure 4.3: K-band number counts in the field of view of 1WGA J1226.9+3332 (left) and 1WGA J0432.4+1723 (right) (open symbols) compared to field counts (filled symbols) (see text).

Chapter 5

Notes on individual sources

This chapter includes all the available information for the blank field sources at the moment of writing. It is to note that all the sources were originally unidentified when the sample was first selected, but some of them were studied (and in some cases identified) by other groups in the three years during which we progressed their investigation.

5.1 Probable clusters of galaxies

5.1.1 1WGA J0221.1+1958

1WGA J0221.1+1958 was identified in the SHARC survey (Romer et al. 2000) as a $z = 0.45$ cluster of galaxies, and assuming a $T \sim 6$ keV, they derived from a *ROSAT* count rate of 0.02211 counts s^{-1} an X-ray luminosity of $L_{X(0.5-2.0)} = 2.87 \times 10^{44}$ erg s^{-1} (H_0=50 km s^{-1} Mpc^{-1} and $q_0 = 0.5$).

5.1.2 1WGA J0432.4+1723

This source was found by Carkner et al. (1996) in the outer PSPC region (offset $\sim 37'$) of a 1993 observation (rp900353n00) of Lynds 1551, a well-studied cloud in the Taurus-Auriga star forming region. They found a 7σ source with $CR = 1.9 \times 10^{-2}$ counts s^{-1}. Even though they do not make a clear identification, the source is first included among the sample of possible T Tauri stars, young low-mass stars just emerged from their obscuring dusty cloud and approaching the main-sequence. The X-ray emission for T Tauri stars is attributed to optically thin plasma trapped in closed magnetic structures and heated by magnetic processes (e.g. reconnection). This emission is usually modeled as ~ 1 keV optically thin plasma, even though few T Tauri stars have large emission measures at higher temperatures (e.g. Koyama et al. 1994). The authors do not find any evidence for H_α emis-

sion and/or Li 6707 Å absorption, typical of T-Tauri stars and the proper motion of the source they measured is inconsistent with being part of the cloud. They conclude that 1WGA J0432.4+1723 is likely to be unrelated to the cloud itself. 1WGA J0432.4+1723 was also detected, but not classified, in the analysis of *ROSAT* All Sky Survey by Wichmann et al. 1996.
In a 1991 observation (rp200443n00), the source falls in the inner PSPC detector region. The $\sim$ 2.5 times longer exposure time and the sharper PSPC PSF in the inner circle give more precise results than in Carkner et al. (1996). We find a (0.5-2.0 keV) count rate of $(1.42 \pm 0.1) \times 10^{-2}$ counts s^{-1} and a position of 04:32:29.5 +17:23:45.4, in agreement with Galpipe position. We were also able to extract and fit a spectrum (Fig 3.2). The fit with a black body model suggests a temperature of $\sim 0.55 \pm 0.01$ keV, somewhat lower than the $\sim$ 1 keV expected for a T Tauri star but not conclusive due to the patchy nature of the ISM in this area. A NVSS radio source with flux at 1.4 GHz equal to 3.2 ± 0.6 mJy is present $\sim 17''$ from the 1WGA J0432.4+1723 PSPC position. Radio continuum emission is often observed for T-Tauri stars at a level of 10^{15} - 10^{18} erg s^{-1} Hz^{-1} and (assuming a distance of 140 pc for L1551, similar to the other Taurus-Auriga star forming clouds (e.g. Carkner et al. 1996), the NVSS radio flux of 3.2 mJy corresponds to a luminosity $\sim 10^{17}$ erg s^{-1} Hz^{-1}. The NVSS flux is fully consistent with the emission from a T-Tauri star, however the proper motion and the energy spectrum of the source as reported in Carkner et al. (1996) exclude the possibility of a new T-Tauri star.

We propose a high redshift cluster classification for 1WGA J0432.4+1723 on the basis of the lack of variability and the presence of an IR-bright extremely red galaxy in the error circle, and an excess of similarly red sources nearby. Although the PSPC spectrum does not discriminate between different spectral models[1] we present here strong evidence for the high-redshift-cluster nature of 1WGA J0432.4+1723 by means of its X-ray and optical-IR properties.

1WGA J0432.4+1723 was observed by ROSAT in 1991 and in 1993. The source is persistent (thus excluding the Gamma Ray Burst possibility) and does not show evidence for variability on a 6-hour timescale (the longest timescale sampled, corresponding to the 1991 observation)[2].

[1] An absorbed power-law model and a redshifted Raymond-Smith model with absorption fixed to the Galactic value give equally good fits

[2] In 1993 the source is detected in the outer rim and spread over a large area and a variability study is not possible due to the low signal to noise. The count rate, however, is consistent with that of 1991 observation

Bright IR galaxy in the error circle

Both 1WGA J0432.4+1723 and the high z cluster 1WGA J1226.9+3332 have a bright K-band counterpart (K$\sim$ 15.3, dereddened for the Galactic N_H = 1.68×10^{21} cm^{-2}, for 1WGA J0432.4+1723; K=15.5 for 1WGA J1226.9+3332) in the X-ray error circle (Fig. 4.2). These objects are clearly classified as galaxies using the Kron radius (Bertin & Arnouts 1996) to separate between galaxies and stars. If these galaxies were first ranked cluster ellipticals with $M_K = -26.7 \pm 0.5$ (assuming negligible K-correction, $q_0 = 0.5$ and , H_0=50 km s^{-1} Mpc^{-1} as in Collins & Mann, 1998), we would have a limit on the redshift: $z = 0.60^{+0.25}_{-0.16}$ for 1WGA J0432.4+1723 ($z = 0.68^{+0.30}_{-0.19}$ for 1WGA J1226.9+3332).

The IR bright galaxies are red

The optical image in R shows that the bright IR galaxies in the error circles of 1WGA J0432.4+1723 and of the high z cluster 1WGA J1226.9+3332 are extremely red ($R - K \sim 5.2 \pm 0.5$[3] for 1WGA J0432.4+1723 and 5.1 ± 0.3 for 1WGA J1226.9+3332) (Fig. 4.2, as expected from obscured AGNs and high z clusters of galaxies. Only an unevolving elliptical galaxy at 0.75 <z< 1.1 or a Sbc galaxy at z> 1.2 can have such red color (Coleman, Wu & Weedman, 1980). ($0.75 < z < 1.0$ are the limits for the high z cluster 1WGA J1226.9+3332).

K-band counts excess

Comparing R and K-band images (Figure 4.2), it is clear that there are many more objects detected in the K- than in the R-band both in the field of 1WGA J0432.4+1723 and of the high z cluster 1WGA J1226.9+3332 (Figure 4.3). We generated K-band galaxy number counts in our field in the range $15 < K < 19.5$, and compared them with those obtained from the near-IR field surveys in the same range (Gardner et al. 1993, Saracco et al. 1997, Huang et al. 1997, Minezaki et al. 1998, Huang et al. 2000) in Figure 4.3 (right). The number counts obtained for 1WGA J0432.4+1723 (open symbols) are substantially higher ($> 7\sigma$ at K=18) than those from the field surveys (filled symbols). Such a large excess cannot be due to Poisson statistics or magnitude errors. We also note that the extended sources (according to the Kron radius method) in the FOV of 1WGA J0432.4+1723 have similar red colors (filled circles in Figure 5.1). There is a clear segregation in colors between point-like sources (stars, open circles in Figure 5.1) and extended sources (galaxies). The galaxies have similar R-K color around R-K=4.5,

[3]R and K magnitude were dereddened for the Galactic N_H

meaning that they may belong to a cluster. The colors have been corrected for the high Galactic absorption ($N_H = 1.68 \times 10^{21}$ cm^{-2}), while the R (left) and K (right) magnitudes represented on the x axes are uncorrected.

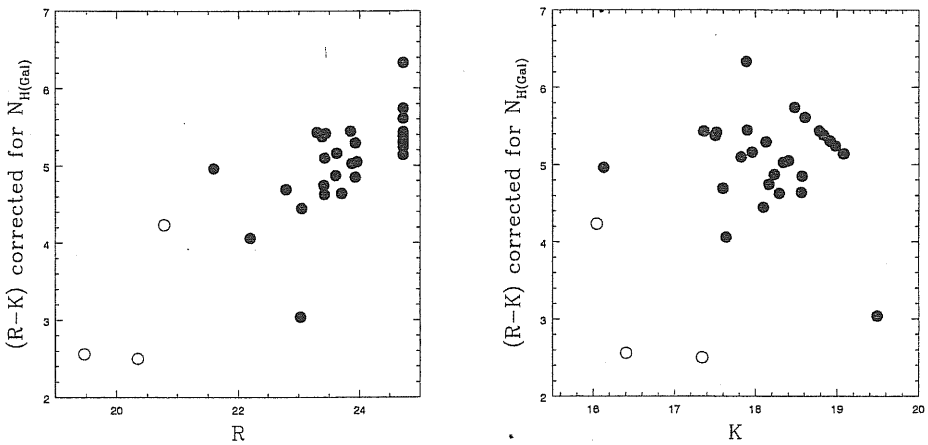

Figure 5.1: Color-magnitude plot for the 1WGA J0432.4+1723 field. The filled circles represent extended sources and the open circles are the point-like source. There is a clear segregation in colors between point-like sources (stars) and extended sources (galaxies).

Any doubt on the high z cluster nature?

(1) - 1WGA J0432.4+1723 is close to the Taurus-Auriga star forming region Lynds 1551 (Carkner et al. 1996). Could this rise some doubts on the high redshift cluster nature of 1WGA J0432.4+1723?
Could the excess of (red) sources in the K-band image be due to the high density of forming stars?
Even if we assume that all the red sources near the bright galaxy are all new T-Tauri stars[4] and that the galaxy is a background galaxy reddened by the star forming cloud along its line of sight, we could not explain its extreme X-ray loudness.
(2) - Could the absence of the Palomar counterpart and the redness of the galaxy present in 1WGA J0432.4+1723 error circle be due to the high Galactic absorption (~10 times larger than that of 1WGA J1226.9+3332)?

Even if we take into account the absorption due to the Galactic N_H ($A_V \sim 0.92$, $A_R \sim 0.7$ and $A_K \sim 0.3$), 1WGA J0432.4+1723 is still an extremely X-ray loud source and the redness of the counterpart is real because both the R and K band magnitudes have been corrected accordingly.
The identification of 1WGA J0432.4+1723 with a luminous high redshift cluster of galaxies is the only option that accounts for all the observational constraints.

[4]These objects are too faint to perform a morphological classification

5.1.3 1WGA J1103.5+2459

1WGA J1103.5+2459 is listed in Romer et al. (2000) as an extended source detected in the SHARC survey with a (wavelet) count rate of 0.00411 counts s^{-1}, but it is not yet identified and it is not included in the SHARC cluster sample. This source has a red counterpart ($R - K \sim 5.5 \pm 0.5$) in its error circle and thus it could be another high redshift cluster of galaxies or an absorbed AGN. If the red counterpart is the first ranked elliptical of a cluster, a $R - K \sim 5.5$ would suggest $z \sim 1$ (Coleman, Wu & Weedman 1980), in agreement with the $z \sim 0.9$ suggested (Collins & Mann 1998) by the K-band magnitude of the source ($K = 16.2 \pm 0.3$).

5.2 Probable AGNs

5.2.1 1WGA J1220.3+0641

1WGA J1220.3+0641 was detected in the *ROSAT* all-sky survey and it is listed in the Bright Source Catalog (BRASS, Voges et al. 1999) with a broad band $CR = 0.079 \pm 0.017$ counts s^{-1}. Using the whole 0.07- 2.4 keV ROSAT band we derive a $CR = 0.098 \pm 0.006$ counts s^{-1} consistent with the RASS detection. Its position in the BRASS catalog is 14″ from the Galpipe position and 10″ from the HRI position . The HRI and Galpipe positions for this source are only 4″ apart. Since 1WGA J1220.3+0641 is a persistent source we can exclude a Gamma Ray Burst origin.

1WGA J1220.3+0641 was detected as an unidentified serendipitous source in 1995 by the *ASCA* GIS with a 1-10 keV count rate of 0.0142 ± 0.09 (George et al. 2000). This source is also included in the ASCA Medium Sensitivity Survey (AMSS) (Ueda et al. 2001) with the name 1AXG J122017+0641. In the AMSS the source has a count rate of 0.0214 counts s^{-1} in the 0.7-7.0 keV band; corresponding to a flux, corrected for the Galactic absorption, of 1.4×10^{-12} erg cm^{-2} s^{-1}, with most of the flux (1.04×10^{-12} erg cm^{-2} s^{-1}) lying in the 2-10 keV band. The AMSS hardness ratio (calculated using the corrected count rates in the 0.7-2 keV and 2-10 keV bands) is -0.1 ± 0.04, which makes 1WGA J1220.3+0641 a hard source.

A Raymond-Smith model provides a poor description of the source with the temperature pegging at the hard limit both for the fit to the *ASCA* GIS2 (1.0-8.0 keV) and GIS3 (1.5-10.0 keV) and to the combined *ROSAT* PSPC (0.07-2.4 keV) and the *ASCA* GIS2 and GIS3 data.

An absorbed power law model with absorption fixed to the Galactic value (1.56×10^{20} cm^{-2}; a free absorption does not improve the fit) better describes the source: the simultaneous fit of *ROSAT* PSPC and *ASCA* GIS2

and GIS3 spectra gives a best fit photon index of 1.18 and a normalization of 3.38×10^{-4} photons cm^{-2} s^{-1} keV^{-1} at 1 keV, with a reduced χ^2 of 2.608 (56 d.o.f.). The data and the unfolded spectra fitted with an absorbed power law model are presented in Figure 5.2.

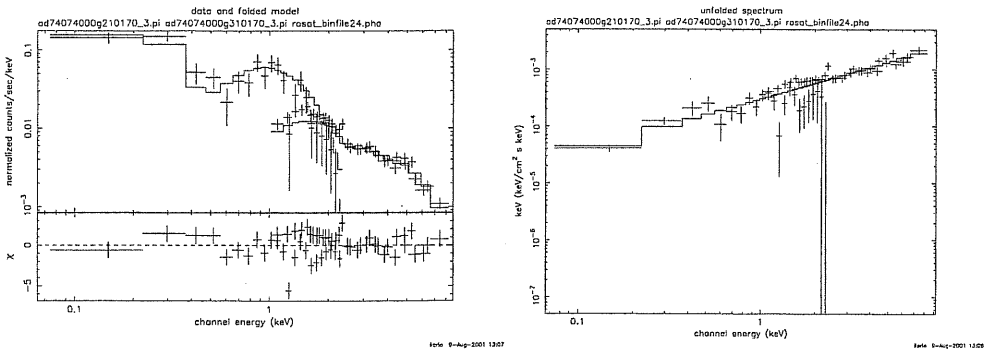

Figure 5.2: Left: *ROSAT* PSPC and *ASCA* GIS2 and GIS 3 spectra of 1WGA J1220.3+0641 and residuals to the fit with a powerlaw with absorption fixed to the Galactic value. Right: *ROSAT* - *ASCA* spectrum in the $\nu - F\nu$ plane.

ASCA GIS2 and GIS3 data alone give consistent values of $\Gamma = 1.31 \pm 0.58$ and normalization of 4.16×10^{-4} photons cm^{-2} s^{-1} keV^{-1} at 1 keV, with a reduced χ^2 of 0.79 (33 d.o.f.). If the absorbed power law is a correct model to describe the spectrum of the source, 1WGA J1220.3+0641 is not absorbed and looks like a normal type 1 AGN: the faintness of its optical counterpart is still a mystery. The *ASCA* archival lightcurves, which do not show any strong variability occurring within the source, are shown in Figure 5.3.

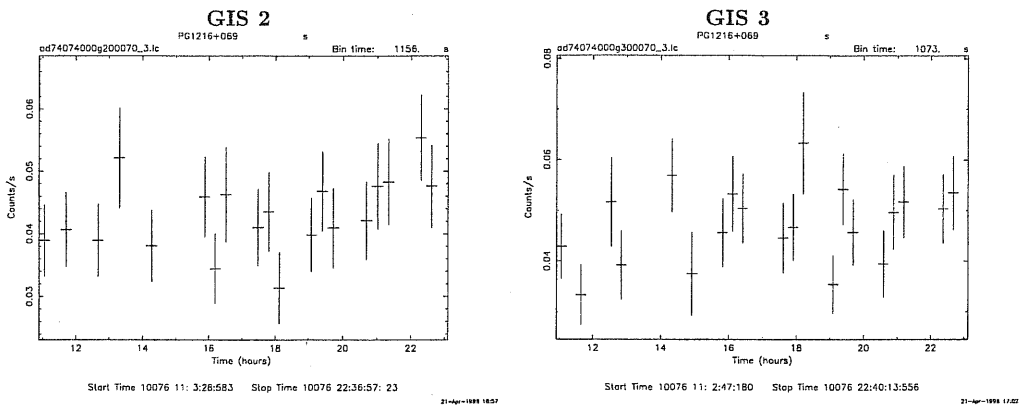

Figure 5.3: *ASCA* GIS2 (left) and GIS3 (right) archival lightcurves of 1WGA J1220.3+0641.

The Palomar plates show the presence of a O=21.81 and E=18.58 red (O-E=3.23) source within 1WGA J1220.3+0641 error circle. The large redness of this source (O-E=3.23) suggests a strongly obscured local source ($A_V \sim 6$) or moderate to Galactic obscuration for a $z \sim 3 - 4$ quasar. The brightest

counterpart we found in our R and K-band imaging has $R = 17.6$ and $K = 13.6$, again showing a red color ($R-K \sim 4$). A local source with (O-E=3.23) would be strongly obscured ($A_V \sim 6$) but this color can be reconciled with moderate to Galactic obscuration in the case of a high redshift AGN ($z \sim 3-4$) or assuming an extreme dust to gas ratio ~ 50 larger than the Galactic value for solar metallicity (≥ 100 for $Z = 3Z_\odot$, Maiolino et al. 2001). If 1WGA J1220.3+0641 were at $z \sim 3-4$ its unabsorbed X-ray luminosity would be $L_{(2-10\mathrm{keV})} \sim 3-5 \times 10^{46}$ erg s^{-1}. We discuss the other open possibilities in § 7.

5.2.2 1WGA 1412.3+4355

This source has been classified as an AGN at $z \sim 0.59$ in the RIXOS survey (Mason et al. 2000) on the basis of one optical broad emission line identified with the Mg II line. It has a RIXOS (0.5 - 2.0 keV) count rate of 0.0055 ± 0.006 counts s^{-1}, smaller than 0.099 ± 0.016 counts s^{-1} we found and than the WGCAT95 count rate (0.011 ± 0.001 counts s^{-1}). The X-ray photon spectral slope is 2.20 ± 0.15 (c.f. 2.1 ± 0.1 in the RIXOS) consistent with a normal type 1 AGN and does not show absorbing column in excess of the Galactic value ($N_{H(\mathrm{Gal.})} = 1.17 \times 10^{20}$ cm^{-2}). 1WGA 1415.2+4403 is not variable in the PSPC observation but there are no other observations for this source.

It is difficult to reconcile a normal type 1 AGN nature as derived from optical spectroscopy (Mason et al. 2000) with the extreme X-ray loudness of this source: 1WGA 1412.3+4355 is the most extreme source in our sample with $f_X/f_V > 100$ and $f_X/f_R > 10$, not compatible with any know class of X-ray emitters.

The Palomar plates show a E=18.73 source within the error circle, but no objects are detected in the O-band. Our R and K band imaging does not show a red source or the presence of red counterparts in the error circle **check this when computing the K-band magnitude....but this is what looks to the eye** From the Palomar, assuming a limit of O>21.5, we obtain a color of O-E> 2.77, corresponding to $A_V > 4$ at $z = 0.59$ when the quasar spectral shape of Francis et al. (1991) is adopted (e.g. Figure 7.1).

We do not have a clear answer on what is the reason of the peculiarity of this source, but we can suggest one of the following possibilities:
- the source experienced an extreme long timescale variability as happened to the BL Lacertae object 1WGA J1340.1+2743 (see § 6.1) (short time scale variability is excluded by the PSPC observation);
- the optical absorption suggested by Palomar colors could be explained assuming an higher than Galactic dust to gas ratio for the obscuring material,

opposite to what found by Maiolino et al. (2001). The Galactic N_H and the A_V from Palomar colors imply a $\sim$ 50 larger than Galactic dust to gas ratio for solar metallicity and $\sim$ 100 larger for 3 times the solar metallicity (Maiolino et al. 2001). The main problems with this idea are (1) such dust to gas ratio is difficult to justify and (2) due to the dust obscuration, we would expect a type 2 classification in the optical band, in disagreement with the broad line seen in the RIXOS spectrum (Mason et al. 2000);
- the optical emission is not reddened but intrinsically faint. This can be caused by the shift of the BBB at higher energies or by suppressed BBB emission as in the case of ADAFs.
We will discuss these possibilities in § 7.

5.2.3 1WGA 1415.2+4403

Also 1WGA 1415.2+4403 is included in the RIXOS survey (Mason et al. 2000) and classified as a $z = 0.562$ AGN with a (0.5 - 2.0 keV) count rate of 0.0033 ± 0.0005 counts s^{-1}, comparable to our count rate (0.0030 ± 0.0006 counts s^{-1}). The X-ray photon spectral slope is $2.70^{+0.22}_{-0.20}$ (2.3 ± 0.1 in the RIXOS) consistent with a normal type 1 AGN and there are no signs of absorption in the X-ray spectrum. As for 1WGA 1415.2+4403, there are no other observations and the source is not variable in the PSPC observation. No sources are found in the Palomar O and E bands within the X-ray error circle. We note that the WGACAT95 flux was $\sim$ 50% overestimated and this source is, as a consequence, one of the least extreme sources in our sample; the f_X/f_V is $\sim$ 5 and $f_X/f_R \sim 1$, both consistent with the tail of normal type 1 AGNs.

5.2.4 1WGA J1416.2+1136

This source was found in the Cambridge Cambridge ROSAT Serendipitous Survey (CRSS, Boyle, Wilkes & Elvis 1997) with a (0.5-2.0 keV) X-ray flux of 5.2×10^{-14} erg cm^{-2} s^{-1}, using a constant conversion factor of 1 count s^{-1} = 1.2×10^{-11} erg cm^{-2} s^{-1}, implying a count rate of 0.433×10^{-2} counts s^{-1}, larger than our $CR = (0.31 \pm 0.08) \times 10^{-2}$ counts s^{-1}. In the *ROSAT* HRI the count rate is consistent with PIMMS estimate based on the PSPC count rate suggesting a constant source over a 4-year period and excluding an extremely variable nature for 1WGA J1416.2+1136. Also for this source the WGACAT was overestimates ($\sim$ 60%) and the source is thus less extreme than previously though.

On the Palomar Observatory sky survey there is a O=22.22 and a E=19.50 source 12.8″ from the HRI position. The redness of the source O-E=2.72

implies $A_V \sim 5$, corresponding to $N_H \sim 10^{22}$ cm^{-2}, while the *ROSAT* spectrum is consistent with Galactic absorption. The X-ray photon spectral index is $2.68^{+0.27}_{-0.24}$, consistent with a normal type 1 AGN. The X-rays and Palomar data can be reconciled if we assume an extreme dust to gas ratio ($\sim$ 50 larger than Galactic value for $Z = Z_\odot$ or ≥ 100 for $Z \doteq 3Z_\odot$; Maiolino et al. 2001)

5.2.5 1WGA J1535.0+2336

This source was detected by *Einstein* IPC as an ultra-soft source (Thompson et al. 1998) with a CR= 0.003636 ± 0.000964 counts s^{-1}, in good agreement with the *ROSAT* PSPC count rate using the best fit values for an absorbed power law model as in Table 3.3. The *Einstein* and Galpipe positions are 17″ apart and thus consistent. The X-ray spectral slope ($\Gamma = 0.70^{+0.72}_{-1.05}$) is consistent within the large errorbars with a type 1 AGN. 1WGA J1535.0+2336 WGACAT95 flux was $\sim$ 90% overestimated and this source too belong to the least extreme group of our blank field sources. A O=21.79 and E=19.61 source is visible in the Palomar within 1WGA J1535.0+2336 error circle. The O-E=2.18 implies $A_V \sim 4$ for a local source and $N_H \sim 8 \times 10^{21}$ cm^2 assuming Galactic dust to gas ratio, while the X-ray fit does not show the need for extra absorption. An extreme dust to gas ratio ($\sim$ 50 the Galactic value for $Z = Z_\odot$ or ≥ 100 for $Z = 3Z_\odot$; Figure 7.2) could reconcile the X-ray and Palomar data. We will discuss this and the other possibilities in § 7.3. Our R and K band imaging show a faint counterpart in the error circle; this counterpart is not particularly red **write R -K here, consistent (not consistent) with $A_V \sim 4$ if we assume a ?? spectral shape. A larger redshift or an higher than Galactic dust to gas ratio could reconcile the X-ray and optical data. What about R and K??**

5.3 Unknown nature

5.3.1 1WGA J1220.6+3347

1WGA J1220.6+3347 was detected by the *Einstein* IPC as an ultra-soft source (Thompson et al. 1998) with a CR= 0.0121385 ± 0.00218474 counts s^{-1}. The *Einstein* and Galpipe PSPC positions are 22″ apart and so are consistent.

Since 1WGA J1220.6+3347 was seen on a > 10 year interval the Gamma Ray Burst hypothesis is excluded.

This source has a soft X-ray spectral index $\Gamma \sim 2.3$ and lack of a red counterpart; the high z cluster and the obscured AGN nature are highly

unlikely for this source.

5.3.2 1WGA J1233.3+6910

This source is listed in Radecke (1997) with a position of 12:33:23.69 +69:10:05.5 and $CR = 0.0225$ counts s^{-1}. For the same observation we found a position of 12:33:23.9 + 69:10:10.1 and $CR = 0.0214 \pm 0.0013$ counts s^{-1}. In the HRI field the source is visible (excluding the Gamma Ray Burst origin) but it falls on the detector edge, making any flux and positional estimate unreliable.

Also for this source, the soft X-ray spectral index $\Gamma \sim 2.4$ and the lack of a red counterpart in the error circle make the high z cluster and the obscured AGN possibilities unlikely.

5.3.3 1WGA J1243.6+3204

This source was detected by Vogler et al. (1996) in the same observation as the brightest *ROSAT* source within the optical extent of the edge-on spiral galaxy NGC 4656 (z=0.00215). It is located to the south-west, at $\sim 7.6'$ from the nucleus along the major axis (12:43:41.03 +32:04:54.8). In this region there is a deficiency in X-ray emission, probably related to the cold gas of the HI which bridges the space between NGC 4656 and its tidally interacting companions. Vogler et al. (1996) estimated for 1WGA J1243.6+3204 a 0.1-2.4 keV count rate of $CR = (9.3 \pm 0.8) \times 10^{-3}$ counts s^{-1} corresponding to $F_X \sim 1.3 \times 10^{-13}$ erg cm^{-2} s^{-1} (0.1-2.4 keV); the N_H value from Vogler et al. (1996) fit is in excess of 5×10^{21} cm^{-2}, both for a thin thermal plasma and for a power law model. The absorbing column is larger than the HI density within NGC 4656 in the viewing direction of 1WGA J1243.6+3204 which is about $8 \times 10^{20} cm^{-2}$. There is a 0.3% probability for this 'blank' to be a background X-ray source. Vogler et al. investigate the possibility that 1WGA J1243.6+3204 is a heavily absorbed source within NGC 4656, e.g. a X-ray binary. In this case, $L_X \sim 8 \times 10^{38}$ erg s^{-1} and the source would be radiating well above the Eddington limit for a one solar mass system. Similar sources have been found in other galaxies (e.g Fabbiano 1989, Fabbiano et al. 2000). X-ray binaries would have faint optical and IR counterparts.

We find a position and a count rate consistent with Vogler et al. (1996). Fitting the spectrum with an absorbed power law in the range 0.07 – 2.40 keV, we find an absorbing column of $1.71^{+1.50}_{-0.78} \times 10^{21}$ cm^2, clearly in excess of the Galactic absorption ($\sim 1.23 \times 10^{20}$ cm^{-2}) and of the column density within NGC 4656 in the viewing direction of 1WGA J1243.6+3204 ($8 \times 10^{20} cm^{-2}$). 1WGA J1243.6+3204 was also serendipitously observed in the

ROSAT HRI in a $\sim$ 27 ks long observation performed in 1994, two years after the PSPC one. From the HRI image the source looks pointlike with a position of 12:43:41.1 +32:04:56.6 and a count rate of $CR = (3.62 \pm 0.50) \times 10^{-3}$ counts s^{-1}, which is slightly smaller than expected from the PSPC fits. The HRI and PSPC count rates can be reconciled within $1\dot{\sigma}$.

The same HRI image was also analyzed by Roberts & Warwick (2000) and 1WGA J1243.6+3204 is detected as a serendipitous source with a count rate of 0.030 ± 0.004 counts s^{-1}.

Chapter 6

Chandra view of blank field sources

This chapter presents the results of the *Chandra* observations we obtained, with particular relevance to the high redshift cluster of galaxies 1WGA J1226.9+3332 (§ 6.2).

We obtained *Chandra* observations for 4 blank field sources so far: two 10-ks long observations; one for 1WGA J1226.9+3332 (Cagnoni et al. 2001) and one for 1WGA J1340.1+2743 and two more 3-ks snapshots for 1WGA J0951.4+3916 and 1WGA J1420.0+0625, which have been recently released to us and are not presented in this thesis. Three more 3-ks *Chandra* snapshots (for 1WGA J0221.1+1958, 1WGA J1220.6+3347 and 1WGA J1233.3+6910) and two 10-ks observations with *XMM-Newton* (1WGA J1216.9+3743 and 1WGA J1220.3+0641) were approved. We detail on the performed observations in the following subsections.

6.1 1WGA J1340.1+2743

1WGA J1340.1+2743 was observed 7 times with the PSPC, only once in the inner circle. We extracted a combined image and spectrum. This source is close ($\sim 7'$) to the bright Seyfert 2 galaxy CC B00 (1RXS J134021.4+274100) which has ~ 2 times the PSPC count rate of 1WGA J1340.1+2743. Due to slight displacements in the source positions as detected in different images and to the broader PSF in the outer regions of the PSPC detector, 1WGA J1340.1+2743, in the combined image, is contaminated by the nearby bright source and this image is not suitable for variability studies or flux estimates. However by using a portion of the source from the side of the source away from the quasar a higher signal to noise spectrum than in WGA

detection alone can be obtained.

1WGA J1340.1+2743 was unidentified in WGACAT95, but it was identified as a BL Lacertae object in Lamer, Brunner & Staubert (1997) because of lack of spectral features in its optical spectrum. Lamer et al. find an X-ray flux at 1 keV of 2.06×10^{-14} erg cm^{-2} s^{-1}. This value is 50% smaller than the 3.07×10^{-14} erg cm^{-2} s^{-1} we find for the detection in the inner PSPC circle (rp701069n00). 1WGA J1340.1+2743 has a radio counterpart $\sim 10''$ from the PSPC position with a 1.4 GHz flux of ~ 4 mJy (NVSS=4.6 ± 0.5 mJy; FIRST= 3.75 mJy). Together with the R magnitude ($R \sim 22$, Lamer et al. 1997), converted into V magnitude assuming $V - R \sim 0.65$ (Moles et al. 1985), we find broad band spectral indices $\alpha_{RO} = 0.62$ and $\alpha_{OX} = 0.61$. This values are extreme for X-ray selected BL Lacertae objects (Figure 3.6) and the f_X/f_V for this object is ~ 300 again, not compatible with known BL Lacertae objects. We could explain such f_X/f_V if we assume that this source is an extreme BL Lacertae object (e.g. Costamante et al. 2001) with the synchrotron peak lying, in quiescence, at energies higher than the *ROSAT* band, e.g. 10 keV. Figure 6.1 from Costamante et al. (2001) shows the α_{ox}-α_{rx} plane as a function of the peak frequencies for known BL Lacertae objects. The values for 1WGA J1340.1+2743 ($\alpha_{ox} = 0.61$, $\alpha_{rx} = 0.62$ red dot in Figure 6.1) are consistent with the source being an extreme BL Lacertae object and the X-ray spectral slope ($\Gamma = 2.35 \pm 0.18$) is similar to what found with *Beppo-SAX* by Costamante et al. (2001) for extreme BL Lacs.

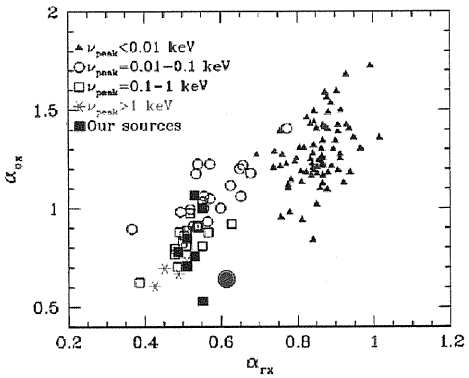

Figure 6.1: (From Costamante et al. 2001) The plane α_{ox}–α_{rx} for the SLEW sample of BL Lacs, the 1 Jy sample of BL Lacs and the 2 Jy sample of FSRQs. All sources with $\alpha_{rx} < 0.7$ are X–ray selected BL Lacs. The SED of all sources has been fitted with a cubic function in order to find the synchrotron peak frequency $\nu_{\rm peak}$ (Fossati et al. 1998). Filled squares mark the location of the extreme BL Lacs in Costamante et al. (2001). The red big circle represents 1WGA J1340.1+2743.

Another possibility is that 1WGA J1340.1+2743 is an "average" X-ray

selected BL Lacs, but it was experiencing a large flaring activity during the WGACAT95 detection: a factor of 10-30 variation has been observed in X-ray selected BL Lac (e.g. MRK 501, Pian et al. 1998) and a 10 times smaller "quiescent flux" would drastically lower the f_X/f_V down to ~ 20, a normal value for BL Lacs. This hypothesis, however, is not confirmed by the PSPC lightcurve, where no dramatic changes in the X-ray flux are visible, but we note that 1WGA J1340.1+2743 was a factor of 2 brighter than in Lamer, Brunner & Staubert (1997).

With the aim of understanding the extreme properties of this source we asked for a 10 ks *Chandra* observation. The data reduction was performed as in § 6.2. Figures 6.2 and 6.3 show the *Chandra* spectrum and lightcurve (with binning factor of 200 and 500 s respectively).

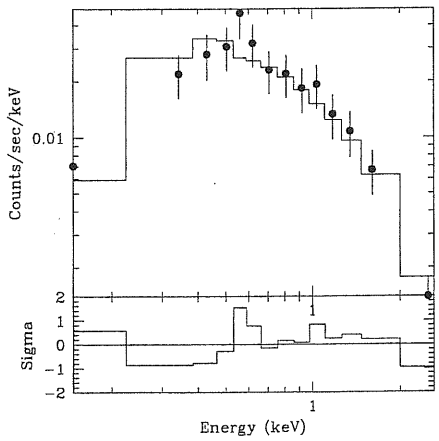

Figure 6.2: *Chandra* Energy spectrum of 1WGA J1340.1+2743 with the best fit absorbed power law model (see text)

The $\sim$ 300 counts accumulated in this observation are not enough for the spectrum to discriminate between different models. We fitted it with an absorbed power law model and the best fit values are: $N_H = 2.7^{+2.1}_{-1.1} \times 10^{20}$ cm^{-2}, photon index $\Gamma = 2.16^{+0.26}_{-0.30}$ and normalization of $(2.64 \pm 0.52) \times 10^{-5}$ phot cm^{-2} s^{-1} keV^{-1} at 1 keV, with a χ^2 of 6.65 for 11 d.o.f.; the count rate is 0.031 counts s^{-1} and corresponds to a 0.5-10.0 keV flux of 8.69×10^{-14} erg cm^{-2} s^{-1}(5.37×10^{-14} and 3.31×10^{-14} erg cm^{-2} s^{-1} in the energy ranges 0.5-2.0 keV and 2.0-10.0 keV respectively). Freezing the column density to the Galactic value ($N_H = 1.09 \times 10^{20}$ cm^2) we obtain $\Gamma = 1.89^{+0.22}_{-0.26}$ and normalization of $(2.39 \pm 0.48) \times 10^{-5}$ phot cm^{-2} s^{-1} keV^{-1} at 1 keV and a χ^2 of 10.09 for 12 d.o.f..

Even if the spectral shape is consistent with the one measured by *ROSAT* the source is $\sim$ 10 times fainter in the 0.5 -2.0 keV band, thus explaining

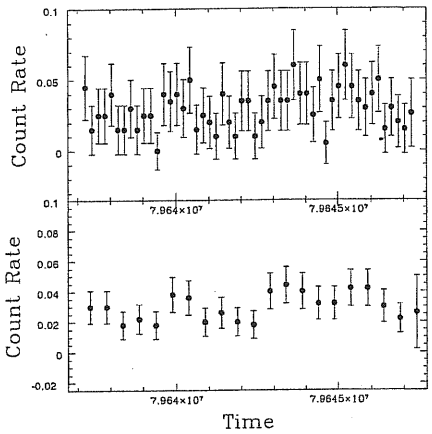

Figure 6.3: *Chandra* lightcurve of 1WGA J1340.1+2743 with a bin size of 200 s (top) and 500 s (bottom)

the extreme X-ray loudness of the source in the *ROSAT* observation.

6.2 1WGA J1226.9+3332: a high redshift cluster of galaxies

This source is listed in Radecke (1997); using our same PSPC data, he found a count rate of 2.20×10^{-2} counts s^{-1} slightly smaller than ours, $(2.66 \pm 0.16) \times 10^{-2}$ counts s^{-1}. In the HRI image the source is faint with a count rate of $CR = (7.94 \pm 1.51) \times 10^{-3}$ counts s^{-1}, in agreement with PIMMS predictions based on the PSPC observations, indicating a non-variable source over a 4-year period. Short term variability is not visible in the 2 PSPC observations taken two weeks apart. In the HRI image 1WGA J1226.9+3332 looks extended, suggesting a cluster of galaxies.

1WGA 1226.9+3332 was one of two 'blanks' for which we obtained Cycle 1 *Chandra* (Weisskopf et al., 1996) observing time. It was observed in ACIS-S configuration (Garmire et al., in prep.) with the backside illuminated S3 chip for a total useful exposure time of 9832.3 s. The data was cleaned as described in Markevitch et al. (2000a) and for the spectral and image analysis we used the latest available ACIS background dataset (Markevitch et al. 2000b).

6.2.1 Spatial analysis

To maximize the signal-to-noise ratio, we extracted the image in the 0.5-5 keV band (Fig. 6.4). Along with a number of faint point-like sources, 1WGA 1226.9+3332 is clearly seen as an extended source on an arcminute

scale. It shows azimuthal symmetry, except for a possible excess to the north-west, $\sim 40''$ from the cluster center.

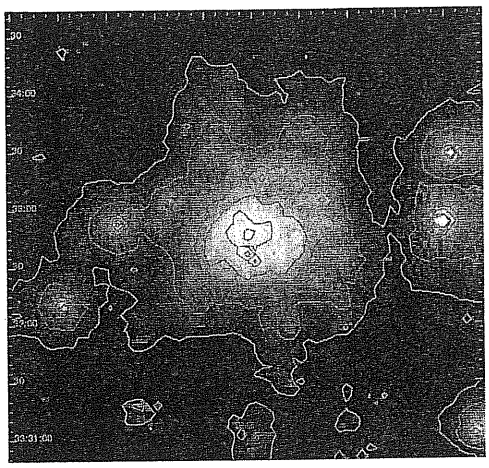

Figure 6.4: *Chandra* view of 1WGA J1226.9+3332: zoom of the cluster (smoothed and background subtracted).

After subtracting the background, from the same regions in a normalized ACIS background map (Markevitch et al. 2000b), we extracted the X-ray surface brightness profile (Fig. 6.5) in concentric annular regions centered on the X-ray emission peak and chosen in order to have 20 counts per annulus. The profile appears to be smooth without any obvious central excess related to a cooling flow (Figs. 6.4 and 6.5). We fitted the surface brightness profile with a standard β model [1] (Cavaliere & Fusco-Femiano 1976) using the *Sherpa* (Siemiginowska et al., in prep.) modeling and fitting tool from the CXC analysis package CIAO 2.0 (Elvis et al., in prep.). We obtained best fit values of $\beta = 0.770 \pm 0.025$, $r_c = (18.1 \pm 0.9)''$ (corresponding to 101 ± 5 kpc at $z = 0.89$), and $S(0) = 1.02 \pm 0.08$ counts arcsec^{-2} with a χ^2 of 27.5 for 26 degrees of freedom (d.o.f.). The excess to the north-west of the cluster is also visible in the radial profile; a drop of the surface brightness at $\sim 40''$ is present in the radial profile for the north-west sector. Similar features in the surface brightness radial profiles were detected by *Chandra* in nearby clusters (e.g. Markevitch et al. 1999;2000a;2001, Vikhlinin et al. 2001; Mazzotta et al. 2001) and interpreted as signs of sub-clump motion.

6.2.2 Spectral analysis

We extracted an overall spectrum in a circle with $r = 120''$ in the 0.5-10 keV band in PI channels, corrected for the gain difference between the different regions of the CCD. The spectrum (Fig. 6.6) contains ~ 1100 net counts and

[1] $S(r) = S(0)[1 + (r/r_c)^2]^{-3\beta+1/2}$

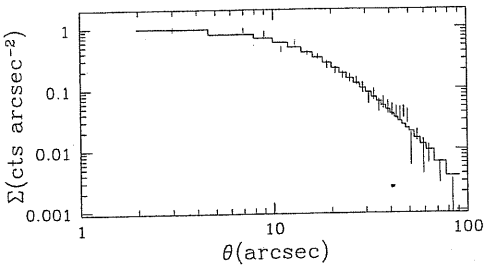

Figure 6.5: Background subtracted surface brightness radial profile of 1WGA J1226.9+3332 (error bars) together with the best fit β-model (see text).

we binned it in order to have 100 counts per bin[2]. Both the effective area file (ARF) and the redistribution matrix (RMF) where computed by weighting each position dependent ARF's and RMF's by the X-ray brightness. We fitted the spectrum in the 0.5-10 keV range with an absorbed Raymond-Smith model (Raymond & Smith, 1977) using *Sherpa*. The source redshift is treated as unknown and, because of the the low statistics, no iron line or other line complex features are expected to be visible.

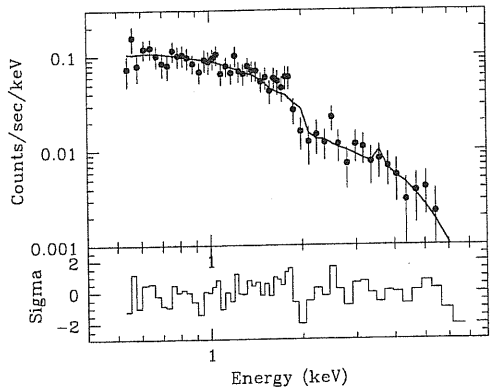

Figure 6.6: *Chandra* ACIS Spectrum and residuals to a Raymond-Smith model with $kT = 10.23$ keV and $z = 0.89$. The spectrum was binned, for display purposes, to obtain a minimum of 30 counts per bin.

In order to get an estimate of the temperature, we fixed the equivalent hydrogen column density to the Galactic value ($N_H = 1.38 \times 10^{20}$ cm^{-2}, Stark et al. 1992), the metal abundance to 0.3 times the Solar value, and we draw confidence levels for the T and z (Fig. 6.7). We find a best fit value of $kT = 10.24$ keV and $z = 0.85$ (χ^2 is 18.68 for 20 d.o.f.)[3]. However, as shown in Fig. 6.7, these values are not well constrained.

After all the data analysis had been performed and when ready to sub-

[2]A smaller binning, e.g. as in Fig. 6.6, leads to similar results

[3]Normalizing the background map using an area of 1WGA 1226.9+3332 observation without sources (7.56% lower background) consistent results are obtained: kT=11.94 keV and z=0.87

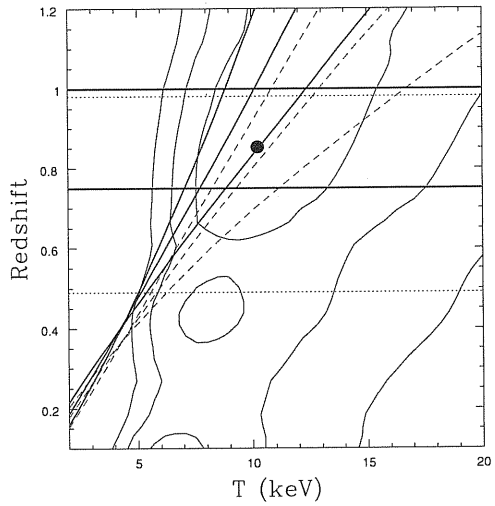

Figure 6.7: The contours of the fit with a Raymond-Smith plasma at 1, 2 and 3 σ. The three blue solid lines represent the luminosity-temperature relation (Markevitch 1998) for $q_0 = 0.5$ and the three blue dashed lines for $q_0 = 0$. The red lines represent the limits on the redshift obtain from the R-K color of the brightest object assuming it is a first ranked elliptical (Coleman, Wu & Weedman 1980), while the dotted lines are the limits from the magnitude of the first ranked elliptical (see text). The big dot corresponds to the best fit to the *Chandra* spectrum.

mit the related paper we found that the same object had been independently identified as a cluster of galaxies in the WARPS survey (Ebeling et al. 2001) and observed for Sunyaev-Zel'dovich effect measurement by Joy et al. (2001). The cluster spectroscopic redshift measured by Ebeling et al. (2001) is $z = 0.89$, which is within the errors of our estimate based on *Chandra* and optical/IR constraints. Fixing the redshift to this value we obtain a temperature of $kT = 10.47^{+4}_{-3}$ keV (kT=12.07 keV using a normalized background), which is in good agreement with that obtained from the Sunyaev-Zel'dovich measurement by Joy et al. (2001) ($kT = 10.0^{+2.0}_{-1.5}$ keV). The absorbed 0.5-2.0 keV flux[4] in a $r = 120''$ aperture is $(3.0 \pm 0.3) \times 10^{-13}$ erg cm^{-2} s^{-1}, consistent with the Ebeling et al. (2001) PSPC measurement; the 0.5-10.0 keV absorbed flux in the same aperture (Table 6.1) is $(8.03^{+0.96}_{-0.88}) \times 10^{-13}$ erg cm^{-2} s^{-1}. For z=0.89 the unabsorbed bolometric and 0.5-2.0 keV band luminosities are $L = (2.2 \pm 0.2) \times 10^{45}$ erg s^{-1} and $L_{X(0.5-2.0)} = (4.4 \pm 0.5) \times 10^{44}$ erg s^{-1} respectively.

[4]The main component in the flux error is the uncertainty on the cluster temperature (quoted in the text); using the $\pm 1\sigma$ values on T we derive an error of +11% −12% on the flux. Other contributions come from the normalization chosen for the background (±9%), from the fraction of counts lost using the $r = 120''$ aperture assuming a β-profile (±5%) and from the Poisson error on the counts (±3%)

Table 6.1: 1WGA J1226.9+3332 observations

Energy	Instrument	Date	Expo. (ks)	Coordinates (J2000)	Offset[a] ($''$)	Count Rate (Counts s^{-1})	
X-ray	*Chandra*	Jul 31 2000	9832.3	12 26 58.2 +33 32 48.28	0.0	0.107 ± 0.006^b	8
R-band	SAO 48in	Feb 02 1997	900	12 26 58.2 +33 32 48.7	0.87	–	
K-band	IRTF	Jan 31 2000	1200	12 26 58 +33 32 48[c]	2.0	–	
Radio	FIRST	–	–	12 26 58.19 +33 32 48.61	0.79	–	3

[a] Offset from *Chandra* position
[b] [0.5-10 keV] in a circle with r=120$''$ computed from the spectral model within sherpa
[c] Due to the lack of bright stars in the K-band image, we obtained an estimate of the position using the objects in common with the R image.

6.2.3 Optical, Infrared and Radio Observations

We combined the *Chandra* information with the optical and IR ones.

A R-band image of the 1WGA 1226.9+3332 field was obtained on Feb. 2, 1997 at the SAO 1.2 m telescope on Mt.Hopkins. A R= 20.4 ± 0.2 galaxy is detected less than 1$''$ from the X-ray centroid (Table 6.1).

A K-band image of the field was obtained using NSFCam at the NASA IRTF on Jan. 31, 2000. The same galaxy is also seen, but is much brighter at K=15.5 (Fig. 4.2) isophotal magnitude. The K-band magnitude within the core radius of the X-ray source is K=15.4, implying that little large scale IR emission sis present. The R-K color of this object is 5.1 with an estimated uncertainty of 0.3 mag due to the poor image quality in both K- and R-band.

Comparing R and K-band images, it is clear that there are many more objects detected in the K- than in the R-band. We detect 23 objects with K<19.5 mag in the $1.5' \times 1.5'$ image using the source extractor software (SExtractor, Bertin & Arnouts 1996) versus only 4 at R. The star/galaxy classification was carried out morphologically using the Kron radius (Bertin & Arnouts 1996), and 3 objects are classified as pointlike. These objects are also detected in the R-band and have bluer colors (R-K<4.2) than the extended objects; we argue they are stars. We should not have to worry about the star contamination of the sample since there are very few stars with K>16 (e.g. Glazebrook et al. 1995). The rest of the morphologically extended objects are galaxies. These, including the bright one located at the X-ray centroid, have very similar red colors (4.5 <R-K< 6.5), implying that they likely have similar redshifts and belong to a cluster. A high-z cluster, CIG J0848+4453, at z=1.27 was detected in a near-IR field survey

using similar color criteria in an over-dense region (Stanford et al 1997). The apparent asymmetry of the galaxy distribution may be an artifact of the longer exposure time at the center of the K-band mosaic image which is offset from the X-ray centroid.

The galaxy surface density in the K-band image is clearly high (Fig. 4.2). We generate K-band galaxy number counts in our field in the range $15 < K < 19.5$, and compare them with those obtained from the near-IR field surveys (Fig. 4.3) in this range (Gardner et al. 1993, Saracco et al. 1997, Huang et al. 1997, Minezaki et al. 1998, Huang et al. 2000) with their coverage ranging from 200 arcmin^2 to 10 deg^2. The number counts obtained from our image are substantially higher ($> 10\sigma$, a factor of 100 at K=19) than those from the field surveys. Such a large excess cannot be due to Poisson statistics or magnitude errors.

Both the high density and the similar (extremely red) colors for these galaxies thus imply that they are likely to be members of a cluster.

The FIRST survey detected a faint 3.61 ± 0.18 mJy source at 1.4 GHz (Becker, White & Helfand, 1995) close to the center of the X-ray emission (See § 3.3 and Table 6.1). The radio source is pointlike (FWHM$\leq 0.91''$, ≤ 16 kpc at $z = 0.85$) and has a luminosity $L_R(z = 0.85) \sim 6.6 \times 10^{24}$ W Hz^{-1}, compatible with low luminosity radio-loud AGNs (e.g. Zirbel & Baum, 1995).

6.2.4 Discussion and Conclusion

Chandra has shown that 1WGA 1226.9+3332 is an extended X-ray source, with a hard, high temperature thermal spectrum. Optical and IR imaging has shown that 1WGA 1226.9+3332 has faint optical/IR counterparts. A cluster of galaxies is the only known type of object that could fit such a description. Moreover the K-band image shows a strong excess of galaxies compared with field counts at K> 17 (Fig. 4.3) around 1WGA 1226.9+3332. Physical clustering is the only possible explanation. Several lines of argument go on to suggest that it is a high redshift cluster of galaxies. Below we list these arguments and try to constrain its temperature and redshift. These results are summarized in Figure 6.7.

(1) The *Chandra* X-ray profile is well fitted by a β model with β=0.77, a value in agreement with a typical relaxed cluster (e.g. Jones & Forman, 1999 and references therein). Moreover, if the cluster redshift is $0.7 < z < 1.2$, then the observed angular core radius, $r_c = (18.1 \pm 0.9)''$ (101 ± 5 kpc at $z = 0.89$ with the assumed cosmology), corresponds to a linear size of $90 < r < 150$ kpc for any value of Ω ($130 < r < 220$ kpc for any value of Ω for H_0=50 km s^{-1} Mpc^{-1}), values consistent with a typical relaxed cluster.

(2) It is well known that clusters of galaxies follow a well-defined Luminosity-Temperature relation (e.g. Markevitch 1998 and reference therein). Recently it has been shown that the local $L_X - T$ relation does not evolve (or is consistent with little evolution) with redshift up to $z \approx 0.8$ (see e.g. Wu et al. 1999; Della Ceca et al 2000; Fairley et al. 2000 and reference therein). Fig. 6.7 shows that the $L_X - T$ relation ($L = AT_6^{\alpha}$ where $T_6 = T/6$ keV, $\alpha = 2.02 \pm 0.40$ and $A = (1.71 \pm 0.21) \times 10^{44}\ h^{-2}$ erg s^{-1}) from Markevitch (1998) requires a 3σ lower limit of $T > 4$ keV and z>0.4, while the 1σ limits require T> 7.5 keV and $z > 0.65$ if no evolution is assumed. The best fit value of 0.85 obtained from *Chandra* spectrum (dot in Figure 6.7) is consistent with the unevolving $L_X - T$ relation.
(3) K-band imaging has shown that 1WGA 1226.9+3332 has a galaxy at K=15.5. If this source is a first ranked cluster elliptical with $M_K = -26.7 \pm 0.5$ (Collins & Mann 1998), then, assuming negligible K-correction, $q_0 = 0.5$ and , H_0=50 km s^{-1} Mpc^{-1} as in Collins & Mann (1998), it has $z = 0.68^{+0.30}_{-0.19}$ (dotted lines in Fig. 6.7).
(4) the color of the K-band galaxies is extremely red, with none bluer than R-K$\sim$ 4.5 and a maximum R-K= 6.5. Only a unevolving elliptical galaxy at 0.7 <z< 1.5 or a Sbc galaxy at z> 1.1 can have such a red color (Coleman, Wu & Weedman, 1980). Using the more accurate R-K$\sim$ 5.1 ± 0.3 of the first ranked elliptical we can restrict the redshift range to $0.75 < z < 1.0$ (red lines in Fig. 6.7).

Using all these constraints we conclude that 1WGA 1226.9+3332 is a distant cluster of galaxies with a most probable redshift of 0.85 ± 0.15 and not smaller than $z = 0.65$.

This gives $kT = 10^{+4}_{-3}$ keV and implies an X-ray luminosity, determined in a $r = 120''$ aperture, of $L_{X(0.5-10keV)} = 1.3^{+0.16}_{-0.14} \times 10^{45}$ erg s^{-1}, corresponding, for $z = 0.85$, to a bolometric $L = (2 \pm 0.2) \times 10^{45}$ erg s^{-1}. Our estimated redshift is similar to the spectroscopic $z = 0.89$ found by Ebeling et al. (2001).

The blank field X-ray source 1WGA 1226.9+3332 is thus a highly luminous and massive high redshift cluster and a useful source to determine the evolution of the clusters X-ray luminosity function (e.g. Rosati et al., 1998). Since models in the direction of low Ω universe (with or without cosmological constant) (e.g. Henry 2000, Borgani & Guzzo 2001) predict a higher density of high redshift clusters compared to high Ω models, finding hot high redshift clusters has a strong leverage on cosmological models.

Chapter 7

Discussion and conclusions

Before discussing the results obtained and their astrophysical implications I will summarize all the available information on the blank field sources.

From *ROSAT* observations we know that blank field sources:
– are, by definition, bright in X-ray and faint in optical;
– have on average harder spectra than radio-quiet quasars (see § 3.1);
– are persistent sources, at least for the 10 of them for which multiple observations exist;
– are not strongly variable within each *ROSAT* observations (3-27 ks long) and on timescales of few years when multiple observations exist.

From the optical and IR imaging and from the radio surveys we learned that:
– **I remembered 5...but I do not have the K band magnitudes yet... all of them are in the stolen books!** have a red counterpart **I do not know how red because all the K band magnitudes are in the stolen books** in the X-ray error circle.
– 3 sources (1WGA J0221.1+1958, 1WGA J1226.9+3332 and 1WGA J0432.4+1723) show a strong excess of K-band counts compared to the field counts.
– the two sources for which we have both radio and optical fluxes (i.e. the high z cluster 1WGA J1226.9+3332 and the BL Lac 1WGA J1340.1+2743) are radio-loud with $f_{(1.4\mathrm{GHz})}/f_V \sim 1000$.

All the blank field sources were unidentified when first selected. The identification process, performed by us and independently by other groups, showed that:
– 2 blank field sources among the 3 showing K-band counts excess are high luminosity and high redshift clusters of galaxies: 1WGA J1226.9+3332 at

Table 7.1: The radio counterparts to the blank field sources.

Source name (1WGA J)	Identification	z range	R	E[a]	B	O[a]	K	O-E[b]	R-K
1340.1+2743	BL Lac		21.3	-	-	-	?	-	
0221.1+1958	Cluster	0.45	19.7	-	-	-	15.1	-	4.6
1226.9+3332	Cluster	0.89	20.4	-	-	-	15.4	-	5.0
0432.4+1723	Cluster?	$\sim 0.5 - 1.0$	20.1[c]	20.0	-	-	15.3[c]	> 1.5	4.8
1103.5+2459	Cluster?	~ 1	~ 22	18.2	-	-	16.2	> 3.3	5.8
1220.3+0641	AGN?		17.6	18.58	-	21.81	13.6	3.23	4.0
1416.2+1136	AGN?		19.5	19.5	20.7**	22.22	?	2.72	
1535.0+2336	AGN?		19.9	19.6	-	21.8	?	2.2	
0951.4+3916	AGN?		20.1	19.1	-	-	16.0	> 2.4	4.0
1412.3+4355	AGN	0.59	19.9	18.73	20.7	-	?	> 2.77	
1415.2+4403	AGN	0.56	20.7	-	-	-	?	-	
1420.0+0625	Unknown		20.0	-	-	-	?	-	
1243.6+3204	Unknown		20.8	-	-	-	?	-	
1220.6+3347	Unknown		?	?	-	21.7	?	?	
1216.9+3743	Unknown		~ 22	-	-	-	?		?
1233.3+6910	Unknown		~ 22	-	-	-	?	-	

[a] Palomar data
[b] when only the O or E magnitude is available we computed lower/upper limits on O-E assuming O=21.5 and E=19.5 as Palomar limits
[c] dereddened for Galactic absorption
? K magnitude was written in the stolen notebooks

z=0.89 and 1WGA J0221.1+1958 at z=0.45;
– 1WGA J0432.4+1723 is a strong high redshift and luminous cluster of galaxies candidate. Its redshift should be in the range $0.5 < z < 1.1$;
– 1WGA J1103.5+2459 is another cluster of galaxies candidate;
– 1WGA J1340.1+2743 is a BL Lacertae object;
– 2 sources (1WGA 1412.3+4355 and 1WGA 1415.2+4403) are apparently normal type 1 AGN at $z \sim 0.5$.

We expected blank field sources to be BL Lacertae objects, old isolated neutron stars, peculiar AGNs, unusual clusters of galaxies or extremely variable sources (see § 2.1) and we found so far BL Lacs, peculiar AGNs and high redshift clusters of galaxies. We will review each of these and discuss them in the following subsections; while a schematic summary of the identified sources and a possible classification for the still unidentified sources is presented in Table 7.1.

7.1 BL Lacertae objects

BL Lacertae objects can reach $f_X/f_V \sim 35$ and are thus expected to "contaminate" our sample at the least extreme side. We found one BL Lacertae object, 1WGA J1340.1+2743, among our blank field sources, but it was extremely X-ray loud $f_X/f_V \sim 300$. During a *Chandra* observation we obtained the source was ~ 10 fainter than in *ROSAT* detection, thus explaining the extreme X-ray loudness with the *ROSAT* observation monitoring the source during a very high state. 1WGA J1340.1+2743 can be an extreme BL Lac as the ones studied by Costamante et al. (2001).

7.2 Isolated neutron stars

The spectrum expected from IONSs is thermal and soft (for a review on IONS see Treves et al. (2000) and references therein), with typical temperatures $T \sim 100$ eV (but models with harder spectra have also been proposed, e.g. Zampieri et al. 1995). The flatter than average spectra of blank field sources suggests that statistically it is unlike that blank field sources are IONSs, but since the PSPC spectra we derived cannot discriminate between an absorbed power-law, a black body or a Raymond-Smith model, the existence of one or more IONSs among the selected sources cannot be ruled out.

7.3 Peculiar AGNs

When we started this project we expected to find examples of peculiar AGNs such as absorbed ones (QSO-2s or LMSy2s) or ADAF (§ 2.1). Indeed two sources, 1WGA J1412.3+4355 and 1WGA J1415.2+4403 were spectroscopically identified in the RIXOS survey (Mason et al. 2000) as AGNs and their are both peculiar AGNs, especially 1WGA J1412.3+4355, which is the most extreme source in our sample of blank field sources. Other 4 sources (1WGA J1220.3+0641, 1WGA J1416.2+1136, 1WGA J1535.0+2336 and 1WGA J0951.4+3916, see Table 7.1) are likely to be AGNs. 1WGA J0951.4+3916 stands out of the group because it shows signs of absorption in the X-ray band ($N_H \sim 2^{+3}_{-1} \times 10^{21}$ cm^{-2}, Table 3.3); it also has a red source in the Palomar E-band (E=19.1) and it is likely to be an absorbed AGN.

The remaining 5 sources are peculiar and seem to share the same characteristics: they have X-ray spectra typical of type 1 AGNs ($\Gamma \sim 2$ and absorbing column densities consistent with the Galactic values) and they have a red (O-E> 2) counterpart in the Palomar E-band at $E < 19.5$ (Ta-

ble 7.1) (with the exception of 1WGA J1415.2+4403). For a local AGN type 1, $O - E > 2$ implies $A_V > 4$ (e.g Risaliti et al. 2001) and thus strong obscuration ($N_H > 2 \times 10^{21}$ cm^{-2} when the dust to gas ratio typical of the ISM in our Galaxy, A_V(mag) $\sim 5 \times 10^{-22} N_H$ cm^{-2}, is assumed), in contrast to the results of the X-ray data.

write about R-K when K magnitude is computed!!!!

We proposed some possibilities to reconcile X-ray and Palomar data in the section dedicated to each source (§ 5.2) and they are: high redshift, high dust to gas ratio, shifted or absent BBB emission and extreme long term variability. We will review and discuss each of these possibilities in the following subsections.

7.3.1 High redshift

As clear from Figure 7.1 taken from Risaliti et al. 2001, at $z \geq 3.5$ the O-E color is larger than 2 even for absorbing columns consistent to the Galactic value.

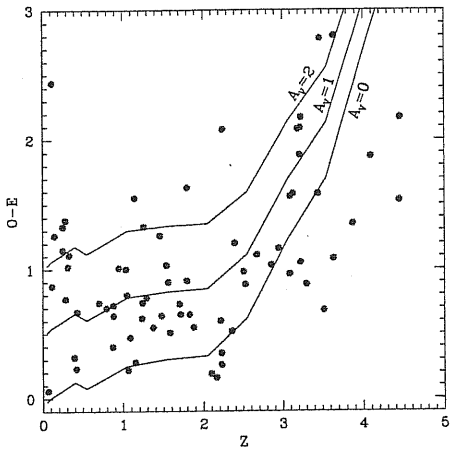

Figure 7.1: (From Risaliti et al. 2001) Optical O-E color versus redshift for the HS sample of Risaliti et al. (2001). Lines are for a standard quasar spectrum of Francis et al. (1991) with three different rest frame optical extinctions: $A_V = 0$ (bottom line), $A_V = 1$ (middle line), $A_V = 2$ (top line).

If we assume $z \geq 3.5$ for our AGN-like sources, there is no need for extra than Galactic absorption. The luminosity of the AGN-like sources if they were at $z \sim 4$ would be $\leq 10^{47}$ erg s^{-1}, consistent with a QSO. **what about the expected and measured R-K???**

We note that, even if promising, this option is excluded for the 2 sources spectroscopically identified in the RIXOS (1WGA J1412.3+4355 and 1WGA 1415.2+4403) which have $z \sim 0.5 - 0.6$.

7.3.2 High dust to gas ratio

Another way to reconcile the lack of absorption in the X-rays (mainly due to neutral hydrogen) with the obscuration in the optical band (due to dust) suggested by the red Palomar counterparts, is to assume an higher than Galactic dust to gas ratio.

We computed the A_V for the 4 sources with a counterpart in the Palomar E band using Figure 7.1 at local redshift except for the two RIXOS AGNs with known redshift. We then derived the A_V/N_H (blue region in Figure 7.2) using the Galactic N_H for each source (Stark et al. 1992) and compared it to the extrapolation of the expected variation of the A_V/N_H ratio as a function of the dust-to-gas ratio presented in Maiolino et al. (2001) relation (Figure 7.2).

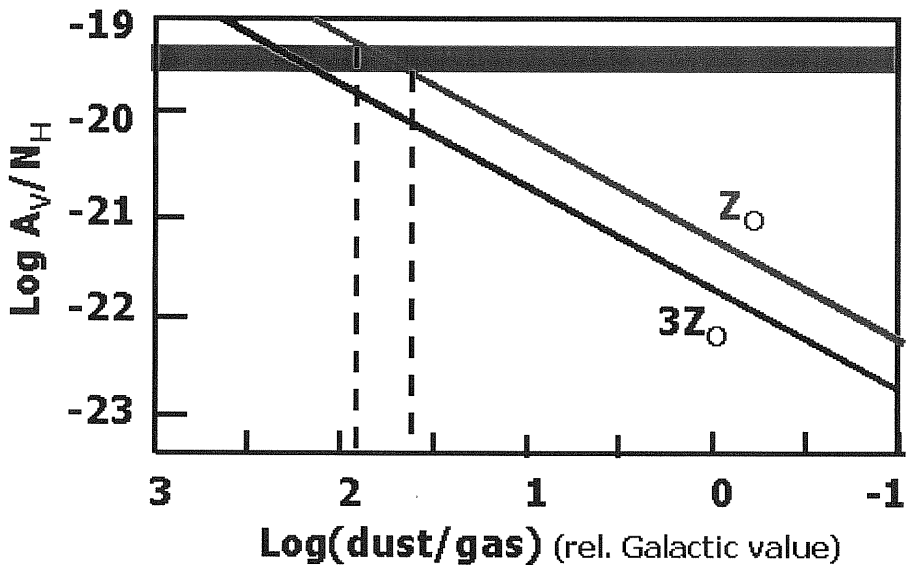

Figure 7.2: The red line represents the expected variation of the A_V/N_H ratio as a function of the dust-to-gas ratio relative to the Galactic value. The predictions of the models, which assume a standard dust size distribution, are shown by the thick solid lines. The blue line marks the AGN-like blank field sources The dashed vertical lines indicate the range of gas-to-dust ratios that matches the observed A_V/N_H computed assuming Galactic N_H and A_V necessary to reproduce the Palomar colors (Figure 7.1). The black line indicates the effect of an increased dust-to-gas ratio due to a metallicity three times solar.

We derive dust to gas ratio $\sim 40 - 60$ times the Galactic value when Solar metallicity is assumed (Figure 7.2). The most recent observational evidence shows the tendency of AGNs to have lower than Galactic dust to gas ratios (e.g. Risaliti et al. 2001; Maiolino et al. 2001) and such an higer than Galactic dust to gas ratio is physically difficult to justify. We

note that Maiolino et al. (2001) find an higher than Galactic dust to gas ratio for low luminosity objects ($L_X \sim 10^{41}$ erg s^{-1}) and suggest that these objects may be intrinsecally physically different from the "classical" AGNs, an hypothesis we develop in the next subsection.

7.3.3 Missing or shifted BBB

Galaxies with bright X-ray emission ($L_X \sim 10^{42} - 10^{43}$ erg s^{-1}) but weak or absent AGN features in the optical band have been known to exist since *Einstein* observations (Elvis et al. 1981; Tananbaum et al. 1997) and are now being found in larger number (e.g. Della Ceca et al. 2001; Hornschemeier et al. 2001, Fiore et al. 2001). A way to explain the faintness of the optical counterpart for these sources and for the 5 AGNs/AGN-like 'blanks' is to assume that the source is intrinsically optically faint.

The first way to justify this is that the BBB emission is highly suppressed: this is exactly what happens in ADAFs (Narayan & Yi, 1994; § 2.1 and red line in Figure 2.3) where the energy usually released by thin disks models (blue line in Figure 2.3) in the optical-EUV range (the BBB) is advected toward the center before being able to escape.
To check if an ADAF can have the extreme properties we observe in our blank field sources we derived the V magnitude and the α_{ro} and α_{ox} from Figure 2.3, which is the spectral fit to Sgr A* (Narayan et al. 1998). Assuming a distance of $\sim$ 10 kpc we get $f_{(1.4\mathrm{GHz})} = 580$ mJy, V=17.22 and $f_{(1\mathrm{keV})} = 7.75 \times 10^{-4}$ photons cm^{-2} s^{-1} keV^{-1}, while the 0.3-3.5 keV flux is $\sim 10^{-11}$ erg cm^{-2} s^{-1} ($L_{(0.8-2.5\mathrm{keV})} = 1.55 \times 10^{34}$ erg s^{-1} Narayan et al. 1998). Using these values we derive $\alpha_{ro} \sim 0.61$ and $\alpha_{ox} \sim 1.12$ and $f_X/f_V \sim 18$, which are compatible with blank field sources. We note that these values are indicative and could be more extreme just slightly changing the parameters of the ADAF model (e.g. Di Matteo & Allen 2000).

Another case in which the BBB emission appears suppressed is when it is shifted out of the optical band. Since the thin disk temperature is inversely proportional to the mass of the central object, low mass AGNs (e.g Narrow Line Sy) are expected to have the BBB shifted toward higher energies. Such a high energy BBB has been already observed and an example is the NLSy RE J1034+396 (Puchnarewicz et al. 1998; 2001). We computed an $f_X/f_V \sim 11$ for RE J1034+396 using the WGACAT2000 flux ($F_{X(0.05-2.5\mathrm{keV})} = 2.71 \times 10^{-11}$ erg cm^{-2} s^{-1}) and V=15.6. In the radio band RE J1034+396 has $f_{(1.4\mathrm{GHz})} = 23.5 - 26.0$ mJy, which together with the normalization at 1 keV (1.05×10^{-3} photons cm^{-2} s^{-1} keV^{-1}) we obtained in the spectral

fit of *Beppo-SAX* data (Puchnarewicz et al. 2001), gives $\alpha_{ro} \sim 0.22$ and $\alpha_{ox} \sim 1.18$, compatible with the least extreme blank field sources. It is difficult to explain the blank field sources with extreme values of f_X/f_V as NLSy galaxies. NLSy are in fact ususally strongly variable even on minutes time scales (RE J1034+396 is an exception) while the 'blanks' seem not to vary during the *ROSAT* observations; if the most extreme blank field sources were "nonvariable" NLSy, like RE J1034+396, an higher f_X/f_V would imply higher disk emission (X-ray emission in NLSy is thought to be disk emission, e.g. Puchnarewicz et al. 2001) and thus higher accretion rates. Since NLSy are thought to have higher accretion rates than "normal" Seyfert galaxies, an even more extreme scenario would be a surprising finding.

7.3.4 Extremely variable AGNs

None of the sources seems to be extremely variable within each PSPC observation, but we cannot a-priori exclude a high state during the *ROSAT* observations (as happened for the BL Lac 1WGA J1340.1+2743).

7.4 High redshift clusters of galaxies

Two high luminosity (unabsorbed luminosity $L_{X(0.5-2.0)} = 1.28 \times 10^{44}$ erg s^{-1} for 1WGA J0221.1+1958, Romer et al. 2000; and $L_{X(0.5-2.0)} = (4.4 \pm 0.5) \times 10^{44}$ erg s^{-1} for 1WGA J1226.9+3332, Cagnoni et al. 2001, using H_0=75 km s^{-1} Mpc^{-1} and $q_0 = 0.5$) and high redshift clusters of galaxies and two more candidates were found among a total of 16 source. High luminosity and high redshift clusters of galaxies are rare and their number density is crucial for cosmological studies. Finding high luminosity and high redshift clusters of galaxies is the only way to:
- determine if any evolution is present in the luminous tail of the cluster X-ray luminosity function;
- constrain the amount of evolution of the luminosity-temperature relation;
and both issues are related to the density of the Universe.
Even if the two clusters found in the course of this thesis are not enough to discern among different models, other clusters can be hidden among our blank field sources. In the next paragraphs we detail about the present understanding of the topics on which high luminosity and high z clusters of galaxies are crucial and of their cosmological and astrophysical consequences, without the presumption of being able to solve this questions with two objects only, but with the aim of showing why these rare objects are important in cosmology and why it is worth to present our method which proved to be the best for finding them.

7.4.1 Cluster X-ray luminosity function

While everybody agrees on the cluster X-ray Luminosity Function (XLF) for clusters with $z < 0.3$ and $L_{(0.5-2)} < 3 \times 10^{44}$ erg s^{-1}, there is not yet consensus for the XLF of the brightest and most distant clusters known. Measurements of the distant XLF at $L_{(0.5-2)} > 5 \times 10^{44}$ erg s^{-1} are difficult with the current samples due to low number statistics. As a result, the evolution of the XLF has remained a hotly debated issue, ever since it was first reported in the *Einstein* Medium Sensitivity Survey (EMSS, Gioia et al. 1990; Henry et al. 1992). Using a complete sub-sample of 67 clusters at $0.14 < z < 0.6$, the authors found a statistically significant negative evolution of the XLF at $z > 0.3$ and $L_{(0.5-2)} > 5 \times 10^{44}$ erg s^{-1}. Covering a very large solid angle (735 deg^2), but being relatively shallow, the EMSS sample can probe mostly the bright end of the XLF and can provide weak constraints on the evolution of the XLF at higher redshifts since only six EMSS clusters lie at $z > 0.5$. Many other clusters surveys based on *ROSAT* data have been undertaken but they do not agree on the evolution of the brightest end of the XLF: while the RDCS (Rosati et al. 1995; 1998; 2000), the NEP (Gioia et al. 2000 and references therein), the SHARC (Nichol et al. 1999) and the CfA 160 deg^2 survey (Vikhlinin et al. 1998; 2000) confirm the EMSS results, the MACS (Ebeling et al. 2000) and the WARPS (Jones et al. 2000) do not find evidence for evolution up to $z = 0.4$ and $z = 0.83$ respectively.

7.4.2 Cluster luminosity-temperature relation

The analyses of nearby clusters showed the existence of a relation between the luminosity and the temperature of a cluster of galaxies. All the studies agree on a relation of the form:

$$L_X = L_6 \left(\frac{T_X}{6keV}\right)^{\alpha} (1+z)^A \left(\frac{d_L(z)}{d_{L,EdS}(z)}\right)^2 \times 10^{44} h^{-2} \text{ erg s}^{-1}$$

where L_6 is a dimensionless quantity and $d_L(z)$ is the luminosity distance at redshift z for a given cosmology and $d_{L,EdS}(z)$ is the same for an Einstein-de Sitter model. Nearby clusters with $T \geq 1$ keV have $L_6 \sim 3$ and $\alpha = 2.5 - 3$ (e.g. White, Jones & Forman, 1997; Markevitch 1998; Allen & Fabian 1998; Arnaud & Evrard 1999; Wu, Xue & Fang 1999 and references therein) with a scatter $\leq 30\%$; while for cooler groups the relation steepens to $\alpha \sim 5$ (e.g. Helsdon & Ponman 2000).

A sample of high z clusters of galaxies with a measure of their temperature is the only means to determine if any evolution is present in this relation.

Figure 7.3 (from Borgani et al. 2001) shows the $L_X - T_X$ relation both for low and high redshift clusters of galaxies and constrains the evolution of the $L_X - T_X$ relation over the largest redshift interval probed to date. This figure includes (large squares) a compilation of distant ($0.57 \leq z \leq 1.27$) clusters recently observed with *Chandra* (Stanford et al. 2001; Holsen et al. 2001; Giacconi et al. 2001; Jeltema et al. 2001) among which is the z=0.89 cluster 1WGA 1226.9+3332 discovered in this thesis project. There are only 11 clusters at $z > 0.5$ with a measure of their temperature (e.g. Della Ceca et al. 2000; Borgani et al. 2001 and references therein), and they always lie below or on top of the local relation, with the possible exception of the cluster at $z = 1.27$, whose X-ray spatial distribution suggests that this might not be a relaxed system. These data show that the evolution in the luminosity-temperature relation is absent or mild, corresponding to $A < 1$.

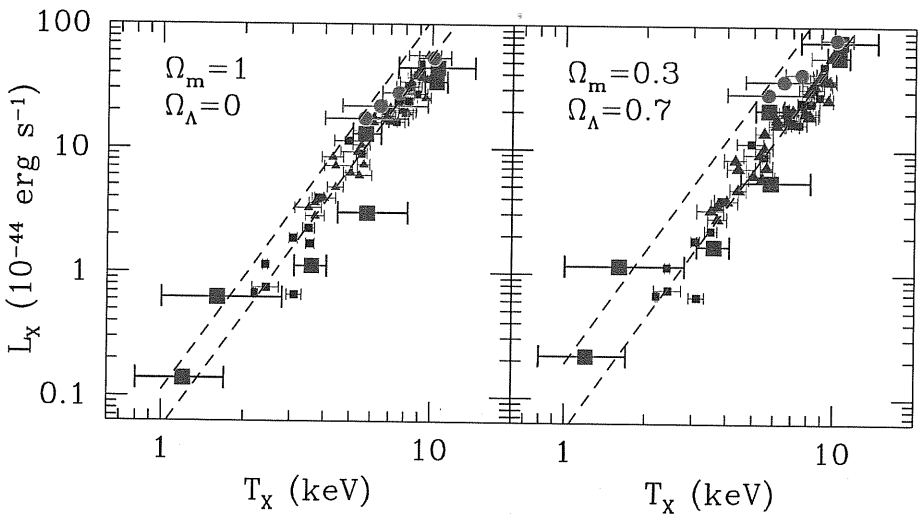

Figure 7.3: (from Borgani et al. 2001) The luminosity–temperature relation for nearby and distant clusters in two different cosmologies. Values of L_X assume here $h = 0.5$ for the Hubble parameter. The nearby clusters analyzed by Markevitch (1998) and by Arnaud & Evrard (1999) are indicated with small triangles and squares, respectively. Large circles are for the compilation of clusters at $0.5 \leq z \leq 0.8$ reported by Della Ceca et al. (2000). The large squares are for the compilation of distant ($0.57 \leq z \leq 1.27$) clusters recently observed with Chandra. The dashed lines indicate the L_{bol}–T_X relation (see text) with $L_6 = 3$ and $\alpha = 3$, for $A = 0$ (lower lines) and $A = 1$ computed at $z = 1$ (upper lines).

The luminosity-temperature relation is important on its own because it is the result of the thermodynamical history of the diffuse X-ray emitting gas in clusters of galaxies and it is determined by gravitational processes associated with infalling gas, shock heating and adiabatic compression, and

non-gravitational processes such as heating by supernovae, stellar winds, activity in central galactic nuclei and radiative cooling (e.g. Tozzi & Norman 2001).

The luminosity-temperature relation is also extremely important because it is used to compare theoretical predictions and observations on the spatial density of clusters of galaxies with the aim of deriving the cosmological parameters; the values of Ω_m derived with this approach depend on the assumed evolution of the luminosity-temperature relation.
According to the standard picture of hierarchical clustering, high redshift clusters of galaxies form from the gravitational collapse of exceptionally high peaks of the primordial density perturbations. Clusters are thus a probe of the high density tail of the distribution of the cosmic density field and their number density is sensitive to the cosmological scenario (e.g. White, Efstathiou & Frenk 1993). The low redshift cluster density has been used to constrain the amplitude of the density perturbation, while the redshift evolution of the cluster abundance reflects the growth rate of density perturbations, and primarily depends on the matter density parameter Ω_m (e.g. Oukbir & Blanchard 1992). While the value of Ω_m strongly rules the mass distribution, the value of Ω_Λ is known to have a smaller effect and is far from being constrained with the present clusters samples.

Theoretical models predict the number density of clusters of a given mass, but the mass itself is never an observed quantity. The usual approach is to convert the theoretical prediction on the cluster mass into X-ray luminosity and compare this to the observations. The mass is converted into luminosity in a two step process: the mass is first converted into temperature of the X-ray emitting intracluster gas assuming spherical symmetry, virialization, isothermality and hydrostatic equilibrium. The second step is to relate the ICM temperature to the X-ray luminosity; this conversion makes use of the luminosity-temperature relation and the knowledge of its evolution is needed from a (not necessarily complete) sample of distant clusters out to $z \sim 1$.

7.4.3 The best method to search for high z and high L clusters of galaxies

Since high luminosity, high redshift clusters should be rare, the relative ease with which we discovered 1WGA J1226.9+3332 is potentially of great significance.

The X-ray band is the best energy range for the selection of clusters samples, especially for high z clusters. The X-ray selection is considered to be superior to the optical detection method because clusters are powerful

X-ray emitters with temperature and gas density which directly reflect the cluster gravitational potential and because X-ray emission depends on the square of the local gas density, while the optical emission depends linearly on the number of galaxies, making clusters stand out more sharply in the X-ray than in the optical. All the X-ray surveys of the last decade, except for the EMSS, have been developed using *ROSAT* data and are divided into two main groups:
– the continuous area surveys (BCS, BCS-E, NEP, RASS-BS, REFLEX, MACS), based on the All-Sky Survey (RASS, Voges et al. 1999). They generally cover $\geq 10,000$ deg^2 and are used to examine large-scale structure in the cluster distribution, but they are limited to the X-ray brightest clusters;
– the serendipitous surveys (e.g. Bright SHARC, CfA 160 deg^2, RDCS, SHARC-S, WARPS), extracted from pointed observations, which can reach much deeper sensitivity ($\sim 10^{-14}$ erg cm^{-2} s^{-1}, two orders of magnitude deeper than the RASS) but cover a much smaller solid angle ($\sim 100 - 200$ deg^2).
The area of the sky covered by the serendipitous clusters surveys is too small to detect a significant fraction of X-ray luminous clusters; the contiguous clusters surveys, on the other hand, are capable of finding these rarest systems, but are too shallow to detect them in large numbers at $z > 0.3$.
The result is that the cosmologically most interesting objects, the massive and distant clusters, are poorly sampled by all existing X-ray cluster surveys.

The search for extremely X-ray loud sources (blank field sources) can sample a large area of the sky and select the few interesting high redshift and high luminosity clusters of galaxies candidates among the $\sim 62,000$ sources sources in the WGACAT95. With this method we were able to select only 16 sources and the two high z and bright clusters of galaxies already found among them make it the most efficient way to select these rare sources: on the contrary the other available methods, based on the X-ray extent or on the X-ray flux limit, are far less efficient in finding these rare sources and are much better suited in finding faint high z or nearby clusters of galaxies.

7.5 Extremely variable sources

We can exclude a Gamma Ray Burst nature for the 10 blank field sources with multiple observations because they are persistent. For the 6 sources without multiple observations, this option is still open. Within each PSPC observation none of the 16 blanks looks variable indicating that they are not extremely variable sources, at least on the sampled time scales ranging

from 3 ks to few years. We recall that one of the blank field sources, the BL Lacertae object 1WGA J1340.1+2743, while not showing variability within the PSPC observation, was found to be a factor of 10 fainter in a *Chandra* observation: we cannot exclude a long time scale variability for the 6 blank field sources without multiple observations.

7.6 Unknown origin

Some sources are still mysterious (§ 5.3: 1WGA J1420.0+0625, 1WGA J1243.6+3204, 1WGA J1220.6+3347, 1WGA J1216.9+3743 and 1WGA J1233.3+6910.
We review all the available information for each of them.

- **1WGA J1243.6+3204 and 1WGA J1216.9+3743**
  both sources show absorption in excess of the Galactic value and extremely steep power law spectra ($\Gamma = 5.97^{+6.66}_{-2.59}$ and $4.90^{+5.10}_{-1.74}$ see Table 3.3) and they both lie close to a nearby galaxy (Figure 4.2) **write about colors of the counterparts when K available.** The R and K band counterparts for these sources are not particularly red (Figure 4.2 **check this and write R-K!!**), thus excluding a high z cluster of galaxies or an absorbed AGN nature.
  1WGA J1243.6+3204 was observed with the *ROSAT* HRI and we can exclude an extended nature for this source (high z cluster or failed cluster) and since it is not variable within the PSPC and the HRI observations we can also exclude a Gamma ray burst nature or an extreme variable source on a $\sim$ 2-year time scale.
  1WGA J1216.9+3743 was not detected by the HRI, as expected from its PSPC count rate.
  We speculate that these sources could be X-ray binaries in the nearby galaxies: 1WGA J1243.6+3204 could be an X-ray binary within NGC 4656 and, if this is the case, it would be radiating above the Eddington limit for $1M_{\odot}$ star. 1WGA J1216.9+3743 could be an X-ray binary within NGC 4244 (z=0.000815) and its 0.5 – 2.0 keV luminosity would be $\sim 1.5 \times 10^{38}$ erg s^{-1}, again at the borderline with an X-ray binary luminosity.

- **1WGA J1420.0+0625, 1WGA J1220.6+3347 and 1WGA J1233.3+6910**
  these source have similar X-ray spectral shape ($\Gamma \sim 2.2 - 2.4$) and absorption consistent with the Galactic value when fitted with an absorbed power law model (Table 3.3). They do not have red counterparts in their error circles **check this with R-K!! Maybe 1WGA J1420.0+0625 is a bit red**, thus making an high z cluster or an obscured AGN na-

ture unlikely.
For all these source we have multiple observations: in particular 1WGA J1420.0+0625, observed twice by *ROSAT*, is a persistent source and does not look variable within each observation and on a 6-month timescale; 1WGA J1220.6+3347 was detected by *Einstein* $\sim$ 10 years before (Thompson et al. 1998); 1WGA J1233.3+6910 has a detection on the border of the HRI detector 5 years after the PSPC one. All these sources are thus persistent and we can exclude a bursting nature for all of them.

7.7 Summary

We called blank field sources the *ROSAT* bright X-ray sources with faint optical counterparts, with $O > 21.5$ on the Palomar Sky survey. The extreme X-ray over optical flux ratio of blank field sources is not compatible with the main classes of X-ray emitters except for BL Lacertae objects for $f_X/f_V \leq 35$. The identification process brought to the discovery of two high z and high luminosity clusters of galaxies (§ 7.4), one BL Lacertae object (§ 6.1), and two spectroscopically normal, but peculiar AGNs (§ 7.3). Among blank field sources we note the presence of 5 AGN-like sources (§ 7.3) which seems to form a well defined group: they present type 1 X-ray spectra and red Palomar **and R-K???** counterparts. These sources are similar to the galaxies with bright X-ray emission ($L_X \sim 10^{42} - 10^{43}$ erg s^{-1}) but weak or absent AGN features in the optical band found since *Einstein* observations (Elvis et al. 1981; Tananbaum et al. 1997) and which are now being found in larger number (e.g. Della Ceca et al. 2001; Hornschemeier et al. 2001, Fiore et al. 2001). Their nature is till mysterious, and we discussed possible explanations to this discrepancy between X-ray and optical data, among which a suppressed BBB emission (ADAF or shifted BBB as in RE J1034+396), an extreme ($\sim 40 - 60$ the Galactic ratio value) dust to gas ratio and an high redshift ($z \geq 3.5$) QSO nature. Other sources (§ 7.6) have a still unknown nature; for each of them we listed and justified the excluded possibilities.

7.8 Future work

Besides the identification of the remaining sources, the obvious development of this project is to construct a larger and statistically complete sample of blank field sources to assess the abundance of the different

classes of sources in the X-ray sky.

The only X-ray satellite with a large enough database to cover a large solid angle and with good enough positions to allow an optical and/or spectroscopic follow-up is at present *ROSAT*. We constructed a sample using the WGACAT based on PSPC observations, but in the course of this thesis catalogs based on *ROSAT* HRI became available. The smaller error box when compared to PSPC positions will greatly reduce the probability of chance coincidences in the optical band, thus enlarging the sample of blank field sources and would ease the identification process in deep optical-IR images. Even though the HRI has no spectral capabilities, its tighter PSF will immediately provide extent informations for each source, allowing a prompt selection of clusters. From preliminary estimates the number of HRI blank field sources is large enough to construct a sizeable sample and members of our team are now starting to work on this project.

Part II

The BLEIS project

Chapter 8

Blazar Surveys

In this second part of the thesis we present a second survey aimed to select rare sources, blazars in this case. We start this part of the thesis with a brief introduction on blazars an on the current status of the selected samples and the knowledge and problems related to these extreme AGNs (§ 8). In the following chapters we present our survey (§ 9) and the comparison of the pilot sample we selected with theoretical models (§ 10).

Blazars are the most extreme variety of AGNs. Their observed properties include irregular rapid variability, high optical polarization, apparent superluminal motion, flat radio spectra ($\alpha_r < 0.5$), core-dominant radio morphology and broad continuum extending from the radio through the gamma-rays (e.g. Urry & Padovani 1995). The broad-band emission of blazar is dominated by non-thermal processes (synchrotron and the dominant inverse Compton), probably emitted by a relativistic jet pointing in our direction. This radiation is relativistically beamed and thus amplified and collimated in the observer's frame. The definition of the blazar class has changed since its introduction at the 1978 Pittsburgh Conference. In the beginning blazar meant objects dominated by a highly polarized, variable and non-thermal continuum. In the years a number of names (e.g. OVV = optically violent variable, HPQ = highly polarized quasars) has been applied to blazars depending on the dominance of one characteristic and on the method employed for their selection. A more commonly used sub-classification depends on the existence of spectral features in the optical spectrum: FSRQ are blazars with optical spectra dominated by emission lines, while BL Lacertae objects (BL Lacs) are almost lineless objects (for a method

to separate between FSRQ and BL Lacs see Marchã et al. 1996).

Blazars, in agreement with the idea that they are AGNs seen at very small angles of beamed jet to the line of sight, are very rare and make up less than 5% of all AGNs (Padovani 1997; 2001). As a consequence, all blazars samples were, until recently, small and with high flux cuts. These "classical" samples were studying only the brightest blazars and were not large and deep enough to test unification models. Because of this, many deeper blazar surveys have recently been undertaken.

8.1 The "classical" blazar samples

Before discussing these on-going surveys, I will summarize the "classical" ones and their main results.

BL Lacs

- 1 Jy: radio flux limited ($F_{5GHz} > 1$ Jy) with a radio spectral index cut ($\alpha_r < 0.5$), $V < 20$. The complete sample consists of 34 objects (Stickel et al. 1991);
- EMSS (*Einstein* Medium Sensitivity Survey: X-ray flux limited ($F_{0.3-3.5keV} \geq 2 \times 10^{-13}$ erg cm^{-2} s^{-1}). The complete sample includes 41 objects (Stocke et al. 1991; Rector et al. 2000);
- IPC slew: X-ray flux limited ($F_{0.3-3.5keV} \geq 2\times10^{-12}$ erg cm^{-2} s^{-1}). The complete sample includes 51 objects (Perlman et al. 1996).

FSRQ

- 2 Jy: radio flux limited ($F_{2.7GHz} > 2$ Jy). The complete sample consists of 52 objects (Wall & Peacock 1985; Di Serego Alighieri et al. 1994).
- EMSS: X-ray flux limited ($F_{0.3-3.5keV} \geq 2\times10^{-13}$ erg cm^{-2} s^{-1}). The complete sample includes 20 objects (Wolter & Celotti 2001)

These classical surveys were sampling only the brightest radio and X-ray objects and this brought to a bimodality of BL Lacertae characteristics and to a further subdivision. The BL Lacs were thus separated into: radio selected BL Lacs, or RBLs, and X-ray selected BL Lacs, or XBLs. Typically XBLs are less variable and less polarized than RBLs. The spectral energy distribution (SED) of the two classes is strongly bimodal, and, as a consequence, they populate different regions of the

$\alpha_{ro} - \alpha_{ox}$ plane. One of the main issues regarding BL Lacs is their evolution: while the XBL show negative evolution in the X-ray band (e.g. Wolter et al. 1994), the radio selected ones are consistent with no evolution in the radio band (e.g. Stickel et al. 1991). The existence of two distinct populations has tentatively been explained as a difference in the width of the jets of the radio and X-ray radiation (e.g. Ghisellini & Maraschi 1989; Celotti et al. 1993): according to this scenario XBLs are less beamed, and thus seen at larger angles, than RBLs. The main difficulty of these models is to reproduce the position of the peaks in the spectral energy distribution (SED) of RBL by just changing the angle of view of an XBL spectrum. Giommi & Padovani (1994) suggested the existence of an unique class of BL Lacs with a continuous range of spectral properties, with the dichotomy between RBL and XBLs being just the consequence of the fact that the radio and X-ray surveys were sampling the extremes of this continuous sequence. They suggest the terminology of low-energy peaked BL Lacs, or LBLs ($\sim$ RBLs), and high-energy peaked BL Lacs , or HBLs ($\sim$ XBLs) according to the position on the $\nu - F\nu$ diagram of the synchrotron peak (where ν is the frequency and F is the flux density at frequency ν). According to this scenario, intermediate objects were missed in these "classical" surveys. Recently Fossati et al. (1998) further investigated this idea proposed by Giommi & Padovani (1994) suggesting that the bolometric luminosity is the physical parameter that determines the synchrotron peak position. Even if quasars do not present the same duality seen in BL Lacs, the X-ray and radio selected samples of quasars still have some disagreements: for example the X-ray selected quasars are more numerous than predicted from radio samples (e.g. Wolter & Celotti 2001 number counts compared to Urry & Padovani 1992 predictions).

8.2 New blazar samples

With the aim of better understanding this duality seen in BL Lacs many groups started to construct new and larger blazar samples with deeper flux cuts. Most of the recent surveys take advantage of the fact that blazars are both radio and X-ray emitters and, unlike the classical samples, use a double radio/X-ray selection to limit the number of blazars candidates. For the final identification, all of them (except for the Sedentary survey, see below) rely on spectroscopic follow-up for the candidates classification. Unlike the classical surveys which

used a simplified method based on the presence of emission lines, the new blazars surveys separate BL Lacs and quasars using the method presented in Marchã et al. (1996).

BL Lacs

- DXRBS (Deep X-ray Radio Blazar Survey): is radio ($F_{5GHZ} \geq$ 50 mJy) and X-ray limited ($F_{0.1-2.4keV} \geq 2\times10^{-14}$ erg cm^{-2} s^{-1}) with a cut in the radio spectral index ($\alpha_r \leq 0.7$). The complete sample contains 37 BL Lacs and the survey is $\sim$ 90% identified (Perlman et al. 1998; Landt et al. 2001);
- REX (Radio-Emitting X-ray): is radio ($F_{1.4GHZ} \geq 5$ mJy) and X-ray limited ($F_{0.1-2.4keV} \geq 3 \times 10^{-14}$ erg cm^{-2} s^{-1}). The sample contains 72 BL Lacs and the survey is $\sim$30% identified; in a complete sub-sample (90% identified) there are $\sim$ 40 BL Lacs ($F_{0.1-2.4keV} \geq 4\times10^{-13}$ erg cm^{-2} s^{-1}) (Caccianiga et al. 1999;2000;2001);
- RGB (RASS=ROSAT All Sky Survey/ Green Bank): is radio ($F_{5GHZ} \geq$ 20 mJy), X-ray ($F_{0.1-2.4keV} \geq 3 \times 10^{-13}$ erg cm^{-2} s^{-1}) and optically limited ($B < 18$). They found 127 BL Lacs and the complete sample consists of 33 objects. The RGB is 94% identified (Laurent-Muehleisen et al. 1998; 1999);
- "Sedentary" Survey: is radio ($F_{1.4GHZ} \geq 3.5$ mJy) and X-ray limited ($F_{0.1-2.4keV} \geq 10^{-12}$ erg cm^{-2} s^{-1}) with two broad band spectral cuts, one on the radio to X-ray spectrum ($\alpha_{rx} \leq 0.56$) and one on the radio to optical spectrum ($\alpha_{ro} > 0.2$). These spectral cuts are imposed to select a region populated by high-energy peaked BL Lacs (HBL) only. The main difference with the other surveys is that all the objects which satisfy these selection criteria (218 total; 155 complete) are included in the HBL sample without any further spectroscopic follow-up (Giommi, Menna & Padovani 1999; Giommi et al. 2001);
- FIRST flat spectrum sample: is radio ($F_{1.4GHZ} \geq 35$ mJy and $F_{5GHz} > 20$ mJy) and optically limited ($B < 19$) with a cut in the radio spectral index ($\alpha_r < 0.5$). The sample includes 87 objects and the survey is $\sim$ 84% identified (Laurent-Meuhleisen et al. in preparation)

FSRQ

- Parkes 0.25 Jy sample: is radio selected (PKS, flux limit $F_{2.7GHz} =$ 250 mJy) with a cut in the radio spectral index ($\alpha_r \leq 0.4$). The

sample is completely identified and consists of 444 sources (Shaver et al. 1996; Hook et al. 1999; Jackson & Wall 2001);

- DXRBS (Deep X-ray Radio Blazar Survey): is radio ($F_{5GHZ} \geq$ 50 mJy) and X-ray limited ($F_{0.1-2.4keV} \geq 2\times10^{-14}$ erg cm^{-2} s^{-1}) with a cut in the radio spectral index ($\alpha_r \leq 0.7$). The complete sample contains 187 objects and is $\sim$ 90% identified (Perlman et al. 1998; Landt et al. 2001);
- FIRST flat spectrum sample: is radio ($F_{1.4GHZ} \geq$ 35 mJy and $F_{5GHz} >$ 20 mJy) and optically limited ($B < 19$) with a cut in the radio spectral index ($\alpha_r < 0.5$). The sample includes 332 objects and the survey is $\sim$ 84% identified (Laurent-Meuhleisen et al. in preparation)

The most important result on which all of these surveys agree is the existence of a large number of "intermediate" BL Lacs, filling the gap between the LBL and HBL selected by the classical samples. This agrees with the expectations of the existence of a continuous transition between LBLs and HBLs, as proposed by Giommi & Padovani (1994). Other important results are the existence of a continuous sequence of relative importance of the BL Lac core and of the thermal stellar contribution, going from BL Lacs to normal ellipticals (e.g. Caccianiga et al. 1999) and the discovery of a large number of high-energy peaked FSRQ (HFSRQ) (Perlman et al. 1998) whose existence was not predicted in some models (e.g. Sambruna et al. 1996). The evolution of BL Lacertae objects is still not clear: both in DXRBS preliminary results (Padovani 2001) and in the REX complete sub-sample (Caccianiga et al. 2001) BL Lacs are consistent with no evolution, but while the DXRBS sample is not completely identified yet, the REX complete sample is probably too bright to detect the negative evolution found in the EMSS sample. Strong negative evolution is found in the "sedentary" survey at low radio fluxes (Giommi, Menna & Padovani 1999), as expected in the case of anti-correlation between the synchrotron peak position and the cosmological evolution, but the same authors (Giommi et al. 2001) argue that this could be an artifact due to a number of causes, such as (1) eventual optical incompleteness, (2) dependency of the Doppler factor on the radio luminosity or (3) possible flattening of the radio luminosity function at the low luminosity end. The complete identifications of the on-going surveys are waited for to shed some light on this issue.

Chapter 9

The BLEIS project

A completely different approach to solve the puzzles introduced by the "classical" surveys is to select a sample of blazars in a different energy band, possibly between the commonly used radio and X-rays. The optical band is the most easily accessible with the present facilities but the best optically selected sample available to date is the PG sample (Green et al. 1986; Fleming et al. 1993) with 6 BL Lacs only (2 LBLs and 4 HBLs) down to $B \sim 16$. A larger and fainter optical blazar sample can give a new answer to the dichotomy introduced by the classical samples e.g. regarding the BL Lacs evolutive properties or the quasar counts.

Since the brightest BL Lacs of the 1 Jy and of the IPC slew survey have comparable optical magnitudes, the optical band could be a less biased region to look for the relative number of LBLs and HBLs. This number is in fact now known with an uncertainty of two orders of magnitude and present samples cannot discriminate between the different proposed scenarios; an optical sample could. A faint radio flux is another extremely important goal to be reached:
- because different scenarios on the relative numbers of LBLs and HBLs start to differ at low radio fluxes (e.g. Fossati 2001);
- to determine the faint radio number counts of FSRQ, SSRQ (Steep Spectrum Radio Quasar, separated from FSRQ $\alpha_r = 0.5$), radio galaxies and BL Lacs to check for the presence of evolution and to test the unified models, which predict the number of quasars to drop at flux levels of $\sim$ 0.1 Jy and to completely disappear at $\sim$ 10 mJy (e.g. Padovani & Urry 1992);
- to determine a detailed luminosity function at low radio power to derive accurate values for the unification models parameters (e.g. value

of the opening angle or of the beaming factor);
- to define the sources that emit at faint flux levels; in the mJy region different models predict different importance of the various classes of sources. For example, at 1.4 GHz down to 5 mJy the model of Jackson & Wall (1999) predicts $\sim 3-4$ BL Lacs deg^{-2}, while Urry, Padovani & Stickel (1991) predict ~ 0.8 deg^{-2};
- to find the redshift distribution of radio galaxies (FRII and FRI according to the classification of Fanaroff & Riley, 1974) and BL Lacs and quasars to check the correct unification scheme (FRII, SSRQ and FSRQ, as in Urry & Padovani 1995, or high-excitation FRII as parent population of quasars and low-excitation FRII and FRI as parents of BL Lacs, as proposed by Jackson & Wall 1999).

With the goal of selecting the FAINTEST blazar sample ever in the OPTICAL band we started the BLEIS (BLazars + EIS) project (Cagnoni et al. 2000), a search for blazars from the faint optical images of the ESO Imaging Survey Wide (EIS Wide, e.g. Nonino et al. 1999). Other results from the BLEIS project will be e.g. the selection of a) a sample of high redshift quasars and b) a sample of radio galaxies. These samples will be important on their own to obtain an independent estimate on the very high redshift population of radio-loud quasars, as a test for evolutionary and unification models and for other statistical studies.

9.1 The EIS Wide

We used for our project the EIS Wide, a survey covering 4 regions of the southern sky for a total of ~ 16 deg^2 in up to two colors, spanning the right ascension range $22^h < \alpha < 9^h$. EIS Wide was planned with the goal of generating a unique publicy available database for the ESO community to prepare the widest possible range of programs for the first two years of operation of VLT and for the search of distant clusters of galaxies and quasars (e.g. Renzini & Da Costa 1997). Table 9.1 summarizes the positions and the sky coverage for each filter.

EIS wide consists of a mosaic of overlapping EMMI-NTT frames ($9' \times 8.5'$) with each position of the sky being sampled twice for a total integration time of 300 s. To ensure continuity adjacent frames have a small overlap at the edges ($\sim 20''$) and a small fraction of the surveyed area may be covered by more than 2 frames. The average limiting

Table 9.1: EIS Wide sky coverage

Name	Center Position		Area Covered (deg^2)		
			B	V	I
Patch A	22:43:03	-39:58:30	–	1.2	3.2
Patch B	00:48:22	-29:31:48	1.6	1.5	1.6
Patch C	05:38:24	-23:51:54	–	–	6.0
Patch D	09:51:40	-21:00:00	–	–	6.0
Total			1.6	2.7	16.8

magnitudes at the 80% completness for the images are B=24.6, V=24.4 and I=23.7 (Nonino et al. 1999; Da Costa et al. 1999).

9.1.1 Sources selection: the pilot sample

We started our analysis from Patch B (1.6 deg^2), the only region covered with all the 3 optical filters (B, V and I). Since blazars are all radio emitting sources, we cross-correlated each EIS Patch B filter catalogs with the NRAO VLA Sky Survey (NVSS, Condon et al. 1998) sources. The NVSS is a radio survey that covers the whole sky north of J2000 $\delta = -40$ ($\sim$ 82 % of the celestial sphere); it was performed at 1.4 GHz using the compact D and DnC configurations of the Very Large Array (VLA) in Socorro, New Mexico. The NVSS products consist of 2326 $4^\circ \times 4^\circ$ maps containing information on the total flux and linear polarization in the form of Stokes parameters I, Q and U. The NVSS source catalog was extracted from the Stokes I images and it is available to the scientific community in electronic form.

We excluded from the cross-correlation all the optical sources fainter than the catalogs 80% completeness limits and used a first screening cross-correlation radius of $10''$; we later restricted the search in a radius equal to the uncertainty on the radio position for each source (as cataloged in the NVSS) and to two times this value.

We cut the NVSS catalog at two different flux levels: 2.5 mJy, the NVSS flux limit, and twice this value and considered only the "matching" radio sources. We consider a radio source to have a "match" when there is at least one counterpart per filter. For most of the cases the counterpart in one filter is within $0.8''$ from the sources detected in other filters. We considered these counterparts to be different detections of the same source. In some cases the counterparts found in different filters fall further away one from the other and we do not

consider them to be the same source. The nominal uncertainty on the position for all the EIS patches is 0.03″ (Da Costa et al. 1999), but we found this value to be larger ($\sim$ 0.5″) probably due to the lack of bright stars on which good astrometry can be performed. The EIS number counts down to the 80% completness limits are so high ($\sim 2 \times 10^5$ src deg^{-2}, Prandoni et al. 1999) that more than one counterpart is expected as chance coincidence for the 5 sources with NVSS positional uncertainty larger than 7″; indeed this is the case. The total number of counterparts is 24 in the V-band, 24 in the I-band and 23 in the B-band. The results of these cross-correlations are summarized in Table 9.1.1.

Table 9.2: EIS Wide - NVSS cross-correlations

Radius (σ)	Flux (mJy)	No. of sources
1	2.5	22
1	5	5
2	5	15

We decided to use 5 mJy as radio limit, corresponding to $\sim$ 10 times the rms of the Stokes I images, to have accurate positions (95% error circle smaller than 5″ and to guarantee the completeness of the sample (Condon et al. 1998). We chose the larger 2σ radius for the cross-correlation because we considered it safer not too loose sources even if the EIS Wide positional accuracy was stated to be extremely precise ($\sim$ 0.03″, Da Costa et al. 1999).

We were thus left with a pilot sample composed of 15 sources.

9.1.2 Optical color classification

For a first attempt to classify the sources we used the optical color classification presented in Zaggia et al. (1999). We added to this scheme a region (region 2 in Figure 9.1 left) representing the optical colors of BL Lacertae objects derived from Moles et al. (1985). The resulting classification pattern is presented in Figure 9.1 (left): in region 1 the low redshift ($z < 3$) and in region 3 the high redshift ($z > 3.5$) quasars are expected; regions 4 and 5 are occupied by very low mass stars and white dwarves respectively and region 2 should be populated by BL Lacs.

Figure 9.1 (right) shows where the 24 V-band counterparts of the pilot sample fall on Zaggia's diagram: 5 counterparts are in the region occupied by high redshift quasars ($z > 3.5$), 3 (3 radio sources) in the low redshift quasar region ($z < 3.5$), 4 in the BL Lac region and 4 fall out of the known regions. 7 counterparts are not visible in the I and/or B filters and, obviously, are not included in the plot.

The result of such a classification on the 15 BLEIS sources is: 2 sources fall in the BL Lac region, 3 in the low z QSO, 3 in the high z QSO and 7 sources have not clear classification on Zaggia's plot.

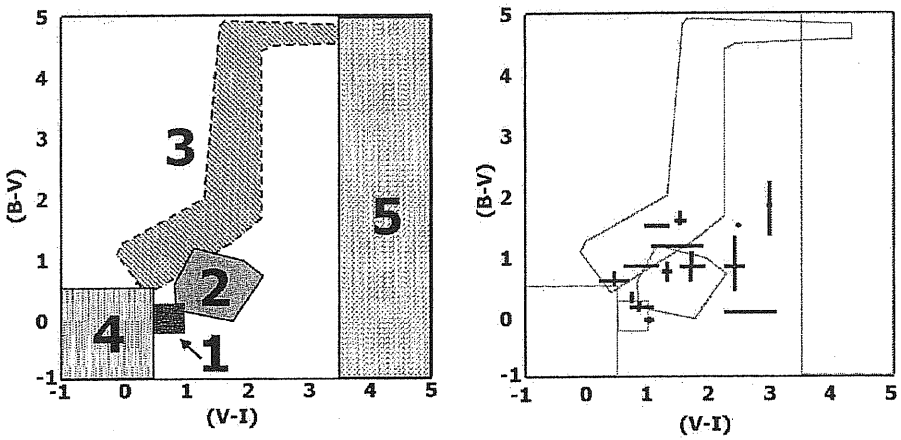

Figure 9.1: (Left) Classification based on optical colors: in region 1 the low redshift ($z < 3$) and in region 3 the high redshift ($z > 3.5$) quasars are expected; regions 4 and 5 are occupied by very low mass stars and white dwarves respectively (Zaggia et al 1999). Region 2 represents the colors of BL Lacertae objects measured by Moles et al (1985). (Right) Optical classification of the V band counterparts of the BLEIS pilot sample.

9.1.3 Chance coincidences

The flux density down to B=24.6, V=24.4 and I=23.7 is $\sim 2.4 \times 10^5$ src deg^{-2} 2.2×10^4 src deg^{-2} (Prandoni et al. 1999 for the EIS and Huang et al. 2001 for a recent review of deep sources counts). With a radio source density of $\sim$ 23 sources down to 5 mJy and a 95% error circle of 5″ radio, this translates into $\sim 4 - 5$ sources expected as chance coincidence in the Patch B area. This corresponds to $\sim$ 30% of the pilot sample.

9.1.4 α_{ro} distribution

By extrapolating the NVSS flux (assuming a flat slope to 5 GHz) and using the EIS V magnitudes we estimated the α_{RO} distribution for our sources and compared it to various classes of sources, namely: the X-ray selected BL Lacertae objects of the *Einstein* Slew Survey (Elvis et al. 1992); the radio selected BL Lacs of the 1 Jy sample (Stickel et al. 1994); the radio galaxies of the 3CR sample (whose flux was extrapolated to 5GHz assuming an average slope for the radio spectrum of $\alpha = 0.7$); the Flat Spectrum Radio Quasar sample selected by Padovani & Urry (1992) from the '2Jy sample' of Wall & Peacock (1985). The α_{ro} distribution of the BLEIS sources is compatible with those of radio selected BL Lacs and FSRQ, as clear in Figure 9.2.

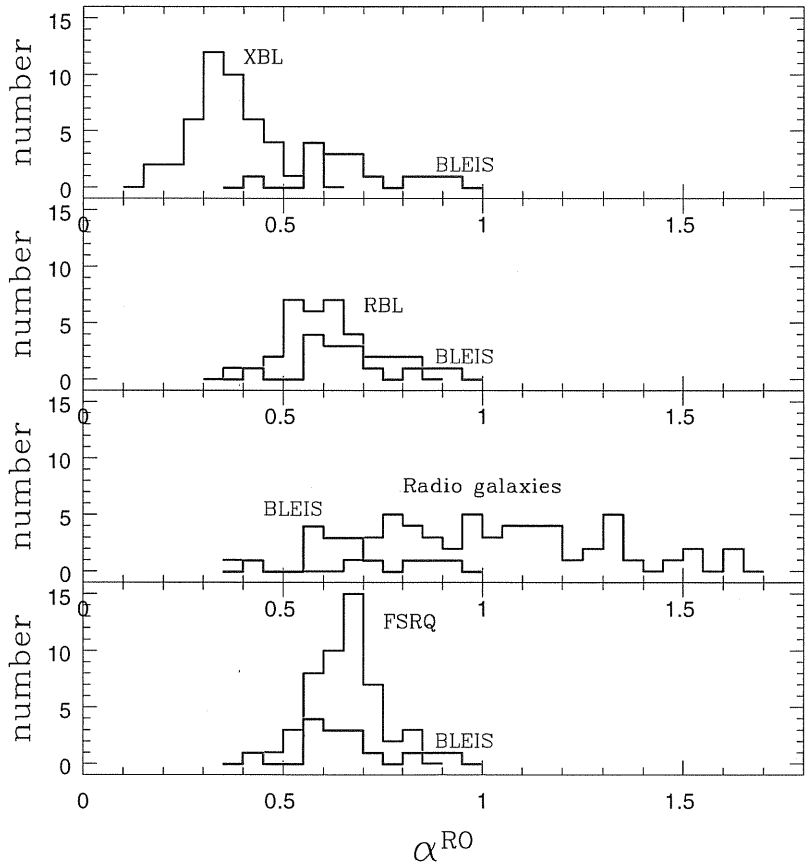

Figure 9.2: BLEIS sources α_{ro} distribution compared to those of XBL, RBL, radio galaxies and FSRQ. See text for details.

Chapter 10

Comparison with models

If we assume that the optical classification proposed by Zaggia et al. (1999) is correct we can compare the observed candidates with model predictions. In the following sections we will detail on each class of objects.

10.1 BL Lacertae objects

10.1.1 Radio band

We found 2 BL Lacertae objects in 1.6 deg^2 or 1.25 ± 1.12 deg^{-2} BL Lacertae in the BLEIS. Due to the large error associated with such a small number, the BLEIS number counts are compatible both with the ~ 0.8 BL Lacertae deg^{-2} predicted by the models of Urry, Padovani & Stickel (1991) (see Figure 10.1) and the $\sim 3-4$ BL Lacs deg^{-2} predicted by Jackson & Wall (1999) at these flux limits in the radio band.

The most recent BL Lacertae number counts come from the DXRBS (Padovani et al. 2000), one of the new blazars surveys; at 50 mJy at 5 GHz they find ~ 0.06 src deg^{-2}, which is consistent with Urry, Padovani & Stickel (1991) predictions. The number counts of the candidate BL Lacertae objects found in the BLEIS is thus consistent with theoretical predictions, but due to the small statistics and the large error associated with this quantity, we are not able to discriminate between competing models (e.g. Urry, Padovani & Stickel 1991; Jackson & Wall 1999). A larger sample is needed for this goal.

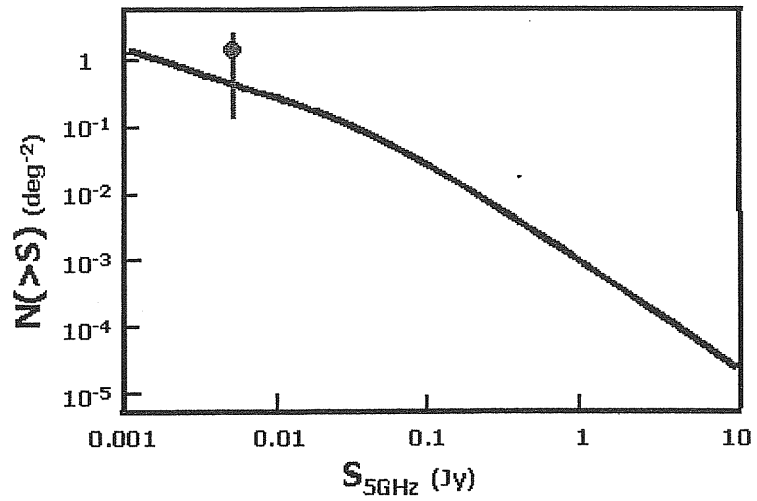

Figure 10.1: BLEIS BL Lacerate candidates number counts in the radio band (red point) compared to model predictions by Urry, Padovani & Stickel (1991) (solid line)

10.1.2 Optical band

Figure 10.2 shows a comparison of the BLEIS candidate BL Lacertae objects in the optical band with the predictions of Padovani & Urry (1991).

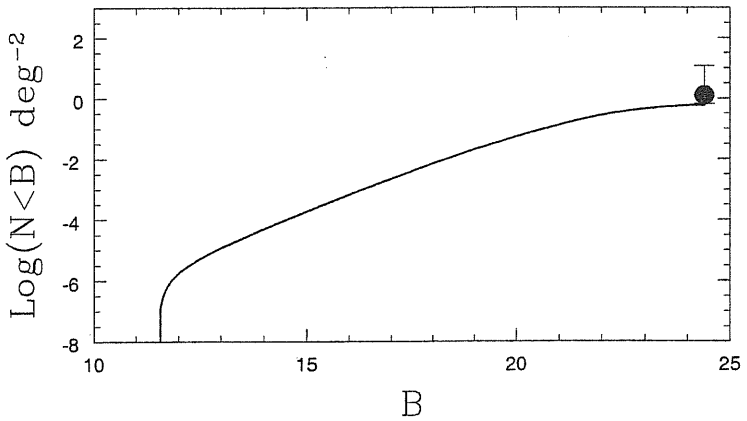

Figure 10.2: BLEIS BL Lacertae candidates number counts in the optical band (red point) compared to model predictions by Padovani & Urry (1991) (solid line)

Even in the optical band, the BLEIS density of candidate BL Lacertae objects is consistent with model predictions.

10.2 Quasars

10.2.1 Radio band

According to Zaggia's classification, we find in the BLEIS a total of 6 quasars (4 at high z and 2 at low z) in 1.6 deg^2 or 3.75 ± 1.9 quasars deg^{-2}.
According to Padovani & Urry (1992) ~ 0.17 FSRQ deg^{-2} and ~ 0.84 SSRQ deg^{-2}, for a total of ~ 1 quasar deg^{-2} are expected at a flux limit of 5 mJy. There is an indication of BLEIS candidate quasars to be higher than model predictions in the radio band, but, due to the large errorbars associated with these small numbers we cannot draw any firm conclusion.

10.2.2 X-ray band

The BLEIS sources in our sample are too faint to be observed in the X-ray band. In fact, assuming an average broad-band spectral index for FSRQ of $\alpha_{rx} \sim 0.8$ (Fossati et al. 1998) we find $F_{X(1-10\mathrm{keV})} \sim 10^{-15}$ erg cm^{-2} s^{-1} hard to reach with the presently available X-ray telescopes. Nevertheless we can compare the BLEIS candidate quasars space density with the deepest number counts for X-ray selected quasars from Wolter & Celotti (2001) in Figure 10.3. We also added in the same figure the BLEIS candidate BL Lacs extrapolated to the X-ray band with the same $\alpha_{rx} = 0.8$ used for the quasars (Fossati et al. 1998).

We note that while BLEIS candidate BL Lac counts are roughly consistent with the extrapolation of the EMSS number counts from Wolter et al. 1991, a flattening of the quasars counts at $\sim 10^{-14}$ erg cm^{-2} s^{-1} is needed to reconcile the BLEIS candidate quasars with the EMSS quasars from Wolter & Celotti (2001).

10.3 All the radio emitting sources

We have a total of 15 sources with radio flux above 5 mJy with an optical counterpart visible in the B,V,I bands down to B=24.6, V=24.4 and I=23.7. These sources have a broad band spectral index $0.35 < \alpha_{ro} < 1.05$, compatible with RBL and FSRQ and only partially overlapping with the radio galaxies and with the XBL distributions. According to Zaggia's optical classification (§ 9.1.2) BLEIS sample is

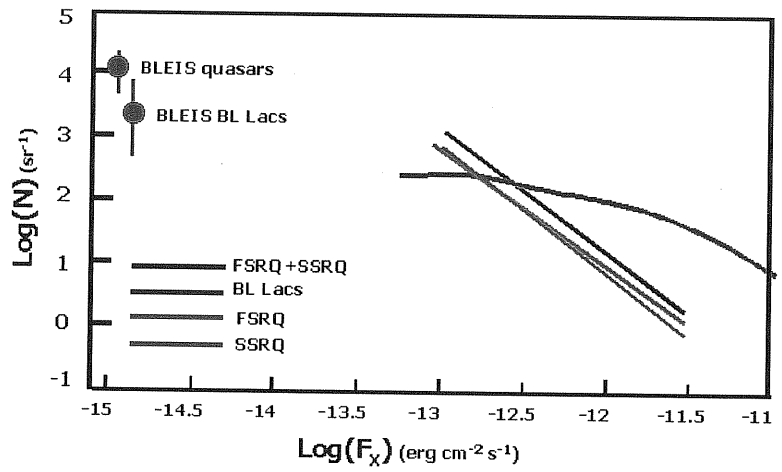

Figure 10.3: BLEIS quasars and BL Lacertae candidates number counts (red points) converted to the X-ray band assuming $\alpha_{rx} \sim 0.8$ compared to the EMSS counts. The blue line represents the BL Lacs from Wolter et al. 1991 while the green, the pink and the black lines represent FSRQ, SSRQ and the total quasars counts from Wolter & Celotti (2001).

composed of: 13% BL Lacs, 40% quasars and the remaining 47% has no clear classification.

Theoretical models predict different relative importance of the various source; for example according to Jackson & Wall (1999) we would expect the radio emitting sources down to 5 mJy to be: 30% FRII, 38% FRI, 17% BL Lacs and 15% starbursts.
Danese et al. (1987) model at 5 mJy predicts 17.5% of the sources to starbursts galaxies, another 17.5% QSOs, 64% elliptical galaxies and 1% irregular and spiral galaxies.
These and other models agree that a large fraction ($\geq$ 60%) of the radio emitting sources down to 5 mJy at 1.4 GHz are radio galaxies (called FRI and FRII in Jackson & Wall 1999 and ellipticals in Danese et al. 1987) and another consistent fraction ($\sim 15-20\%$) is composed by starburst galaxies.

Since these classes of sources are not included in Zaggia et al. (1999) we checked which is the region of the diagram they are likely to occupy. To obtain the colors of the starbursts galaxies we used the synthetic model starburst99 by Leitherer et al. (1999), while for the radio galaxies we used the colors of the elliptical galaxies observed by Goudfrooij et al. (1994). We reported the loci of these two classes of sources on Zaggia et al. (1999) diagram in Figure 10.4.

As clear from the figure above Zaggia's diagram is not completely

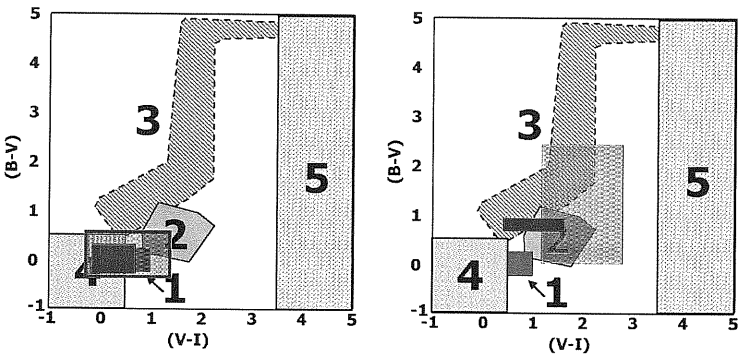

Figure 10.4: Expected loci of (left) starbursts galaxies from Leitherer et al. (1999) and (right) radio galaxies from Goudfrooij et al. (1994) on Zaggia (1999) classification scheme. The colored region in the left panel shows the expected colors of starbursts galaxies for models of instantaneous (larger shaded red area) and for a continuous burst model (smaller filled red area); on the right panel the larger shaded red area represents the measured colors, while the smaller filled red area shows the same colors when corrected for dust absorption (Goudfrooij et al. 1994)

reliable for classification purposes and radio or optical spectral information are needed to discriminate among the various classes of objects. However we note that the α_{ro} distribution of the sources we selected (Figure 9.2) is not consistent wih them being starburst galaxies ($\alpha_{ro(\text{starbursts})} \leq 0.1$, e.g. Magliocchetti & Maddox, 2001).

10.3.1 Patch A and ATESP

Being the most southern area sampled in the EIS-Wide, no NVSS data is available for Patch A, but this area was observed at 1.4 GHz in the ATESP survey (Prandoni et al. 2001) down to a radio flux of ~ 0.5 mJy. Prandoni et al. (2001) cross-correlating the ATESP and the I-band catalog of Patch A of the EIS-Wide find $\sim 9\%$ of AGNs, 60% of early type spectrum galaxies, 13% of starbursts and 20% of late type galaxies down to a radio flux $S \sim 1$ mJy and to $I \sim 22.5$. These results are consistent with the expectations of theoretical models.

10.4 Conclusions and future work

The work presented in this thesis represents a pilot study for the possibilities of using deep optical data to select a sample of blazars. Using a ~ 1.6 deg^2 area (Patch B) of the EIS-Wide we were able to select a sample of 15 sources. We attempted an optical classification using

the scheme based on optical colors presented in Zaggia et al. (1999) and compared the results with number counts from theoretical models. Two are the largest limitations that prevent us to draw any firm conclusions:
(1) - the Zaggia et al. (1999) is likely to be contaminated by radio galaxies, which constitute $\sim 60\%$ of the predicted objects at the sample radio fluxes. An optical spectrum or at least another flux estimate in the radio band, which would allow a distinction among the various sources based on their radio spectrum, are needed.
(2) - the statistics we obtained from the pilot study performed on a area of the sky of just 1.6 deg^2 is not enough to discriminate between different models (§ 10).

The obvious continuation of this work is thus to obtain a classification of these objects in the pilot sample with optical spectroscopy and to extend the work to the whole area of the sky covered by the EIS-Wide ($\sim$ 16 deg^2). We have both NVSS and deep I-band imaging both for Patches C and D; the addition of these two patches will define a $\sim$ 7.5 times larger sample and provide the statistics necessary to constraint theoretical models.
An optical spectrum will be useful to:
- obtain a classification for the sources and estimate the number counts of blazars down to these faint flux limits and constrain theoretical models.
- Find a redshift for the sources and compute the redshift distribution of the sample. According to Jackson & Wall (1999) the sources emitting in the energy range $10^{-5} - 10^{-2}$ Jy should mainly be low power radio sources at intermediate redshift, in contrast to the powerful radio sources at cosmological redshift which dominate between 0.1 and 150 Jy, but this is an area still unknown from the observational point of view.
- Construct the luminosity function of the various classes of objects and blazars in particular, to the faintest level ever to check for evolution.

Improvements could also be obtained with other radio observations: more accurate positions (e.g. $1''$ as in the ATESP, Prandoni et al. 2000) will guarantee an unambiguous association of the radio and optical sources, not possible with the presently available NVSS positional

accuracy. A lower flux limit (e.g. ~ 1 mJy) would enlarge the already selected sample in the B patch and would allow the selection of interesting sources in the other EIS patches; according to Jackson and Wall (1999) the fraction of blazars would remain unchanged.

From the pilot study we performed in this part of the thesis we conclude that the selection of faint optical samples of blazars, radio galaxies and quasars is a powerful test for unification and evolutionary models, but much work is still to be done before being able to set any stringent constraint.

Part III

MRK 421

Chapter 11

Introduction

The previous part of the thesis deals with the search for a faint blazar sample and this part presents the detailed analysis of one of the closest and brightest examples of this class of objects: the BL Lacertae object MRK 421. We study in detail the EUV emission of MRK 421 both in terms of spectral and timing analysis. This part of the thesis is organized as follows: after a brief introduction on BL Lacertae objects and on MRK 421 in particular and after explaining the aim of the study, we show the method and the results of the spectral (§ 12) and timing (§ 14) analysis and discuss the results in § 13 and in § 15 respectively and summarize the work done in § 16.

BL Lacertae objects are part of the blazars class presented in the previous part of this thesis. BL Lacertae objects, as the other blazars, are an extreme subclass of Active Galactic Nuclei (AGNs) emitting highly variable non-thermal radiation over 20 decades of frequency from radio to TeV energies. The mechanism responsible for the production of radiation over such a wide range is thought to be synchrotron emission followed by inverse Compton scattering from energetic electrons. Some of the extreme properties of BL Lac objects, such as rapid variability, high gamma-ray luminosities and superluminal motion (e.g. Urry & Padovani 1995), are explained invoking relativistic beaming of the emitted radiation along the jet axis which is taken to be oriented at small angles to the line of sight. BL Lac objects were originally defined as a class and distinguished by the other blazars (i.e. FSRQ) by their lack of the sharp spectroscopic features in their optical spectra, that provide the normal tools for understanding astrophysical objects.

Absorption features are extremely important in astrophysics because they can provide a unique tool to study the presence and the dynamical properties of any gas surrounding the central nucleus, but BL Lacs seemed to lack this tool, at least in the optical band.
Despite the definition of BL Lacertae objects as optically lineless sources, evidence for absorption features in the X-ray spectra of some BL Lac objects at $\sim 0.5 - 0.6$ keV (e.g. PKS 2155-304, Canizares & Kruper 1984; AO0235+164, Madejski et al. 1996; H1426+428, Sambruna et al. 1997 and PKS 0548-322, Sambruna & Mushotzky 1998 and see § 13.1 for a detailed discussion) has existed for many years, but since these features fell in a critical region for instrumental calibrations[1] their existence and importance was still under debate (e.g. Brinkmann et al. 1994).
According to theoretical models (see § 13.1) the ~ 0.6 keV absorption was expected to have a related EUV feature and scientists went looking for it with the *Extreme UltraViolet Explorer* (*EUVE*). It was soon realized that even at low Galactic column densities the absorption in the EUV band was such to require extremely long (weeks, compared to hours or even minutes in X-rays) pointings to gather enough photons for a spectral detection even for X-ray bright objects and the only two BL Lacs bright enough for a spectrum were MRK 421 and PKS 2155-304. Spectral features in the EUV band were inferred for both these objects extrapolating the X-ray energy spectrum (Konigl et al. 1995 and Kartje et al. 1997). The weakness of *EUVE* in the spectral domain brought to the collection of the longest and best sampled lightcurves at high energies.

Strong and rapid variability is one one the main characteristics of the blazars class and variability studies are powerful tools in constraining emission mechanisms. In particular the power spectrum of a source (e.g. § 14.2) is the footprint of the emission mechanisms which dominate in the source; the slope, changes in the slope, periodicities and all the features that could be found in a power spectrum are the marks of characteristics time scales (e.g. minimum and maximum variability time scales) which are in turn related to the physics of the object itself. At least two characteristics time scales are expected in the power spectrum of any source:

[1] In the energy range $\sim 0.3 - 0.6$ the effective area of all satellites is greatly reduced and discontinuous because of the presence of the K-edges of C, (0.28 keV), N (~ 0.4 keV) and O (~ 0.53 keV), the constituents of the windows supports

- a sharp steepening toward short time scales which reflects the minimum variability time scale and is set by the size of the emitting region (with the eventual modification of beaming effects);
- a flattening toward long time scales, related to the maximum variability time scale. The existence of this flattening is necessary to constrain the maximum variance of the source.

While the minimum variability time scale is nowadays covered up in the Poisson noise related to the observation, the long time scale break is in principle observable, providing that enough time is spent on the same source. Thanks to *RXTE* we have examples of low frequency breaks in the power spectrum of radio quiet AGNs ranging from few hours (e.g. McHardy et al. 1998 for NGC4051) to few months (e.g. Chiang et al. 2000 for NGC 5548), but this feature has never been found in a radio loud AGN.

Because of the potential consequences both of a spectral analysis and of a temporal analysis for a BL Lac in the EUV range and because a lot of data was already public in the *EUVE* archive we decided to select a representative of the BL Lac class and to study it in detail.

11.1 MRK 421: the best BL Lac to be investigated

As we mentioned above, *EUVE* spectral capabilities are strongly limited by the amount of interstellar matter (ISM) and to have a good signal to noise, only bright and/or nearby objects can be taken into consideration. MRK 421 is one of the brightest, best known and closest BL Lac objects (z=0.0308, Ulrich et al. 1975). MRK 421 was in fact the first BL Lac object found to have X-ray emission (Richetts et al. 1976) and its low redshift makes this object one of the few extragalactic sources detected at γ-rays above 300 GeV up to TeV energies (Punch et al. 1992). MRK 421 has been extensively observed at radio (e.g. Zhang & Baath 1990), UV/optical (Maza, Martin & Angel 1978; Mufson et al., 1990) and X-ray frequencies (e.g. Mushotzky et al., 1979; George, Warwick & Bromage 1988, Takahashi et al. 1996, Guainazzi et al. 1999, Fossati et al. 2000a; 2000b). MRK 421 shows optical polarization, a flat radio spectrum and significant time variability, characteristics of the blazar class (Makino et al., 1987) and its parent galaxy has been identified as a giant elliptical (Ulrich et al. 1975; Mufson, Hutter & Kondo 1989).

MRK 421 is thus a good candidate to look at, but it is far superior to the other close and bright BL Lac observed by *EUVE* (e.g. PKS 2155-304) because of the extremely large amount of data collected for it.
In the EUV band ($\sim 60 - 750$ Å) MRK 421 was detected during the *ROSAT* WFC survey (Pounds et al. 1993; Pye et al. 1995) and the *EUVE* all-sky survey (Marshall, Fruscione & Carone 1995, Fruscione 1996). It is one of the strongest EUV extragalactic sources and was immediately recognized as a prime target for subsequent EUV spectroscopic studies. For 4 almost consecutive years (1994, 1995, 1996 and 1998) MRK 421 was the target of multiwavelength campaigns covering radio to TeV energies (Macomb et al., 1995, Kerrick et al. 1995, Buckley et al. 1996, Takahashi et al. 1999) and the *EUVE* satellite (which gives simultaneous photometric and spectroscopic data) was always part of the campaigns. In addition, in 1995 and in 1997 MRK 421 was observed serendipitously with the *EUVE* photometers (the "scanners").
The large amount of data accumulated for MRK 421 by the *EUVE* satellite to date ($\sim$ 1100 ks of public imaging data and $\sim$ 950 ks of public spectroscopic data) represents the best coverage for any BL Lac object at high energies. Less than half of this data has been analysed to date (Fruscione et al. 1996, Kartje et al. 1997, hereafter K97) revealing that (i) the source exhibits a flare-like behavior (ii) the strong EUV variability is correlated with soft X-ray and TeV-energy emission, and (iii) the spectrum may have strong absorption features between 65 Å and 75 Å (0.16-0.19 keV) (K97). However the presence of absorption was inferred from the extrapolation of the X-ray spectrum and using the inappropriate on-axis effective area, which, as explained in § 12 has the effect of increasing the importance of the feature.

The purpose of this work is to analyze, in an homogeneous way, all of the *EUVE* public data for MRK 421 in order to perform the first detailed variability analysis for a BL Lacertae object in the EUV and to check for the presence of absorption lines in the energy spectrum, which might only be the effect of the use of an inappropriate calibration and of the extrapolation of the X-ray spectrum used in K97.

11.2 The EUVE satellite and MRK 421 observations

The *EUVE* satellite was launched in June 1992 and is still acquiring astronomical data in the wavelength range from $\sim$ 60 to 750 Å. Onboard *EUVE* there are 4 telescopes: three of them are co-aligned photometers observing in 4 different EUV bandpasses, while the fourth is the Deep Survey/Spectrometer (DS/S, see e.g. Welsh et al. 1990) mounted orthogonally to the scanners. (Figure 11.1 shows the DS effective area compared to the scanner effective area).

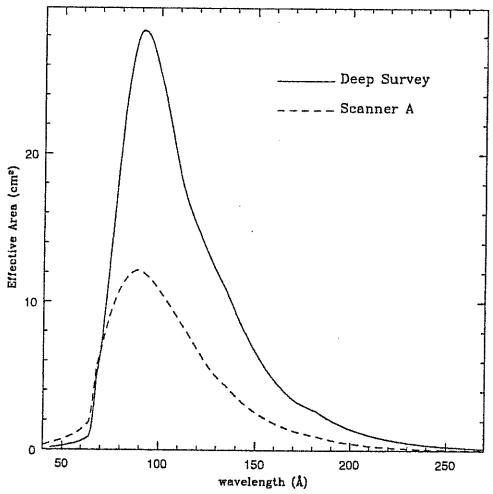

Figure 11.1: Comparison of the effective areas of the Deep Survey (solid line) and scanner A (dashed line) instruments on board the *EUVE* satellite.

In addition to a photometer (10 % bandpass 68-178 Å) the DS/S telescope is also equipped with three spectrometers (Hettrick & Bowyer, 1983; Abbott et al. 1996) covering the "short" (SW: 70 – 190 Å), "medium" (MW: 140–380 Å) and "long" (LW: 280–760Å) EUV wavelengths. This configuration allows simultaneous imaging and spectroscopy with a spatial resolution of $\sim 1'$ and a spectral resolution of $\lambda/\Delta\lambda \sim 200$ at the short wavelengths, i.e. 0.35 Å at 70 Å.
Further details on the science instrumentation and performances can be found in Malina (1994), Sirk et al. (1997) and Abbott et al. (1996).

The scanners were used to carry out the *EUVE* all-sky survey (July 21 1992 - January 23 1993) and are currently utilized in the Right Angle Program (RAP), that is the observation of targets of scientific interest with the scanner telescopes while the DS/S telescope is conducting the primary science observation. The DS/S has been used for a deep EUV

survey along the ecliptic during the all-sky survey and for pointed spectroscopic and imaging observations since then.

We use throughout this thesis all of the publicly available DS/S spectroscopic and imaging data on MRK 421: from 1994 to 1997, a total of 950 ks and 1100 ks respectively. We are not considering the most recent observation (April 1998) since the data is presently being analysed by the original proposers (Marshall et al. in preparation). MRK 421 was observed by *EUVE* several times from 1994 to 1997, four times with the DS/S and twice with the scanners; Table 11.1 summarizes the observations.

Because of strong absorption by the interstellar medium (ISM) along the line of sight (even at the low $N_H = 1.45 \times 10^{20}$ cm^{-2} Elvis, Wilkes & Lockman 1989), MRK 421 was detected only at the shortest wavelengths: in the Lex/B filter of the scanners (10% bandpass 58-174 Å), in the Lex/B filter of the DS instrument (10% bandpass 67-178 Å) and, relevant for this thesis, in the SW spectrometer (70-190 Å) [2].

11.3 Serendipitous sources

Two faint serendipitous sources are clearly visible next to MRK 421 in the DS image. We identified the closest one ($\sim 2'$ from MRK 421) with 2 unresolved stars in a double system: HD 95934 ($M_V = 6.00$, Spectral type A3III-IV) and BD+39 2414B($M_V = 12.6$). The other one at $\sim 4'$ from MRK 421 was identified with another star in double system: HD 95976 ($M_V = 7.4$, Spectral type FII).

The DS 50% energy radius is about $0.3'$ up to $0.3°$ off-axis. In scanner A, this half energy radius is $\sim 3'$ at $\sim 1.5 - 2°$ off-axis (where the sources lied in the 1995 and 1997 observations) and the sources are not resolved. During the analysis of DS data we excluded a circle centered on HD 95934; this excluded only a negligible fraction of counts from MRK 421 .

[2] A graphical representation of the simulated DS/S and scanner responses is presented in Figure 11.1, where we convolved the MRK 421 energy spectrum corrected for the ISM absorption with the DS/S and scanners effective area. No signal is present at wavelengths longer than ~ 110 Å

Table 11.1: EUVE Observations of Mrk 421

Year	Start	End		Instrument[a]	T_{exp}[b] (ks)	Count rate[c] (10^{-2} c s^{-1})	Spectrum	Variability factor
1994	2 Apr	12 Apr[d]		DS	280	18 ± 0.85	yes	2
1995	4 Feb	7 Feb		ScaA	68	32 ± 2.9	no	1.5
						45 ± 4.1[d]		
1995	25 Apr	13 May		DS	355	29 ± 0.96	yes	3
1995	25 Apr	28 Apr	(flare)[e]			37 ± 2.3	yes	
1995	29 Apr	6 May	(decay)[e]			29 ± 1.5	yes	
1995	7 May	13 May	(quiescence)			22 ± 1.0	yes	
1996	17 Apr	30 Apr		DS	299	30 ± 1.08	yes	1.4
1996	10 May	11 May		DS	3.6	40 ± 1.1	no	
1996	7 Feb	11 Feb		ScaA	108	19 ± 1.6	no	2
						27 ± 2.2		

[a] "DS" indicates that the source was observed in the Deep Survey photometer. "ScaA" indicates that the source was observed in one of the three *EUVE* photometers (scanner A) during a pointing within the Right Angle Program.

[b] Total exposure time calculated eliminating (i) all SAA passages (ii) all satellite daytime data (iii) all times during which the detector was turned off (iv) all times affected by possible earth blockage. It does include corrections for telescope vignetting, deadtime and limited telemetry allocation (primbshing).

[c] Average count rate in the Lexan/B filter ($\approx 60 - 180$ Å). For the scanner observations, the second line gives the count rate normalized to the one in the DS assuming an average spectral shape, to take into account the difference in the effective area between the two instruments.

[d] This observation was presented in Fruscione et al. (1996)

[e] This observation was presented in Kartje et al. (1997)

Chapter 12

Spectral analysis

We performed a detailed spectral analysis on the 950 ks of data accumulated for MRK 421 from 1994 to 1997. After rejecting the time intervals with high particle background, such as the satellite passages over the South Atlantic Anomaly, and correcting the data for instrumental dead-time and telemetry saturation, we measured a total effective exposure of 315858 s, 506780 s, and 354806 s for the 1994, 1995 and 1996 observations respectively (note that the first 1995 and the 1997 observations were performed with the scanners, instrument with imaging capabilities only).

We extracted all the spectra in a homogeneous way from the two-dimensional SW detector image, using the *EUVE* Guest Observer Center software (IRAF/EUV package) and other standard spectroscopic IRAF tasks. The spectrum was extracted in a 14 pixel wide aperture and the background obtained by linearly fitting an average background in two regions ($\sim$ 80 pixel wide) of the detector, one on each side of the spectrum. The resulting wavelength-calibrated spectra (Figures 12.1, 12.4 and 12.9) were convolved with the proper effective area and binned over 1 Å. For the 1994 on-axis observation (Figure 12.1) we used the on-axis effective area derived from in-orbit calibrations for the 75 Å- 110 Å range. The 1995 and 1996 observations were performed off-axis (a technique that slightly increases the short-wavelength coverage, down to $\sim$ 70 Å). This results in a different effective area (Marshall et al. 1999) that we applied here for the first time. The 1σ error bars on the flux measurements shown in the figures of all the spectra were computed using the formula

$$\sigma(\lambda) = \frac{\sqrt{[S_\lambda + B_\lambda/(1 + H_{sp}/H_B)]}}{A_{eff}(\lambda)}$$

where S is the signal from the target, B the averaged background, both in counts/s, A_{eff} the SW effective area in cm^2 and H_{sp} and H_B are respectively the width in pixels of the extraction region for spectrum (14 pixels) and background (160 pixels) in the direction perpendicular to the dispersion.

We modeled the EUV spectrum of MRK 421 using version 2.0 of the SHERPA modeling and fitting software (recently developed at the Chandra X-ray Center). We initially used an absorbed power law of the form

$$\mathrm{f}(\lambda) = \mathrm{f}(\lambda_0)\lambda^{\alpha-1}\exp\{-[\Sigma_X \mathrm{N(X)}\sigma_X)\} \qquad \text{photons cm}^{-2}\ \text{s}^{-2}\ \text{Å}^{-1}$$

where $\mathrm{f}(\lambda_0)$ is a normalization factor. We used $\lambda_0 = 80$ Å (E_0=0.155 keV). α is the energy index and the absorption is characterized by a column density N(X) and an absorption cross section σ_X for each element. We included in the model H, He I and He II (Rumph, Bowyer and Vennes, 1994) and heavier elements (Morrison and McCammon, 1983). We fixed the Galactic hydrogen column density at $N_H = 1.45 \times 10^{20}$ cm^{-2} (Elvis, Wilkes & Lockman 1989) and the ratios N_{Hei}/N_{Hi}=0.1 and N_{Heii}/N_{Hi}=0.01. The best fit values for the simple absorbed power law model are summarized in Table 12.1 together with their 1σ uncertainties for 1 interesting parameter. Two-parameter χ^2 contour confidence levels at χ^2_{min}+1, +4.61 and +5.99 – corresponding respectively to the 1σ uncertainty for each single parameter and to the 90% and 95% joint confidence levels – are shown in Figure 12.2, 12.5 and 12.10 for the 1994, 1995 and 1996 data sets respectively.

12.1 1994 energy spectrum

Our best fit flux in 1994 is slightly higher than the previous analysis of Fruscione et al., 1996 ($f_{80\text{Å}} = 6.44 \pm 0.33 \times 10^{-3}$ photons cm^{-2} s^{-1} Å^{-1} compared to their $f_{80\text{Å}} = 290 \pm 15$ μJy= $5.47 \pm 0.28 \times 10^{-3}$ photons cm^{-2} s^{-1} Å^{-1}) but our slope is within the errors ($\alpha = 0.85^{+0.66}_{-0.72}$ compared to their $\alpha = 1.4 \pm 0.8$). The 1σ error bars reported in Fruscione et al., 1996 were not corrected for the effective area; the small difference in the value of the normalization can be possibly explained by the difference in the errors and a possible difference in the wavelength range used to model the spectrum. This is the only spectrum for which the addition of an absorbed inverted gaussian line does not

improve the fit (Tab.12.1).

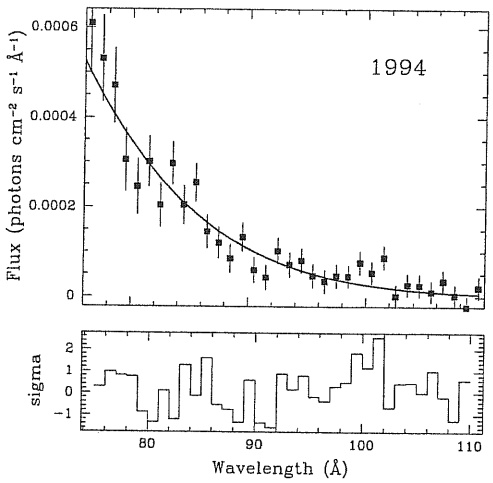

Figure 12.1: EUV spectrum of MRK 421 obtained in 1994 with the SW spectrometer. The best fit power law model is overplotted (solid line). The lower panel shows the residuals to the fit.

12.2 1995 energy spectrum

The 1995 *EUVE* DS/S observation was part of a large multiwavelength campaign during which a powerful TeV flare occurred (Buckley et al. 1996). Simultaneously an X-ray flare developed (Takahashi et al. 1996), and the EUV followed with a short delay (Buckley et al. 1996). As illustrated in Figure 12.3, the *EUVE* observation spanned the flare ($\sim$ 104 ks), the decay ($\sim$ 218 ks) and the following quiescent state ($\sim$ 185 ks).

The observation was performed $\sim$ 0.3° off-axis and as expected the signal reaches down $\sim$ 70Å. This spectral region is crucial since it covers the location of the wide EUV absorption feature proposed by K97 using less than half (the flare decay) of the 1995 data. In our analysis we corrected the data with the $\sim$ 0.3° off-axis effective area (Marshall et al. 1999) and the resulting spectrum, binned over 1 Å, is presented in Figure 12.4.

In order to compare our data analysis to that of K97, and in an attempt to look for changes during the flare, we divided the 1995 observation into three parts (Figure 12.3):
Flare: April 25–28 ($\sim$ 104ks), the time interval of the *EUVE* flare;

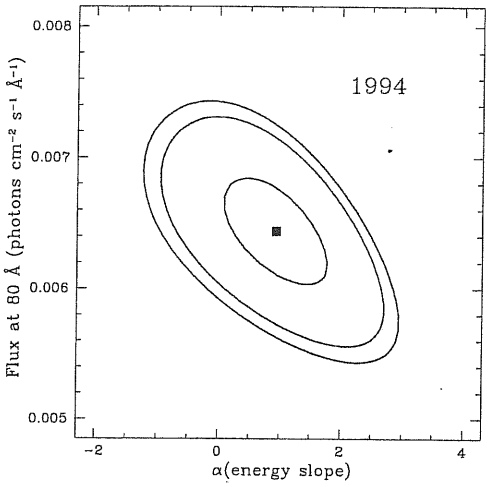

Figure 12.2: χ^2 contour confidence levels for normalization and energy index of the 1994 spectrum. The contours correspond to χ^2_{min}+1, +4.61 and +5.99, respectively the 1σ uncertainty for each single parameter and the 90% and 95% joint confidence levels. The best fit is marked by the filled symbol.

Decay: April 29 – May 6 ($\sim$ 218 ks), the time interval analysed by K97;
Quiescence: May 7–13 ($\sim$ 185 ks), the remaining data. The *EUVE* spectra for the 3 parts are shown in Figure 12.6.

Table 11.1 lists the exposures times and Table 12.1 summarizes the best-fit parameters for each one of the three parts. In Figure 12.7 we plot the two-parameter χ^2 contour confidence levels.

Table 12.1: Spectral fits to the EUV spectrum of MRK 421 assuming an absorbed power law model. Fixed parameters are $N_H = 1.45 \times 10^{20}$ cm^{-2}, N_{HeI}/N_{HI}=0.1 and N_{HeII}/N_{HI}=0.01

Obs.		Range (Å)	α	$10^{-3} f_{80\mathring{A}}^{\alpha}$ (phot cm^{-2} s^{-1} Å^{-1})	χ^2_ν
1994		75-110	$0.85^{+0.66}_{-0.72}$	6.44 ± 0.33	1.06
1995		70-110	1.13 ± 0.38	6.70 ± 0.22	2.45
Flare	Apr. 25-28	70-110	1.43 ± 0.56	10.28 ± 0.51	1.57
Decay	Apr. 29-May 6	70-110	2.19 ± 0.50	7.24 ± 0.33	1.24
Quiescence	May 7-13	70-110	$-0.60^{+1.13}_{-1.16}$	3.53 ± 0.35	1.47
1996		70-110	2.12 ± 0.31	9.32 ± 0.27	1.61

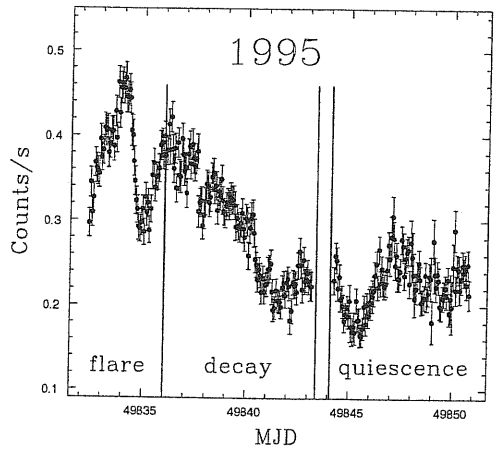

Figure 12.3: April 25 - May 13 1995 Deep Survey lightcurve binned over one average *EUVE* orbit ($\sim$ 5544 s). The "flare", "decay" and "quiescence" intervals are marked.

12.3 Comparison with previous results

The 'decay' section of the 1995 spectrum deserves comparison with the analysis of K97, given the importance of the absorption line evident in their Figure 2. We show the effect of using the improper $\sim 0.3°$ off-axis effective area in Figure 12.6 b; we compared the *EUVE* spectrum obtained using the on-axis effective area (open cirles) as in K97, and the 0.3° off-axis effective area (filled squares). The effect of using the appropriate calibration is to increase the flux below $\sim$ 80 Å and so weaken the absorption feature ($\sim$ 45%). Another effect to consider is that K97 evaluated the level of the continuum in the EUV range by adopting an $\alpha_{\rm EUVX}$ ($\approx$ 1.32) slope derived from the 0.15 keV EUV flux and the 1.5 keV X-ray (*ASCA*) flux, which resulted in a strong absorption feature (see also §3 for further discussion on this point).

Our best fit slope $\alpha = 2.19 \pm 0.5$ (Table 12.1) is flatter than the $\alpha = 3.5 \pm 0.8$ in K97. If we consider the same wavelength range (70-95 Å instead of 70-110 Å) we find $\alpha = 2.54 \pm 0.56$, consistent with K97 result.

A simultaneous fit of an absorbed power law plus an absorbed (inverted) gaussian should provide a more reliable result. If the position of the gaussian is a free parameter then the reduced χ^2 goes to 1.17 and a narrow (FWHM=1.8 $\pm$ 0.5 Å) absorption feature is found at $\sim$ 72.7 $\pm$ 0.3 Å while the slope becomes significantly flatter ($\alpha = 1.62 \pm 0.59$) (see Tab. 12.2). This is the first time that an absorption feature in the EUV range is derived from EUV data alone.

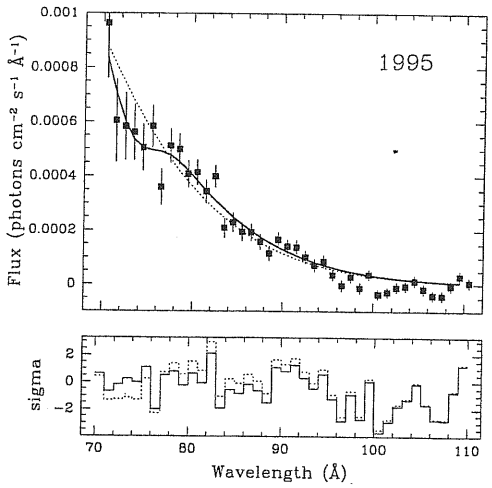

Figure 12.4: EUV spectrum of MRK 421 obtained in 1995 with the SW spectrometer during a 0.3° off-axis observation. Hence note the increased coverage toward shorter wavelengths. The best fit power law model (dotted line) and the best fit power law + inverted gaussian model (solid line) are shown together with the residuals to the fits.

Both for PKS 2155-304 (Konigl et al. 1995) and for MRK 421 (K97) the presence of absorption features was previously derived on the basis of an extrapolation of the X-ray power law and not directly from *EUVE* data. However there is strong evidence that the X-ray spectrum of the high-energy peaked BL Lac objects, including MRK 421 , is concave (Sambruna et al. 1994, 1997; Tashiro et al. 1995; Takahashi et al. 1996a; Giommi et al. 1998; Guainazzi et al. 1999, Fossati et al. 2000b) and a gradual steepening with energy agrees with the "synchrotron self Compton" scenario, which has often been used to explain the spectral energy distribution of BL Lac objects (Ghisellini, Maraschi & Treves 1985, Ghisellini 1989). Therefore, a simple power law model is an unreliable extrapolation from X-rays to the EUV.

In order to verify this assumption for MRK 421 , we re analyze, as an example, one of the many one-hour-long 1995 *ASCA* observations (the one on 25-26 April) undertaken simultaneously with the *EUVE* observation (1995 'flare'). This in order to investigate the spectral slope below 1.5 keV (Takahashi et al. 1996b and 1999 only published data for 1.5 keV and above). First we fitted the *ASCA* spectra with an absorbed broken power law and the best fit requires a break position at $E_{break} = 1.77 \pm 0.07$ keV and the energy slopes varies from 1.44 ± 0.16 above the break to 0.98 ± 0.02 below the break (consistent with what found by Takahashi et al.). The broken power law model however does not give a good fit of the spectrum below 1.5 keV; a better result is

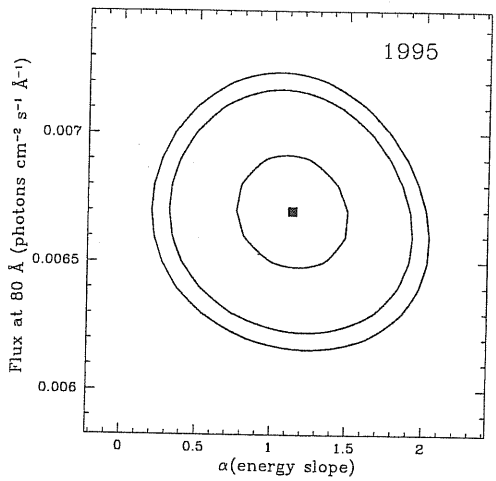

Figure 12.5: Same as Fig. 12.2 for the 1995 spectrum and the power law model.

found if we assume a "curved spectrum" parametrized as

$$F(E) = E^{-(f(E)\alpha_{low}+(1-f(E))\alpha_{high})}$$

where $f(E) = (1-exp(-E/E_0))^{\beta}$, α_{low} and α_{high} are the low and high energy asymptotic slopes and β is the curvature radius in the energy space. The best fit values for the curved model with fixed $\beta = 1.0$ (e.g. Guainazzi et al. 1999) are $\alpha_{low} = 0.57 \pm 0.06$, $\alpha_{high} = 1.34 \pm 0.13$ and $E_0 = 1.78 \pm 0.18$ (see Fig 12.8); these values show that the slope flattens toward lower energies and that an extrapolation with a simple power law is not an accurate way to predict the EUV continuum level; the low energy asymptotic slope ($\alpha_{low} = 0.57$) is generally in agreement with the flat slope derived from the EUV spectrum ($\alpha = 0.71 \pm 0.61$ from Tab. ??).

Note that in the case of PKS 2155-304 there is an additional problem: the *ROSAT* spectral slope used for the extrapolation was not measured simultaneously to the EUV spectrum and the spectral slope has been observed to harden when the source intensity increases (Giommi et al. 1998).

12.4 1996 energy spectrum

In 1996 MRK 421 was again observed $\sim 0.3°$ off-axis with a total effective exposure of 354806 s. The 1 Å binned spectrum and the best fit parameters model are plotted in Figure 12.9; the corresponding contour confidence levels are shown in Figure 12.10.

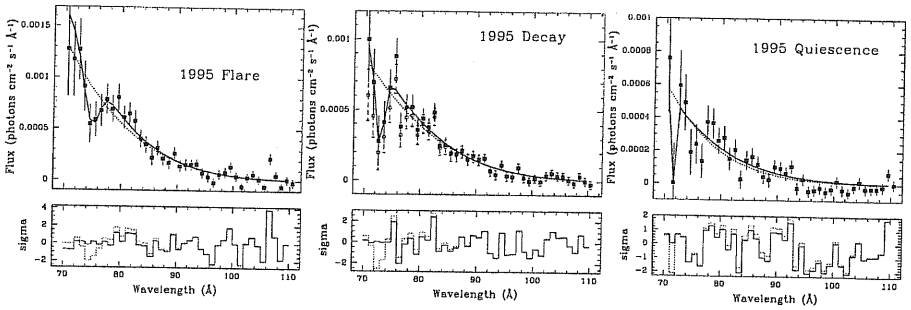

Figure 12.6: Individual sections of the 1995 spectrum of MRK 421 (left) During the flare (MJD 49832-49835 or Apr. 25-28); (center) during April 29 - May 6(MJD 49835-49843) for direct comparison with the analysis by Kartje et al. 1997; (right) during the remaining period, May 7-13 (MJD 49844-49851). The best fit power law model (dotted line) and the best fit power law + inverted gaussian model (solid line) are shown. The open circles in the central figure correspond to the spectrum corrected with the on-axis effective area (not accurate for this off-axis observation) as presented in Kartje et al. 1997.

12.5 The EUV absorption feature

We performed several fits using an absorbed power law model plus gaussian for all the observations. The results are listed in Table 12.2. In every case, except for the 1994 observation, the addition of a gaussian absorption line improves the fit. The power law slope is in the range $\alpha = [-0.15, 1.62]$ which is not too distant from the slope measured from X-ray data, (see e.g. Guainazzi et al. with SAX data which gives $\alpha = 0.3 - 1.1$ depending on the spectral model and by Fossati et al. 2000a $\alpha 0.78 - 1.21$ around 0.5 keV). The best-fit center of the gaussian absorption lines is in the 71-75 Å range with full width half maximum varying from 0.2 to 6 Å. We note however that the 6 Å FWHM is relative to the global 1995 observation and it is probably due to the super-position of narrower slightly variable lines.

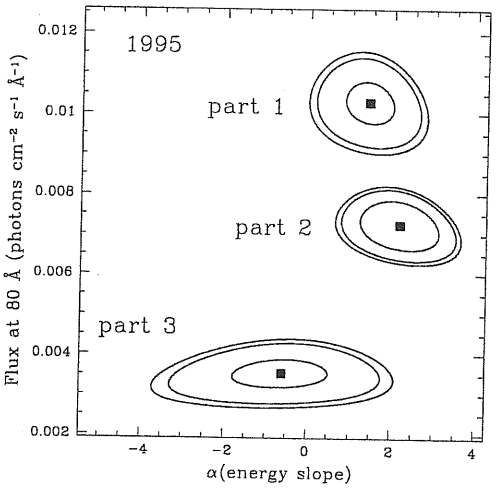

Figure 12.7: Same as in Fig. 12.2 for the three sections of the 1995 observation and the power law model. They are displayed, from the top to the bottom, in temporal order: part 1 corresponds to the flare, part 2 to the decay and part 3 to the quiescent period.

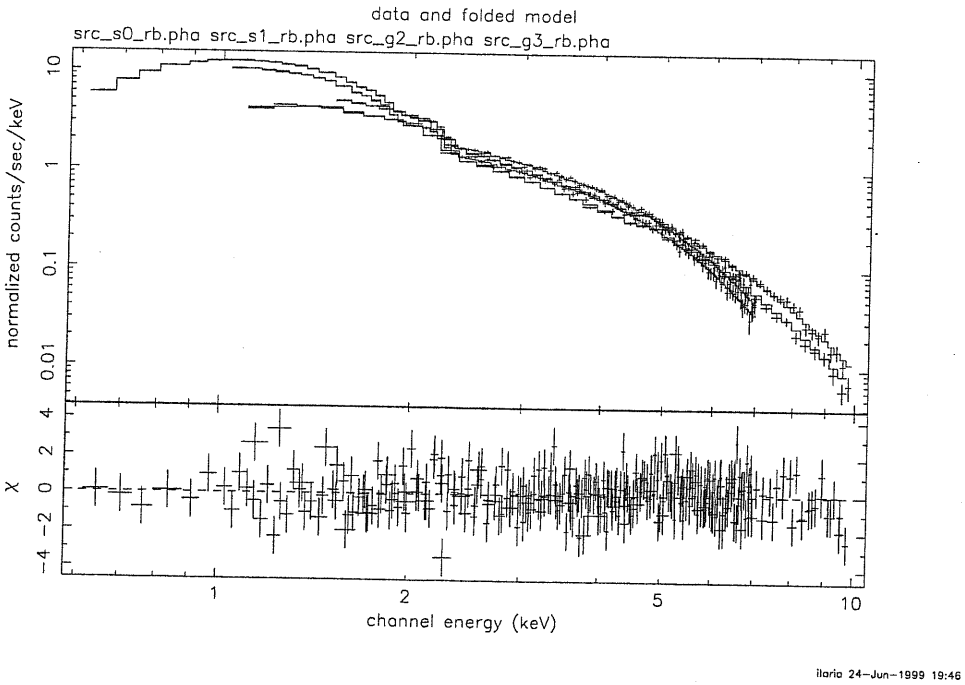

Figure 12.8: *ASCA* spectrum of MRK 421 obtained in 1995 during the flare. The solid lines represent the best-fit model when an absorbed power-law with a gradually changing spectral index is applied to the spectrum of all the instruments simultaneously (upper panel). The lower panel shows the residuals.

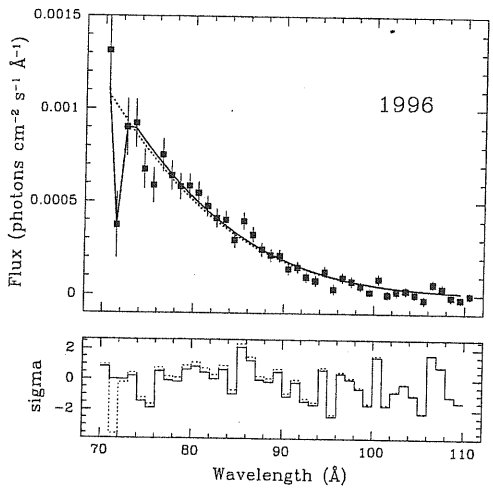

Figure 12.9: EUV spectrum of MRK 421 obtained in 1996 with the SW spectrometer during a 0.3° off-axis observation. The best fit power law model (dotted line) and the best fit power law + inverted gaussian model (solid line) are shown.

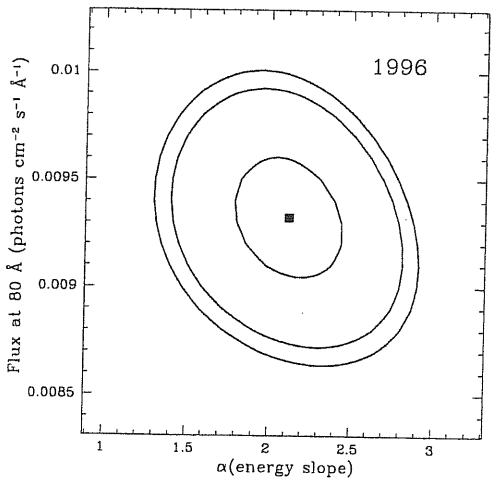

Figure 12.10: Same as Fig. 12.2 for the 1996 spectrum and the power law model.

Table 12.2: Spectral fits to the EUV spectrum of MRK 421 assuming an absorbed power law model plus a reverted gaussian. Fixed parameters as in Table 12.1

Obs.		Power Law		Gaussian				
		α	$f_{80\mathring{A}}$ $(10^{-3}\frac{phot}{cm^2 s \mathring{A}})$	λ_0 (Å)	FWHM (Å)	Ampl. $(10^{-3}\frac{phot}{cm^2 s \mathring{A}})$	χ^2_ν	F
1994		-0.29 ± 0.83	6.72 ± 0.35	$79.3^{+1.05}_{-0.07}$	0.20 ± 0.05	-10.67 ± 0.95	1.14	
1995		1.14 ± 0.41	7.55 ± 0.22	73.5 ± 0.84	6.07 ± 1.47	-2.23 ± 0.48	1.17	
Flare	Apr. 25-28	0.71 ± 0.61	11.6 ± 0.52	74.87 ± 0.45	3.04 ± 0.95	-5.86 ± 0.14	0.57	
Decay	Apr. 29-May 6	1.62 ± 0.59	7.84 ± 0.34	72.75 ± 0.28	1.86 ± 0.51	-5.22 ± 1.30	1.17	
Quiescence	May 7-13	0.63 ± 1.29	3.90 ± 0.35	71.43 ± 0.04	$0.17^{+0.23}_{-0.06}$	-6.55 ± 3.17	1.29	
1996		-0.15 ± 0.38	9.64 ± 0.28	$71.82^{+0.06}_{-0.60}$	0.66 ± 0.12	-10.40 ± 2.75	1.10	

[a] This is calculated in the 75 – 110 Å range for the model in Table 12.1

Chapter 13

Discussion on the spectral analysis

Ever since *Einstein* Pioneering observations suggested the existence of an ubiquitous absorption feature around ~ 0.55 keV in the X-ray spectra of BL Lacertae objects (Canizares & Kruper 1984, Madejski et al. 1991), much X-ray and EUV data has been collected with the goal of confirming the existence of such absorption features.

13.1 EUV/X-ray absorption in other BL Lac objects

The first object to show evidence of an X-ray absorption feature was PKS 2155-304 ($z = 0.117$) in a 1980 *Einstein* grating spectrum (Canizares & Kruper 1984). The feature was detected at ~ 0.6 keV ($\lambda = 21$ Å) and extended for 50-100 eV ($\lambda = 120 - 250$ Å); it was interpreted by the authors as O VIII Lyα absorbed by high velocity material. Looking at a 1979 *Einstein* solid state spectrometer observation of the same object Madejski et al. 1991 found evidence for absorption at ~ 0.55 keV, consistent with the grating result.
Krolik et al. 1985 modeled the absorption as due to an out-flowing sub-relativistic wind beamed in our direction.
PKS 2155-304 was subsequently observed by *BBXRT* in 1990 and the absorption feature at ~ 0.55 keV was confirmed in those data (Madejski et al. 1994), although instrumental effects cast some doubt on this result (Sambruna et al. 1997, Weaver et al. 1995) and indeed the absorption feature was not revealed in a subsequent *ROSAT* observation (Brinkmann et al. 1994).

In a long exposure (> 100 ks) *Beppo-SAX* spectrum of PKS 2155-304 in the soft X-rays (Giommi et al. 1998) the best fit model is improved (at 99% confidence) when a notch at 0.55 ± 0.04 keV is added to the model, although the magnitude of the feature is close to the instrument calibration limits.
PKS 2155-304 was also observed by *EUVE*. A 1992 30 ks observation gives hints of an absorption feature at $\sim$ 80 Å (Fruscione et al. 1994). Two longer observations in June (130 ks) and in July (150 ks) 1993 suggested the existence of 2 to 5 absorption features at a $\geq 3\sigma$ level in the range 75 to 110 Å (Konigl et al. 1995). Extrapolating the *ROSAT* X-ray spectral slope into the EUV the authors found evidence of a wide absorption feature from $\sim$ 75 to $\sim$ 85 Å and interpreted it as the superposition of Doppler-smeared absorption lines (L-shell transitions of Mg and Ne as well as M-shell transitions of Fe) that originate in a high-velocity clumped outflow from the nucleus. According to this model the X-ray line spectrum should be dominated by an O VII Kα broadened and blueshifted feature. This corresponds to the feature observed in by *Einstein* and in 1990 by *BBXRT*, but the predictions are an order of magnitude greater than the observations; to match *BBXRT* measurement the oxygen must be present in sub-cosmic abundance (Konigl et al. 1995).

Another BL Lac object to show an X-ray absorption feature is H1426+428 ($z = 0.129$). Sambruna et al. (1997) re-analyzed a *BBXRT* 1990 observation and found a broad feature around $0.5 - 0.6$ keV confirmed by an *ASCA* 1994 spectrum, but not by a *ROSAT* 1993 spectrum.

A third BL Lac, PKS 0548-322 ($z = 0.069$) (Sambruna & Mushotzky, 1998) confirmed the early discovery of an absorption feature from the *Einstein* spectrum (Madejski et al. 1991); this feature is present in *ASCA* data and can be modeled with either an edge at $\sim$ 0.66 keV and optical depth $\tau \sim 0.3$ or with a notch at $\sim$ 0.82 keV and fixed width of $\Delta E = 0.1$ keV and covering fraction $f_c \sim 0.1$. The *ASCA* absorption feature is at energies significantly higher than in previous X-ray observations, when the continuum was in a slightly higher state (by a factor $\sim$ 1.4); this provides tentative evidence for variability in the absorption feature.

The situation in the X-ray regime is still confused because all the absorption lines revealed so far fall in a critical region of the spectrum for calibration purposes. In fact, the k-edges of C, N e O, the constituents of the windows supports of all the instruments launched so

far, fall in the $\sim 0.2 - 0.6$ keV range and the effective area in these region is discontinuous. Even the smallest uncertainties ($\sim$ 1%–2%) in the knowledge of the instrumental response around this energy can induce significant spurious features (e.g. Fossati & Haardt 1997).

13.2 EUV/X-ray absorption in Markarian 421

Kartje et al. (1997) interpret the absorption feature in the context of the Konigl et al. (1995) model for PKS 2155-304 as a superposition of Mg VIII and Mg IX absorption lines. The implied ionization state of the gas would require stronger O VII absorption in the X-ray range than is allowed by observations and the authors invoke subcosmic oxygen abundance to explain its absence.

Our analysis of the 1994, 1995 and 1996 *EUVE* spectra of MRK 421 shows an absorption feature inferred directly from the *EUVE* data, (i.e. by modeling the EUV continuum and the absorption line simultaneously). The simplest model for this feature is a reverted Gaussian at about 71-75 Å a maximum FWHM of the order of few Å.

In order to investigate likely absorption features in a BL Lac environment, we ran photoionization equilibrium models (Nicastro et al. 1999, Nicastro et al. 2000) which include the strongest 300 emission and resonant absorption lines down to 50 eV (oscillator strength > 0.1). We find that the predicted wavelengths and strengths of the absorption lines, both absolute and relative, are highly sensitive to the properties of the photoionizing continuum and the absorbing gas (e.g. the ionization state and the assumed outflowing velocity). The number of transitions in the model also has a strong effect. However assuming the observed EUV-to-X-ray continuum and adjusting the gas parameters to maximize the relative abundance of OVII ($\sim$ 65%) both an OVII Kα absorption line (EW=0.25Å) and a FeIX L ($\lambda_{\rm rest}$ = 82.43 Å, EW=0.2Å) absorption line are expected respectively around 0.6 keV and 73 Å (assuming an outflow velocity of 0.15c). The equivalent width of the lines is too small to give significant detections, however, especially in the EUV regime, the presence of many fainter satellite lines (not included in the model) could explain the observed feature For example between the Si VI line (λ = 72.34 Å) and the Mg VI complex (λ 71.3 Å), both included in the model, at least 15 additional lines from ionized Fe, Al, Be and Ne are not included (oscillator strength 0.01-0.1) and could be important especially if the elements are abun-

dant.

In order to investigate any possible correlation between spectral changes and source flux, we plotted in Figure 13.1 the energy index as a function of total EUV flux for the the power law plus gaussian models. However the large error bars prevent any statistically significant conclusion.

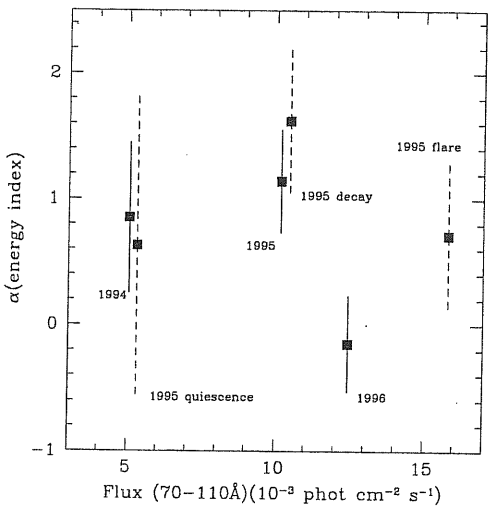

Figure 13.1: EUV source flux vs. energy index (α) for the power law component of the power law plus gaussian model.

In the X-ray regime, no absorption line was ever detected for MRK 421 before the spectral resolution of *Chandra* was available. MRK 421 was observed with the *Chandra* ACIS-HETG configuration twice, on November 5, 1999 and on May 29, 2000 and for the first time the spectrum was observed with a resolution of R=400 at 20 Å (corresponding to $\Delta\lambda = 0.05$ Å). The results of the analysis of the first order *Medium Energy Grating* (MEG) data is presented in Nicastro et al. 2001. The 1999 spectrum shows the presence relatively broad emission and absorption lines (significativity 2σ per bin, spread over various bins), tentatively identified with two different absorbing/emitting systems of ionized gas with oxygen mostly distributed between O VII and O IX species. These two systems are outflowing from the central source with velocities of 6600 and 28500 km s^{-1} respectively. During the 2000 observation MRK 421 is an order of magnitude brighter than in 1999 and no absorption or emission lines are present in its spectrum. The disappearing of the absorbing/emitting systems suggests that they were intrinsic to the nuclear environment and became fully ionized, and so transparent, as the source brightened. No features were found in a

Newton-XMM observation (Brinkmann et al. 2001).

13.3 Conclusions

Even though our initial goal was to disprove the existence of EUV absorption in the spectrum of MRK 421, we have found a clear absorption feature at $\sim 71-75$ Å. All the evidences for absorption in the X-ray spectra of BL Lacs are in the ~ 0.5 keV region, where even small calibration uncertainties of the discontinuous effective area can bring to spurious features, but we cannot explain in the same way the absorption feature we found in the EUV band. Two absorbing/emitting systems were recently seen by *Chandra* in the range 19-22 Å (0.56 - 0.65 keV) (Nicastro et al. 2001). These systems are visible in a faint status of the source, while they disappear when the source brightens. These features are not visible in the *XMM-Newton* spectrum (Brinkmann et al. 2001)

The absorption features detected by different instruments on different satellites in the X-ray spectra of BL Lac objects fall in the same $\sim 0.5-0.6$ keV band and could be explained with uncertainties in the calibrations in this critical energy range, but all these uncertainties would be for all the instruments and all the satellites systematically underestimating the number of photons around ~ 0.5 keV; no claims of emission lines in BL Lacs were in fact ever reported. And we cannot explain the EUV absorption feature we found in the spectrum of MRK 421 with the same calibrational problems.

Future observations covering the EUV to X-ray energy bands with much higher resolution and collecting area, as with *Chandra* and *XMM-Newton* are needed to confirm or disprove the presence of absorption lines in the X-ray and EUV spectra of BL Lacertae objects.

Chapter 14

Timing analysis

14.1 Light curves

We extracted the light curves from the DS or Scanner time-ordered event lists using the *EUVE* Guest Observer Center software (IRAF/EUV package) and other IRAF timing tasks adapted for *EUVE* data. All the lightcurves were binned over one average *EUVE* orbit (5544 s), but effective exposure times per bin vary due to several correction factors different case by case (e.g. instrumental deadtime, telemetry saturation, high particle background, dead spot).

Unless described otherwise, we chose the extraction region for the source as a circle with a $2.5'$ radius excluding a circle with a $0.67'$ radius centered on the serendipitous source. The background region is an annulus with inner and outer radii equal to $\sim 4'$ and $8'$ respectively which avoids the other serendipitous source.

In order to compare scanner and DS data, we had to normalize the count rates. Count rates depend on the effective area of the telescope and on the spectral shape of the source. We convolved a sample of input spectra (absorbed power law with slopes as in Table 12.1) with the DS and scanner effective areas and defined the normalization factor as the ratio of peak of the derived count rates (see Figure 14.1 as an example for $\alpha = 2$). The average normalization factor is about 1.4 ± 0.3 (depending on the input spectrum). We used this value throughout the thesis and verified that the results in the power spectrum analysis are all consistent within the errors of this value.

The combined light curve of all the observations is presented in Figure 14.2.

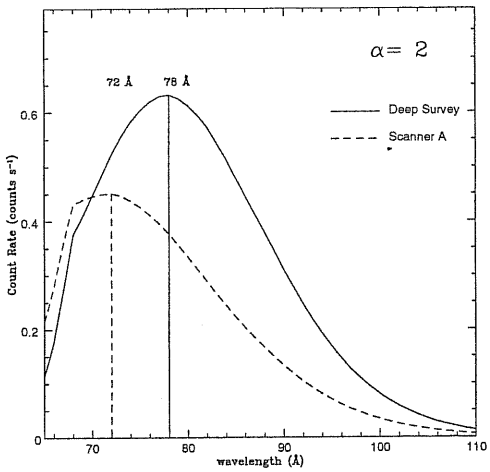

Figure 14.1: Simulated count rates in the DS (solid line) and Scanner A (dashed line) instruments assuming an absorbed power law model with spectral index $\alpha = 2$ The ratio of the count rate at the peak wavelength for the two instruments was used as rescaling factor to convert the Scanner A count rate into a DS count rate.

In this section we will give a qualitative description of each lightcurve in terms of flares and sub-flares: a general rising/decreasing trend will be addressed as a "flare", while faster variations superimposed on the general trend will be referred to as sub-flares. This description is useful in understanding the results from the power spectrum and structure function analysis.

14.1.1 1994 DS light curve

Figure 14.3 shows the 1994 light curve, which was obtained eliminating time intervals when the source crossed the dead spot [1] (about 1440 s).

The source dimmed for about 3 days, brightened again for another $\sim$ 3.5 days, until it reached a level of $\sim$ 0.2 counts/sec and stayed there for the remaining of the observation (another $\sim$ 3.5 days). This light curve behavior could be sampling the end of a flare and the beginning of a new one. Interestingly, when the source increases its flux, after MJD 49447, (i.e. possibly during the beginning of a new flare) smaller "sub-flares" are superimposed on it; this trend is also present in the 1995 scanner lightcurve (see 2.2.2 and Figure 14.4).

[1] A small region of reduced gain and detector quantum efficiency near the center of the DS detector, caused by the observation of the very bright EUV source HZ 43 (Sirk 1994)

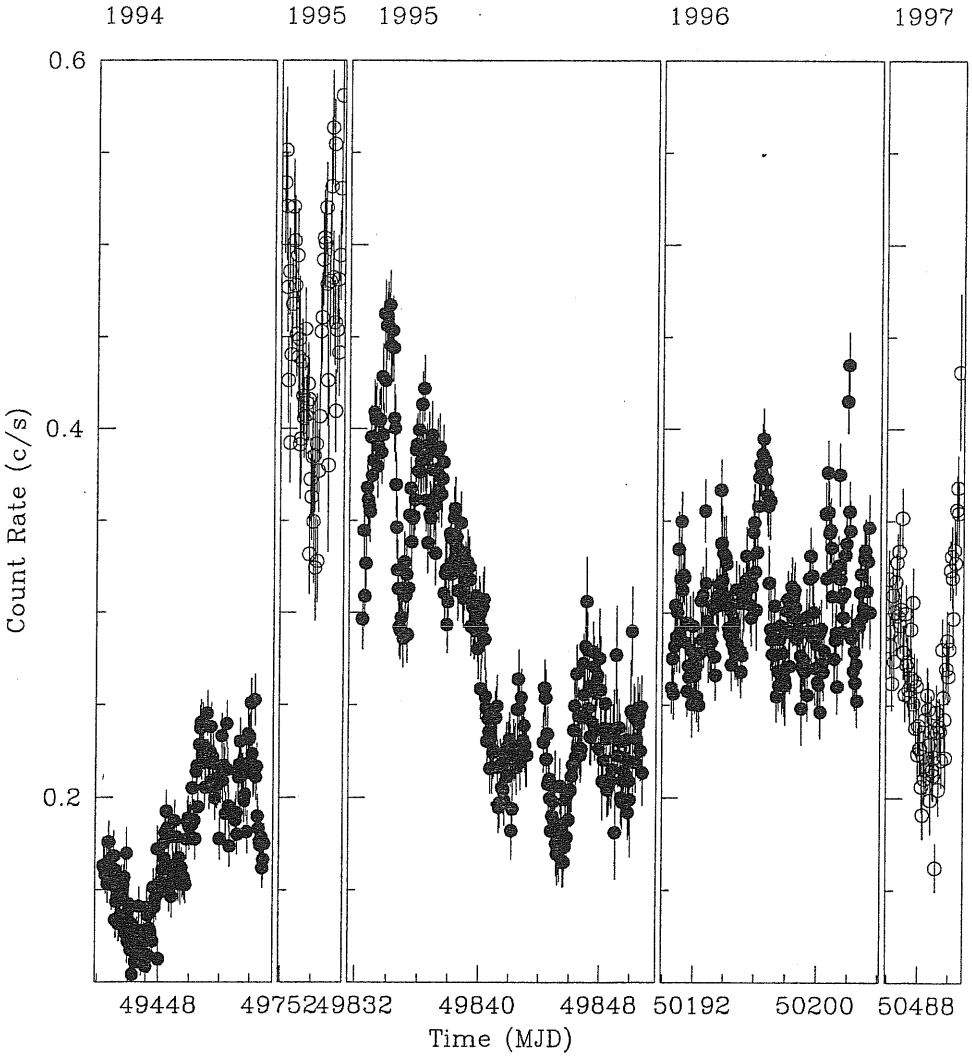

Figure 14.2: Combined lightcurve of all *EUVE* observations from 1994 to 1997 binned over one average *EUVE* orbit (~ 5544 s).

14.1.2 1995 scanner A light curve

During this scanner exposure optimized for the primary scientific DS/S observation of HD 41511, MRK 421 partially falls in the region usually discarded by the standard analysis pipeline because of the obscuration due to the filter support and because of the high particle background close to the detector edge. We extracted the lightcurve only from the "clean" region of the detector and we corrected the count rate for the fraction of the count lost (~10%). The background region was chosen in the same detector quadrant as the source and large enough to match the ratio background/source (~ 7.8) region used for the other lightcurves. The lightcurve is plotted in Figure 14.4; the open

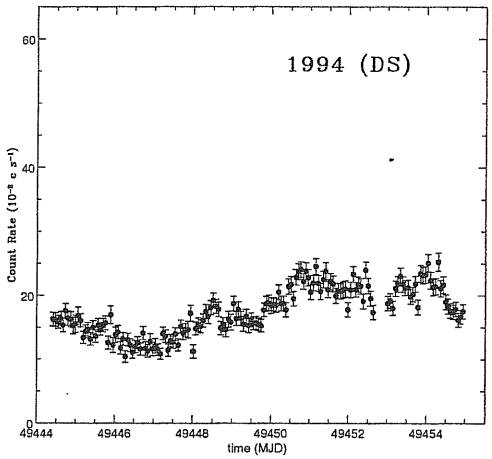

Figure 14.3: April 2-12 1994 Deep Survey lightcurve binned over one average *EUVE* orbit (~ 5544 s). This light curve was also presented in Fruscione et al. (1996).

circles represent the count rate measured in scanner A, while the filled circles are the count rate normalized to the DS; this lightcurve has as behavior similar to the 1994 DS lightcurve: when the source brightens, after MJD 49754, "sub-flares" appear above the main trend.

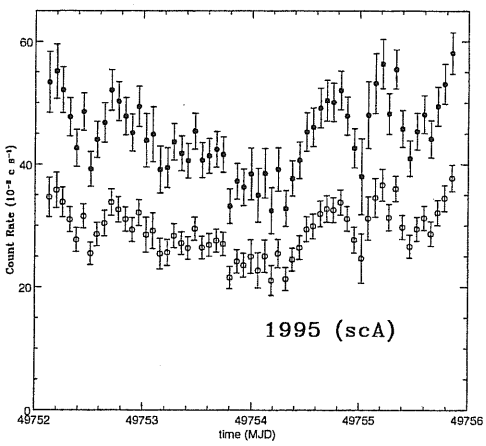

Figure 14.4: February 4-7 1995 Scanner A light curve (open circles) binned over one average *EUVE* orbit (~ 5544 s). The filled circles represent the count rate scaled to the DS instrument (see Section ??).

14.1.3 1995 DS light curve

During this DS/S observation, the source was pointed 0.3° off axis both to avoid the dead spot and to extend the spectrum toward shorter wavelengths (see paper I). The light curve is shown in Figure 14.5.

The behavior of the source during the DS 1995 observation is complex: at the beginning MRK 421 brightens by a factor of $\sim$ 65% in less than 2 days and this flare, which lasts for about 3 days, is well correlated to a TeV/X-Ray flare (Buckley et al. 1996). Right after the first one, there is a second flare lasting for $\sim$ 6 days which can also be seen as the superposition of two separate flares (the second one starting at $\sim$ MJD 49838). After MJD 49845.5, the source rises from $\sim$ 0.20 counts s^{-1}, up to $\sim$ 0.28 counts s^{-1}, and then decays to $\sim$ 0.23 counts s^{-1}, within $\sim$ 3 days. The overall variability of the source is about a factor 3.

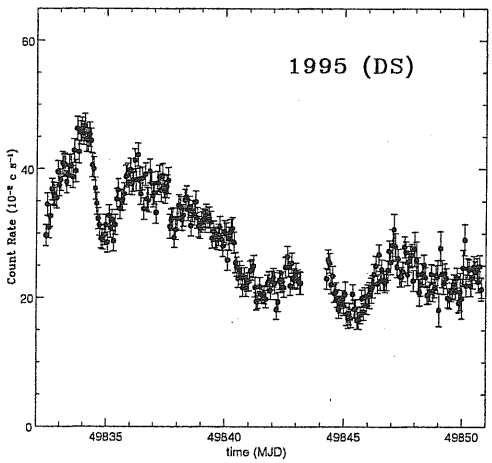

Figure 14.5: Same as Figure 14.3 for the April 25 - May 13 1995 DS data. The data from MJD 49832 to MJD 49843 were presented in Kartje et al. (1997) and were part of a multiwavelength campaign during which a TeV flare was detected (Buckley et al. 1996).

14.1.4 1996 DS light curves

In 1996 MRK 421 was observed few days before and few days after the detection of a large TeV flare on May 7th 1996 (Zweerink et al. 1997). The lightcurves are shown in Figure 14.6. This lightcurve looks different from all the other ones because no slow variations seem to be present; the source appears to be at a constant level with lots of small amplitude, fast variations superimposed on it; i.e., the light curve appears to be the sum of flares which live a short time, and rise or decay faster when compared with the flares seen in the other light curves (see for example the two flare like events after MJD=50200).

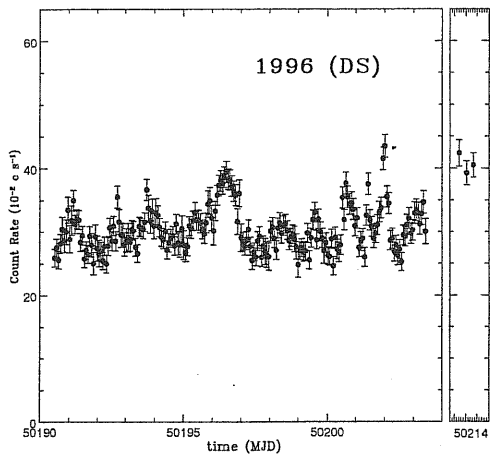

Figure 14.6: Same as Figure 14.3 for the April 17-30 DS data (on the left) and the May 10-11 data (on the right). A large TeV flare (Zweerink et al. 1997) occurred on 7 May 1996.

14.1.5 1997 scanner A light curve

In 1997 MRK 421 was observed for 4 days with the scanner A telescope during the DS pointed observation of Γ Tauri; the source was detected within the useful area of the scanner A field of view allowing an easier data reduction than the previous scanner observation. The light curve is shown in Figure 14.7: the open circles represent the scanner data while the filled circles correspond to the count rate normalized to the DS. This is the shortest lightcurve and its shape suggests that we may be looking at the tail of a flare and at the beginning of a new one.

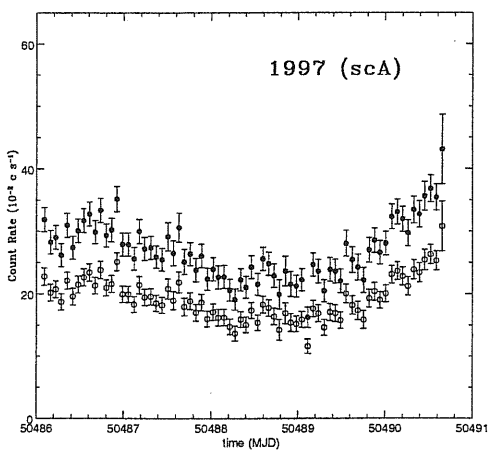

Figure 14.7: Same as Figure 14.4 for the February 7-11 1997 Scanner A data.

14.2 Power Spectrum Analysis

In order to quantify the variability seen in the *EUVE* lightcurves of MRK 421 , we computed their periodogram as:

$$\hat{I}(\nu_i) = \frac{\Delta t}{N}\{\sum_{i=1}^{N}[x(t_i) - \bar{x}]e^{-i2\pi\nu_i t_i}\}^2 - C, \qquad (14.1)$$

where: $\bar{x}$, Δt and N are the mean value, bin size and number points of each light curve respectively, and $\nu_i = i/(N\Delta t)$, $i = 1, 2, ..., (N/2) - 1$ (e.g. Deeming 1975). The constant C in equation (1) represents the power level due to Poisson statistics, $C = \Delta t \sigma^2_{noise} = (\Delta t/N)\sum_{i=1}^{N} err(i)^2$ ($err(i)$ is the error of each light curve point). The subtraction of this constant level is necessary since we are interested in the source power spectrum only and the *EUVE* light curves were obtained with two different instruments, hence the Poisson statistics will be different in them. The periodogram calculated in this way has the units of (counts/sec)^2/Hz, and its integral over positive frequencies is equal to half the light curve variance.

It is common to average the periodogram estimates in order to reduce the variance and approximate their probability distribution function to a Gaussian. Furthermore, it is better to estimate the logarithm of the power spectrum instead of the power spectrum itself, since the logarithmic transformation brings the distribution function of the power spectrum estimates closer to a Gaussian (Papadakis & Lawrence, 1993). Therefore, we calculated the logarithm of the binned periodogram estimates,

$$\log_{10}[\hat{P}(\nu_i)] = \log_{10}[\frac{\sum_j \hat{I}(\nu_j)}{m}], \qquad (14.2)$$

(where $\nu_i = \sum_j \nu_j/m$, and $\nu_j = j/(N\Delta t)$) and used it as our estimate of the *logarithm* of the power spectrum. The index j varies over m consecutive periodogram estimates and the index i varies over the $[(N/2)-1]/m$ subsets into which we have grouped the periodogram estimates. Taking into account the propagation of errors (e.g. Bevington 1969), the error on the logarithm of the power spectrum is

$$\sigma(\log_{10}[\hat{P}(\nu_i)]) = \log_{10}(e)\sigma_{\hat{P}(\nu_i)}/\hat{P}(\nu_i), \qquad (14.3)$$

where $\sigma_{\hat{P}(\nu_i)}$ is the square root of the variance of the $\hat{I}(\nu_j)$' s around the mean value, $\hat{P}(\nu_i)$, at each bin.

14.2.1 Power spectra of the orbit-binned lightcurves

We estimated the power spectrum of the DS and scanner A light curves binned over one average *EUVE* orbit (5544 s) shown in Figures 14.2 – 14.7. To avoid the gap in 1995 DS observation (Figure 14.5) we divided it into 2 parts and performed a power spectrum analysis on each one of them. Using equations 1 and 2, we estimated the logarithm of the power spectrum with $m = 10$. A larger value for m would bring the distribution function of the power spectrum estimates closer to a Gaussian (Papadakis & Lawrence 1993). However this small value of m was necessary in order to have a reasonable frequency resolution, i.e. in order to have the maximum possible number of power spectral points above the Poisson noise level.

The power spectra of all the light curves, normalized to the square mean value of the respective light curve, are shown in Figure 14.8. The normalization is necessary if one wants to compare the power spectrum amplitudes, since the light curves were obtained from two different instruments. All the power spectra show a similar red noise behavior at frequencies $< 10^{-4.3}$Hz (i.e. all of them rise logarithmically toward lower frequencies in a similar way), except for DS 1996 observation which seems to flatten for $\nu < 10^{-5}$ Hz.

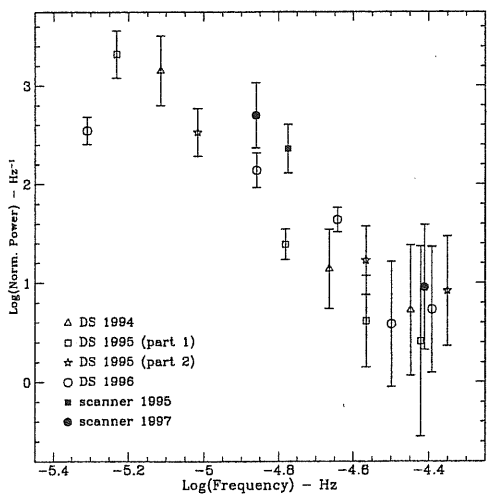

Figure 14.8: Normalized power spectrum (binning factor $m = 10$, see § 14.2.1) obtained from each lightcurve binned over 5544s (1 average *EUVE* orbit). 1995 DS/S observation was split into two parts to avoid the gap. The open symbols represent DS/S observations (triangles for 1994, squares for the first part of 1995, stars for the second part of 1995 and circles for 1996) while the filled symbols represent scanner observations (squares for 1995 and circles for 1997).

Table 14.1: Power spectra "power law" model fits for the DS orbit-binned light curves of MRK 421

Year	Instrument	α	A	No. of points	χ^2
1994	DS	4.02 ± 1.42	13 ± 24^a	3	0.38
1995 (part 1)	DS	4.14 ± 0.86	22 ± 15^a	4	0.35
1995 (part 2)	DS	2.64 ± 1.10	15 ± 8^a	3	0.17
1996	DS	1.45 ± 0.42	13 ± 6^a	5	3.85
All	DS+scaA	2.14 ± 0.28	148 ± 33^b	10	5.6

[a] in units of (counts/sec)^2/Hz
[b] in units of Hz^{-1}

We fitted the DS power spectra with a simple power law model of the form $P(\nu) = A \times (10^{-5}\nu)^{-\alpha}$ (the scanner A power spectra had too few points to fit a model to them). In this model, the normalization A is equal to the value of $P(\nu)$ at $\nu = 10^{-5}$ Hz. The model fit was done using the power spectra before normalizing to the mean square value. The best model fit results are listed in Table 14.1. The model gives a good fit to all the DS power spectra, but, due to the small number of points, the errors on the model parameters are large. The best fit values of A are within the errors for all the DS spectra. However, the best fit slope values show a larger scatter. In particular, the difference between the DS 1995 (part 1) and the DS 1996 best fit slope values is 2.7 ± 1.0. This $\sim 3\sigma$ difference indicates that the shape of the power spectrum does not remain constant with time, i.e. that the EUV emission of MRK 421 is not stationary [2]. However, looking at DS 1996 power spectrum (Figure 14.8), there is a possibility that the flatter slope obtained from the fit is due to a flattening around $\nu = 10^{-5}$ Hz. If this is the case, a broken power law model should give a better fit to the data. However, with just 5 points, it is not possible to investigate if a broken power improves the fit to the data in a statistically significant way (e.g. by the use of an F-test). On the other hand, perhaps the flattening of the power spectrum is a spurious effect introduced by the small binning used ($m = 10$).

In an attempt of ruling out this possibility we used a larger value ($m = 20$). Figure14.9 compares the results: open circles for Structure Function of the total *EUVE* light curve of MRK 421 . (Figure 14.2)

[2] A lightcurve is said to be stationary if its mean, variance and power spectrum remain constant in time (e.g. Chatfield 1989); see Section 14.2.1 for further details

Filled circles correspond to the SF estimated with a lag bin of size 1 day and the filled squares to the SF estimated with a lag bin of size 1 month. Open symbols (circles and squares) correspond to the mean SF of 1000 simulated light curves with a power spectrum of slope 2.14 and a frequency turnover at 4×10^{-6} Hz. Dotted triangles correspond to the mean SF of 1000 simulated light curves with a same slope power spectrum but with a frequency turnover at 10^{-7} Hz. In both cases, the errorbars correspond to the standard deviation of the simulated SFs around their mean (see § 14.3 details). $m = 10$ (as in Figure 14.8) and filled circles for $m = 20$. Both power spectra look similar, and the lack of frequency resolution in the latter case cannot allow us to reach a firm conclusion.

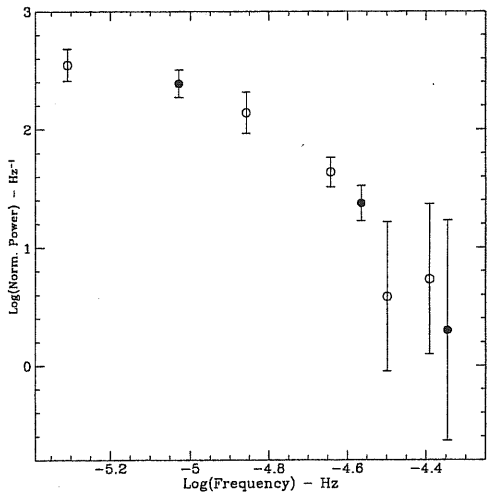

Figure 14.9: Same as Figure 14.8 for DS 1996 observation with different binnings. Opens circles, as in Figure 14.8, represent a binning value of $m = 10$, and filled circles $m = 20$ (see § 14.2.1).

Despite this possible non-stationarity, it is useful to combine the periodograms of all the DS and scanner A light curves in order to increase the number of power spectrum estimates (and hence the frequency resolution). We first normalized the data sets to the square mean value of the respective light curve and then combined them into one dataset by sorting them in order of increasing frequency. Then we grouped this "combined" periodogram into bins of size $m = 20$ since the larger number of estimates allows us to use a larger bin size value. Figure 14.10 shows a plot of the resulting power spectrum (filled circles). Note that the combined power spectrum has the units of Hz^{-1}. This spectrum can be considered as the "average" EUVE power spectrum

of the source. A power law model gives a good fit to this average power spectrum (solid line in Figure 14.10; Table 14.1) with a best fit slope value of 2.14 ± 0.28.

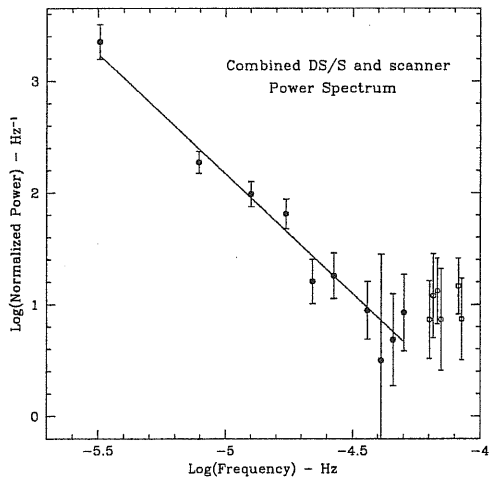

Figure 14.10: Average normalized power spectrum of MRK 421 obtained from all the 5544s binned lightcurves presented in Figure 14.2 (see § 14.2.1). Different symbols represent different binnings: $m = 20$ (filled circles) for the low frequency part and $m = 10$ (open circles) for the high frequency part representing the the Poisson noise level. The solid line shows the best power law model fit with slope -2.14.

14.2.2 Power spectra of the 500 s binned lightcurves

Due to the indication of a possible break in the power spectrum and/or a possible non-stationarity in the *EUVE* light curve of MRK 421, we decided to investigate further the power spectra of the DS 1995 and 1996 light curves. Our main aim was to determine the high frequency shape of the power spectrum as well as possible. For this reason, we used a ~ 10 times finer binning, with a bin size of 500 s, for the light curves; we were thus able to extend the power spectrum to higher frequencies and to use a larger value for m ($m = 20$ in equation 2) to bring the distribution function of the power spectrum estimates closer to a Gaussian.

Figure 14.11 shows the DS 1995 and 1996 power spectra estimated with equation (1), without subtracting the expected Poisson noise level, and binned as in equation (2) with $m = 20$; the long dashed lines in these plots indicate the Poisson noise power level C. Both power spectra show a large peak at $\sim 1.8 \times 10^{-4}$ Hz corresponding to a period of 5556 s, i.e. the *EUVE* orbital period. The next strongest peak is

at a harmonic of that frequency. These peaks are due to the uneven sampling of the 500 s binned light curves.

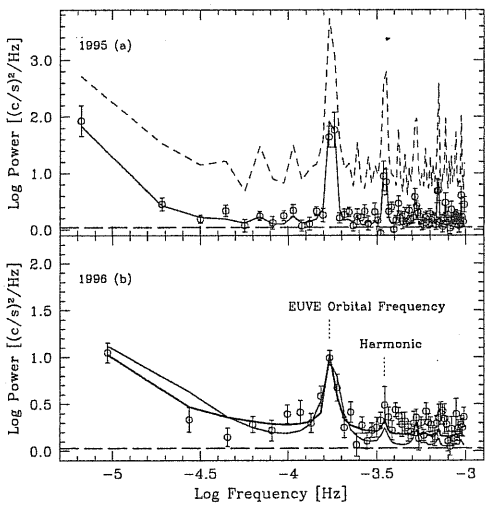

Figure 14.11: Power spectra of the DS 1995 (a) and DS 1996 (b) light curves binned over 500 s (open circles). The long dashed line in both plots indicate the expected Poisson noise power level. Solid line shows the best fit of the model defined by equation 5 in § 14.2.2, with the slope fixed to -2.14. The dotted line in (a) represents the simulated power spectrum using the same best fit values but moving the break to 10^{-7} Hz; while the dotted line in (b) shows the best fit of the same model but with the slope left as a free variable (see text).

Apart from those peaks, the two power spectra appear to have a similar shape: they rise toward low frequencies, and they are flat at higher frequencies. So, it seems as if the use of a smaller bin size in the light curves has not helped us much. The power spectra, at most frequencies, appear to be flat and dominated by the Poisson noise power. However, while the DS 1995 estimates at high frequencies are close to the expected Poisson power level, the DS 1996 power spectrum is higher than this level.

We fitted both spectra with a modified power law model with one of the slopes fixed at 2.14 (see below). Due to the effects of the window function, it is not possible to fit the logarithm of the model directly to the power spectrum calculated from the 500 sec binned light curves. Instead, we convolved the model, let us say $M(\nu)$, with the window function at each frequency ν_i,

$$I_{mdl}(\nu_i) = \frac{\Delta t}{N} \int_{-\infty}^{+\infty} M(\nu) W(\nu_i - \nu) d\nu. \tag{14.4}$$

The function $I_{mdl}(\nu_i)$ takes account of the window function effects.

We call $I_{mdl}(\nu_i)$ the "convolved model".

As $M(\nu)$, we used the following function,

$$M(\nu) = \frac{A}{[(2\pi\nu)^2 + f_b^2]^\alpha} + C, \qquad (14.5)$$

which has a power law form with a slope of 2α at frequencies $>> f_b/2\pi$, and flattens to zero slope at frequencies $<< f_b/2\pi$ (as before, C represents the power level due to the Poisson counting statistics). Note that as $M(\nu)$ we did not use a simple power law model because in this case it is not easy to estimate the convolution model (equation 4) analytically (a simple power law model cannot be defined at $\nu = 0$) and because there might indeed be a break, as suggested by DS 1996 power spectrum (Figure 14.8).

Then, we averaged the convolved model $I_{mdl}(\nu_p)$ over groups of size $m = 20$ exactly as we did when estimating the power spectrum. The logarithm of the convolved model power spectrum becomes:

$$\log_{10}[P_{mdl}(\nu_i)] = \log_{10}[\frac{\sum_j I_{mdl}(\nu_j)}{m}]. \qquad (14.6)$$

We can now fit $\log_{10}[P_{mdl}(\nu_i)]$ to the estimated power spectrum, $\log_{10}[\hat{P}(\nu_i)]$. In this way, we are taking into account both the window function and any effect that the binning procedure may have on the power spectrum estimation.

For the fit we used standard χ^2 statistics, we kept 2α fixed to the value 2.14, and we did not allow C to vary but rather used the value found as described at the beginning of § 14.2. Table 14.2 summarizes the best fit results for each observation; the errors quoted represent the 90% confidence levels assuming that A and f_b are correlated. By far the largest χ^2 value is for the DS 1996 model fit. However, it is not straightforward to judge the goodness of fit using the these χ^2 values. Due to the uneven sampling of the light curves, the periodogram estimates are no longer independent. Therefore, the errors on $\log_{10}[\hat{P}(\nu_i)]$ may be larger than those estimated (and hence the χ^2 values smaller). At the same time, depending on the amount of correlation between the $\hat{I}(\nu_i)$'s, the $\log_{10}[\hat{P}(\nu_i)]$ estimates may be correlated as well. As a result, the number of degrees of freedom may be smaller than those listed in Table 14.2.

The best model fits are also plotted in Figure 14.11 with a solid line; these plots show that the model agrees well with the DS 1995 power

Table 14.2: Power spectra "power Law plus low frequency turn over" model fit for the DS and scanner A, 500 sec binned light curves of MRK 421

Year	Instrument	Slope2α	f_b (Hz)	DoF	χ^2
1994	DS	2.14 (fixed)	$8.4^{+27}_{-7.7} \times 10^{-6}$	43	67.8
1995	ScaA	2.14 (fixed)	$5.0^{+18}_{-4.3} \times 10^{-5}$	14	28.7
1995	DS	2.14 (fixed)	$2.6^{+5.6}_{-2.0} \times 10^{-6}$	77	116.9
1996	DS	2.14 (fixed)	$7.7^{+4.3}_{-2.6} \times 10^{-5}$	53	140.4
		(1.1 ± 0.1)	$(1.6^{+10.}_{-1.5} \times 10^{-6})$	(52)	(65.5)
1997	ScaA	2.14 (fixed)	$7.7^{+17}_{-5.3} \times 10^{-5}$	17	16.7

spectrum, but not with the DS 1996 (as expected from the large χ^2 value). We fitted again the DS 1996 power spectrum with the model defined in equation (5) but we let the slope as a free parameter this time. The best fit results are listed in Table 14.2 (values in a parenthesis), and the best fit model is also plotted in Figure 14.11 (b) (dotted line). As this figure shows, the new model fit agrees better with the power spectrum. The best fit slope is now 1.1 ± 0.1 significantly smaller than the average slope of 2.14 ± 0.28. The χ^2 value is also reduced by 74.9. The ratio of the reduced χ^2 values for the two fits is 2.1 (note that this ratio does not depend on whether the errors on the power spectrum are underestimated or not). Using the number of degrees of freedom listed in Table 14.2 and the F-test, we find that the improvement on the fit when we let the slope to be a free variable is highly significant (the probability of a significantly better fit when $\alpha = 1.1$ is larger than 99.5%). The probability remains larger than 95%, even if the degree of freedoms listed in Table 14.2 are reduced by a factor of two.

Furthermore, to check for any other possible indication of non-stationarity, we performed a fit to the power spectra of all the 500 sec binned light curves (including the scanner A light curves) using the model defined in equation (5) with $2a = 2.14$. The best fit model results are listed in Table 14.2, and the best fit model, together with the power spectra, are plotted in Figure 14.12 (the dotted lines in this figure show the Poisson noise power level). This figure shows that the model gives a good fit to all the power spectra.

We conclude that all the *EUVE* power spectra of MRK 421 are consistent with a power law model with a slope of ~ 2.1. The only exception is the power spectrum of the DS 1996, which shows a significantly flat-

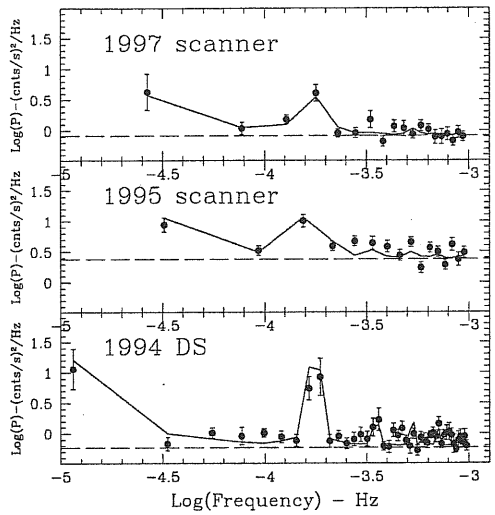

Figure 14.12: Same as Fig. 14.11 but for DS 1994, scanner A 1995 and scanner A 1997 respectively.

ter slope of 1.1 ± 0.1. The clear change in slope in the 1996 data shows that the EUV emission of MRK 421 is not statistically stationary (see § 14.2.1).

As hinted by Figure 14.8 for DS 1996 (open circles), from the fit of the 500 s binned power spectra we found indication for the presence of a low frequency turn over in the *EUVE* power spectrum of MRK 421 below which the power spectrum flattens. This finding, if confirmed, would be the first detection of a break in the power spectrum of a BL Lac object. Since we cannot estimate the power spectrum at frequencies lower than $\sim 10^{-5}$ Hz, using the value $m = 20$, we cannot be certain of the slope below the turn over frequency. All we can say with the present data is that the power spectrum should show a change in its slope at f_b. Furthermore the value of this knee frequency is not constrained very well from our data. Using the best fit results from the DS spectra only (as they have the largest number of data points), we get a straight mean value of $f_b = 4 \times 10^{-6}$ Hz. By simply combining the overlapping 90% confidence limits on the best values of f_b, we find that with probability larger than 68%, f_b should be between 7×10^{-7} Hz and 8×10^{-6} Hz.

From a physical point of view, it is natural to expect that low frequency knees should be present in the power spectra of AGN. Lack of this turnover would imply a physical system with infinite variance, a system whose properties change continuously with time. The fre-

quency turnover is not evident in the combined *EUVE* power spectrum of MRK 421 (Figure 14.10), because that spectrum does not extend to frequencies below $\sim 10^{-5.5}$ Hz. Its presence is implied only when we take proper account of the window function effects in the model fitting of the 500 s light curve power spectra. If the frequency turn over were located at a much lower frequency, more power would be transferred to higher frequencies. The resulting power spectrum would have a higher normalization than the observed one. To put in other words, the amplitude of the variations in the light curves would be larger, i.e. they should have a higher variance. For example let us assume that the source power spectrum is well describe by equation (5) and that the break is at 10^{-7} Hz. Using equations (4) and (6) we can predict how the power spectrum of the DS 1995 light curve should be in this case (dotted line in Figure 12a). As this Figure shows, the power spectrum should have a much larger amplitude than the one that is actually observed.

Due to the significance of such a feature in the power spectrum of the source, we searched further evidence of its existence by means of a structure analysis of the light curves. We present below the results from this analysis of the *EUVE* light curves which confirm the existence of this turn over in the power spectrum of MRK 421 .

14.3 Structure Function Analysis

The Structure Function (SF hereafter) is defined as,

$$SF(\tau) = 2\sigma^2 - R(\tau), \tag{14.7}$$

where σ and $R(\tau)$ are the variance and auto-covariance at lag τ of the light curve (equation A4 in Simonetti, Cordes & Heeschen, 1985). For a given light curve, it is usually estimated by,

$$\hat{SF}(\tau) = \frac{1}{N}\sum_{i=1}^{N-\tau}[x(i+\tau) - x(i)]^2, \tag{14.8}$$

(equation A8 in Simonetti, Cordes & Heeschen, 1985). The SF gives a measure of the mean difference in the flux of two light curve points, as a function of their time separation (lag) τ. There is a simple correspondence between the SF and the power spectrum: when $P(\nu) \propto \nu^{-\alpha}$

then $SF(\tau) \propto \tau^{\alpha-1}$. Furthermore, if the power spectrum flattens below a frequency f_b, then $SF(\tau) \sim 2\sigma^2$ in the limit $\tau >> 1/f_b$.

The main advantage of the structure function analysis is that the SF estimation is not affected by gaps of missing points in the light curve (it is easy to show using equation (8), that $< \hat{SF}(\tau) >= SF(\tau)$, irrespective of the light curve sampling pattern). However, it is difficult to estimate the errors on $\hat{SF}(\tau)$ because, as with estimates of other time domain quantities (e.g. auto, cross-correlations), the SF estimates at different lags are heavily correlated (much more so than the periodogram points at different frequencies, even in the case of unevenly sampled data).

To estimate the SF of MRK 421, we used together all the orbit-binned DS and scanner A light curves and constructed a single, long *EUVE* light curve of the source (in order to use the scanner data into an overall light curve, we normalized them to the DS expected count rate as explained in § 14.1). For each pair of data points in the light curve, $x(t_i)$ and $x(t_j)$, we computed their time difference, $\Delta t_{i,j} = t_i - t_j$, and their flux difference, $FD_{i,j} = x(t_i) - x(t_j)$. Let us assume that we have chosen a lag bin of size $\Delta\tau$, and that there are n points with $\Delta t_{i,j}$ in the interval $[\tau - \Delta\tau/2, \tau + \Delta\tau/2]$. We used the average value of the n FD_{ij} measurements, $\sum FD_{i,j}/n$, as an estimate of the structure function, $\hat{SF}(\tau')$, at the lag $\tau' = \sum \Delta t_{i,j}/n$.

For the overall *EUVE* light curve (Figure 14.2), we estimated the SF twice. The first time we used $\Delta\tau = 1$ day, and the second time $\Delta\tau = 1$ month. The first bin value was used to estimate the SF from lag ~ 1 day up to lag ~ 18 days. We cannot estimate the SF at higher lags with $\Delta\tau = 1$ day since the individual*EUVE* light curves of MRK 421 have a maximum length of ~ 20 days. Consequently, we used the larger bin size ($\Delta\tau = 1$ month) to estimate the SF at lags > 2 months and up to ~ 2.5 years (ie the time interval between the first and last *EUVE* light curve of MRK 421).

The combined short and long bin estimated SF is plotted in Figure 14.13 (filled circles for $\Delta\tau = 1$ day and filled squares for $\Delta\tau = 1$ month). The estimated SF rises roughly logarithmically with τ at lags < 20 days. However, at lags > 60 days it is relatively flat. This flattening cannot be due to the uneven sampling of the light curve, but it is exactly what we would expect if there is a low frequency turn over in the power spectrum of MRK 421 .

We examine below whether the estimated SF shown in Figure 14.13

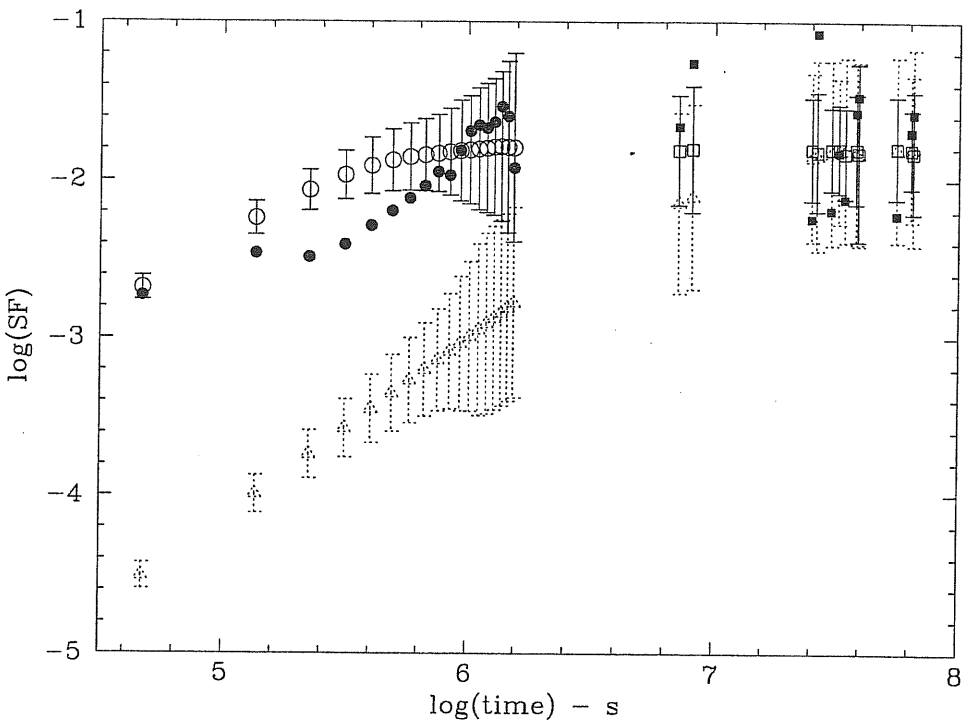

Figure 14.13: Structure Function of the total *EUVE* light curve of MRK 421 . (Figure 14.2) Filled circles correspond to the SF estimated with a lag bin of size 1 day and the filled squares to the SF estimated with a lag bin of size 1 month. Open symbols (circles and squares) correspond to the mean SF of 1000 simulated light curves with a power spectrum of slope 2.14 and a frequency turnover at 4×10^{-6} Hz. Dotted triangles correspond to the mean SF of 1000 simulated light curves with a same slope power spectrum but with a frequency turnover at 10^{-7} Hz. In both cases, the errorbars correspond to the standard deviation of the simulated SFs around their mean (see § 14.3 details).

is consistent with the assumption that the true power spectrum of MRK 421 is similar to the model defined by equation (5) with $2\alpha = 2.14$ and $f_b = 4 \times 10^{-6}$ Hz.

To answer this question, we performed a numerical experiment: we created one set of 1000 simulated light curves using the method described in appendix C of Papadakis & Lawrence (1995). Each simulated light curve has a power spectrum with slope of 2.14, a knee frequency at 4×10^{-6} Hz, and variance as the *EUVE* light curve. For each one of the simulated light curves, we estimated the SF exactly in the same way as we did with the *EUVE* light curve. Then we computed the expected mean value, $< SF_{sim}(\tau) >$, and variance, $\sigma^2_{<SF_{sim}>}(\tau)$, of all the simulated SFs at each τ. The results are plotted in Figure 14.13 (open circles and open squares for the mean short and long bin simulated SF). The "errors" on the points are equal to $\pm\sigma_{<SF_{sim}>}(\tau)$. Note

that these errors would represent the 68% of the process realizations in the case of a Gaussian distribution, but, since the actual SF are *not* normally distributed, they can only give us an idea of the real 1σ errors of the actual SF and cannot be used in the normal χ^2 estimation. In order to quantify the comparison between $\log[< SF_{sim}(\tau) >]$ and $\log[\hat{SF}(\tau)]$ in a statistical way, we estimated the sum of their squared differences, i.e. $\sum_i \{\log[< SF_{sim}(\tau_i) >] - \log[\hat{SF}(\tau_i)]\}^2$, for all the τ_i for which we have estimated the SF. We refer to this sum as "χ^2", although its definition is different from the traditional definition of χ^2. In our case, $\chi^2 = 4$. Based on the distribution of the χ^2 values for the 1000 simulated light curves, the probability that the *EUVE* light curve of MRK 421 is a realization of a process with a power spectrum with a knee frequency at 4×10^{-6} Hz is ~ 40 %.

Finally to check whether MRK 421 structure function is consistent with a break at time scales longer than the range suggested by the fit of the power spectra, we performed a second numerical experiment: we created a new set of 1000 simulated light curves, with $2\alpha = 2.14$, variance as the *EUVE* light curve variance, and a knee frequency at 10^{-7} Hz. As above, for each simulated light curve we estimated the SF, and then computed $< SF_{sim}(\tau) >$, and $\sigma_{<SF_{sim}>}(\tau)$. The results for the mean short and long bin simulated SF are plotted in Figure 14.13 (dotted triangles). At large lag values the mean simulated SF agrees well with the SF of MRK 421 . This is not surprising since, as we mentioned at the beginning of § 14.3, we expect that $SF \sim 2\sigma^2$ in the limit when τ is larger than $1/f_b$ (10^7 s in this case). However, the agreement between the mean simulated SF and the MRK 421 SF at short lags is not good. The χ^2 this time is equal to 183. Based on the distribution of the χ^2 values for the 1000 simulated light curves, the probability that the *EUVE* light curve of the MRK 421 is a realization of a process with a power spectrum with a knee frequency at 10^{-7} Hz is < 0.1 %.

We conclude that the SF of MRK 421 (Figure 14.13) is entirely consistent with the results from the power spectrum analysis (Section 14.2); the slope of the MRK 421 power spectrum is ~ -2.1 and there is a knee frequency at $\sim 4 \times 10^{-6}$ Hz, below which the spectrum flattens; in fact we found that it is highly unlikely that this knee frequency will be smaller than 10^{-7} Hz.

Chapter 15

Discussion on the timing analysis

All the *EUVE* light curves of MRK 421 show significant variations (Figures 14.3–14.7). One interpretation is that they are the result of the superposition of flares whose duration, roughly estimated from the same figures, is about 3 days; as an example we quote the 1994 lightcurve (Figure 14.3) where the source flux declines for about 3 days, rises for another $\sim$ 3.5 days and stays steady to the end of the observation ($\sim$ 3.5 days). We investigated the variability present in the light curves by means of a power spectrum analysis and our results are as follows:

- on average, the *EUVE* power spectrum of MRK 421 has a power law form with a slope -2.14 ± 0.28;
- there is a low frequency turn over at 4×10^{-6} Hz (i.e. $\sim$ 3 days, the 68% confidence range is 7×10^{-7} Hz $-$ 8×10^{-6} Hz). We cannot determine the shape of the power spectrum below this turn over, nevertheless the data so far is consistent with a flattening of the power spectrum below this frequency to a slope of zero;
- there is a strong indication that the power spectrum does not remain the same, i.e. that the *EUVE* emission of MRK 421 is not stationary. The DS 1996 observation shows a power spectrum with a slope -1.1 ± 0.2, which is much flatter than the average slope. However, this observation is again consistent with a flattening below the same frequency of 4×10^{-6} Hz.

Furthermore, we performed a structure function analysis of the total *EUVE* light curve. The structure function of the source flattens at

time scales $> 10^6$ s. Based on numerical simulations, we found that the MRK 421 SF is entirely consistent with a 2.14 power spectrum which flattens to a slope of zero below 4×10^{-6} Hz.

We will discuss each of these results in more detail in the following subsections.

15.1 The power spectrum slope

Our analysis shows that, on average, the *EUVE* power spectrum of MRK 421 (up to $\sim 10^{-4.5}$ Hz) has a power law form with a slope of -2.14 ± 0.28. No periodicities or quasi-periodicities could be found. To the best of our knowledge, this is the first time that the power spectrum of a radio-loud AGN has been estimated in the EUV. In fact, even in the X-rays, the power spectra of radio-loud objects are not well known. The only exceptions are PKS 2155-304 and MRK 421 itself. PKS 2155-304 X-ray power spectrum has been estimated in the past (Tagliaferri et al 1991, Zhang et al 1999) to have a slope of ~ -2, similar to the slope of the X-ray power spectrum of MRK 421 (Takahashi et al. 2000, Brinkmann et al. 2001) and to our estimated slope in the EUV. Both objects are High frequency peak BL Lac objects, and their *EUVE* and X-ray emission are thought to be due to synchrotron radiation. The similarity in the power spectrum slopes could imply that in addition to the same emission mechanism, the same variability mechanism operates in both objects in the two bands.[1]

In general, red noise power spectra can result from a shot-noise model, i.e. from a superposition of random "flare"-like events, each one with the same duration and shape, and with an amplitude randomly distributed around a mean value. A slope $\alpha = 2$ is expected in the case of exponentially decaying shots, consistent with our best fit slope value. However, the shape of the flares in the *EUVE* light curves of MRK 421 can by eye, be more complicated than that; they are asymmetric and they do not have the same shape all the times. For example, the first flare in the DS 1995 lightcurve (Figure 14.5) shows a relatively slow rise (it reaches maximum after ~ 2 days), and faster decline (~ 1 day). Immediately after this the source rises again, reaching now the maximum after ~ 1 day. Even if it is not clear what happens after

[1]The normalized amplitude of the PKS 2155-304 X-ray power spectrum at 10^{-5} Hz is > 1000 (Zhang et al. 1999), when for MRK 421 the normalized amplitude of *EUVE* power spectrum at the same frequency, is 148 ± 33 (Table 14.1).

the maximum (if there is a second flare or not) this difference in rise times indicates that the flares are not always the same. Probably, there are flares which rise slow and decay fast and flares with the opposite behavior, or the complicated shapes can be the result of the superposition of consecutive flares.

In general, knowledge of the power spectrum slope alone cannot provide us with much information on the variability mechanism that operates in the source. One has to work the other way around; develop a model for the variability mechanism, predict the shape of flares, hence the power spectrum slope, and then compare it with the data.

Even though more work is needed in order to investigate if any model can produce light curves with the correct power spectrum slope, amplitude and low frequency knee, it is interesting to notice the similarity between the shape of some of the flares in the *EUVE* light curves of MRK 421 and those predicted by Celotti et al. (1991). The flare at the beginning of the DS 1995 light curve (Figure 14.5) resemble by eye the flare expected in the case of a perturbation with growing thickness in an inhomogeneous jet (Figure 4b of Celotti et al. 1991). A different behavior is present in the second flare in the same light curve; this time the flux of the source continues to be large after reaching the maximum and the amplitude of the event is smaller than in the previous case. This flare could correspond to the case in Figure 4a of Celotti et al. (1991), in which they used different parameters for the stationary jet structure.

15.2 The low frequency turn over

The presence of a low frequency knee, with a value that remains constant, within the error bars, in all the *EUVE* power spectra of MRK 421 , indicates the presence of a "characteristic time scale" (t_{var}) in the system. This time scale determines the "memory" of the system, i.e. the variability mechanism operates in such a way so that, whatever the origin and nature of variations, they "last" typically for a period which is, on average, equal to $t_{var} \sim 1/(4 \times 10^{-6})$ Hz ~ 3 days. For example, according to the simple shot noise model mentioned above, the "memory" of the system is determined by the duration of the flares. If, on average, they last for t_{var} days, a low frequency knee at $\sim 1/t_{var}$ is expected. As we mentioned in the beginning of this section, visual inspection of the MRK 421 *EUVE* lightcurves implies that the flares

in them last for ~ 3 days.

The fact that the low frequency knee remains constant implies that t_{var} is determined by a characteristic of the source that does not change with time. Such a permanent characteristic might be the size of the *EUV* emitting region. If that is the case, then an upper limit to the source size at rest frame, R, is given by $R = t_{var} \times (\delta c)$, where δ is the Doppler factor. For $t_{var} \sim 3$ days and a typical value of $\delta \sim 10$, the source size should be less than $\sim 8 \times 10^{16}$ cm. This value is similar to the value of 4.8×10^{16} cm and 4.7×10^{16} cm that Chiaberge & Ghisellini (1999) and Mastichiadis & Kirk (1997) find from theoretical modeling of multifrequency energy spectra of MRK 421 .

Recently, Maraschi et al. (1999) proposed the e-folding times scales of 10.7×10^4 s, 7.1×10^4 s, and 5.3×10^4 s at 1, 5 and 15 keV respectively for a large flare observed by *BeppoSAX*. These time scales were calculated from a simple arbitrary exponential fitting to a single event in the *BeppoSAX* light curve. If they represent indeed a characteristic time scale of the system at these energies, then this time scale decreases with energy. The time scale derived from EUV data is 2.6×10^5, i.e. larger than the time scales in the X-ray band. If the time scale is associated with the source size, then these numbers are consistent with models in which the source size is expected to decrease with energy. A more detailed comparison has to wait for a proper statistical analysis of the X-ray data.

An indication of a break at ~ 0.5 days is present also in the structure function analysis performed on a simultaneous *ASCA*, *Beppo-SAX* and *RXTE* observation in 1998 (Takahashi et al. 2000) and on *Beppo-SAX* 2000 observation of MRK 421 (Zhang Y. H. 2000 private communication). Assuming that the bulk of *Beppo-SAX*, *ASCA* and *RXTE* emission is at $\sim 3 - 4$ keV, the 6 times longer EUV (~ 0.1 keV) break could be explained with the synchrotron cooling of the same electron population emitting in the *Beppo-SAX* range. The cooling time in fact is proportional to energy of the electrons which emit at a frequency proportional to the inverse of square root of the electron energy. Therefore the cooling time is proportional to the inverse of the square root of the observed frequency.

15.3 Evidence of non-stationarity: DS 1996 data

As is evident from Figure 14.8 and Figure 14.11, the slope of DS 1996 power spectrum (open circles) is flatter than the others, showing the non stationary nature of MRK 421 emission. The appearance of the DS 1996 light curve (§ 14.1.5) agrees well with the power spectrum of that light curve. The flatter slope of the DS 1996 power spectrum indicates larger amplitude variations at high frequencies, i.e. lots of short time variations, consistent with the presence of a number of short lived flares, and the absence of any long "trend" in the light curve itself. Changes in the power spectrum indicates that some of the variability mechanism characteristics change with time. PKS 2155-304 also shows evidence for non-stationarity in its X-ray light curves (Zhang et al 1999). MRK 421 has shown evidence of "non-stationarity" in the past: Fossati et al 2000, in a simultaneous TeV and X-ray observation, found that the hard X-rays were delayed with respect to the soft X-rays, opposite to the behavior previously observed (Takahashi et al 1996).

In the context of the shot-noise model, in DS 1996 power spectrum: (a) the different slope indicates a difference in the flare shape; (b) the roughly similar amplitude (Figure 14.8) suggests that probably both the number of flares per unit time and their amplitude has not changed drastically during DS 1996 observation; (c) the knee at the same frequency, within the errors, of the other power spectra indicates that the duration of DS 1996 flares is not changed.
To the eye, though the flares in the DS 1996 light curve appear to be relatively short-lived. We speculate that the DS 1996 flares consist of two parts: one with a fast decay/rise evolution, and another one with a much slower evolution, not seen directly in the light curve, due to the blending of consecutive flares.

The extremely large *EUVE* database on MRK 421 ($\sim$ 1100 ks) offers a so far unique opportunity to study the variability properties of a BL Lacertae object at high energies. We analyzed MRK 421 light curves by means of the power spectrum and structure function techniques; in a power spectrum with slope -2.14 ± 0.28 we find indication, confirmed by the structure function analysis, of a break at $\sim$ 3 days. This is the first time that a break in the power spectrum of a BL Lacertae object is found. We also find evidence of non-stationarity for MRK 421 EUV

emission.

The few existing models on BL Lacertae objects variability (Celotti et al. 1991, Chiaberge & Ghisellini 1999, Georganopoulos & Marscher 1998), developed for multifrequency analysis, try to explain the amplitude and delays observed among the various energy bands. The single energy approach, as the one proposed in this thesis, is at least as promising as the multifrequency approach, but no predictions on the power spectrum and on the structure function shapes (the most widely used analysis methods to quantify the variability of an object) have never been derived from any of the current models.
It is beyond the scope of this thesis to investigate in detail whether the model flares that have been computed so far can reproduce the results from the analysis of the *EUVE* light curves of MRK 421 and we reserve this for future studies. However, such a quantitative work, will be very interesting since it may be able to distinguish between different models that have been proposed to explain the high frequency emission of blazars.

Chapter 16

Summary and conclusions on MRK 421

We performed a detailed spectral and timing analysis on the $\sim$ 1000 ks of public data available as of January 1999 for the bright and nearby BL Lacertae object MRK 421. The aims of the work were:
- check previous reports of absorption lines in the *EUVE* spectrum of MRK 421 (Kartje et al. 1997), based on the extrapolation of the X-ray spectrum and on the use of an inappropriate effective area;
- perform a detailed variability analysis by means of power spectrum and structure function techniques to constrain emission mechanisms models.

The main result of the spectral analysis is that, despite the extrapolation of the X-ray spectrum performed by Kartje et al. (1997) was inaccurate due to the curved nature of the X-ray spectrum of BL Lacertae objects in the X-ray regime (§ 12.3) and despite the increase of the importance of the absorption feature due to the use of the inappropriate on-axis effective area by Kartje et al. (1997) (§ 12), an absorption feature is still present in the $\sim 71-75$ Å range with FWHM varying from 0.2 to 6 Å (§ 12.5). To our knowledge, no calibration uncertainty in this region could produce such a feature and indeed no other class of objects have comparable lines in *EUVE* spectra.

We interpreted this feature in the context of the Konigl et al. (1995) model for PKS 2155-304 as a superposition of Mg VIII and Mg IX absorption lines. The implied ionization state of the gas would require stronger O VII absorption in the X-ray range than is allowed by observations and the authors invoke subcosmic oxygen abundance to

explain its absence. According to photoionization equilibrium models (Nicastro et al. 1999, Nicastro et al. 2000) which include the strongest 300 emission and resonant absorption lines down to 50 eV (oscillator strength > 0.1) the predicted wavelengths and strengths of the absorption lines, both absolute and relative, are highly sensitive to the properties of the photoionizing continuum and the absorbing gas (e.g. the ionization state and the assumed outflowing velocity). The number of transitions in the model also has a strong effect, but under reasonable assumptions (§ 12.5) an OVII Kα absorption line (EW=0.25Å) and a FeIX L ($\lambda_{\rm rest}$ = 82.43 Å, EW=0.2Å) absorption lines are expected respectively around 0.6 keV and 73 Å.

Even if Konigl et al. (1995) model predicts the existence of related lines in the $\sim$ 0.55 keV range the present situation is consistent with no absorption detected in this energy range possibly with the exception of faint absorbing/emitting features detected by *Chandra* (Nicastro et al. 2000).

The line we found is so far the strongest proof of the presence of absorption in BL Lacs. The absorption feature improves all the spectral fits of MRK 421 *EUVE* spectrum improving the χ^2 of 52% and 32% in 1995 and 1996 observations respectively. *EUVE* has now concluded its mission and such absorption feature could only be confirmed or rejected by *Chandra* or *XMM-Newton* observations in their lowest energy range.

The variability analysis performed on MRK 421 *EUVE* lightcurves showed that:
- the slope of the power spectrum is on average -2.14 ± 0.28, consistent with a red-noise model due to the superposition of exponentially decaying/rising flares;
- there is a low frequency turnover in the power spectrum around $\sim$ 3 days. This is the first indication of the presence of a characteristic time scale in the emission of this BL Lac; a similar flattening in the power spectrum has been found at $\sim$ 0.5 days in the X-ray band for the same object by Takahashi et al. 2001. How this time scale is related to the physics of the central engine or of the jet is still unknown. The easiest way to interpret a characteristic time scale is that it is related to the size of the emitting region. If indeed this is the case, assuming a $\delta \sim 10$ we would have $\sim 8 \times 10^{16}$

cm in the EUV band and $\sim 1.3 \times 10^{16}$ cm in the X-rays, in agreement with with models in which the source size is expected to decrease with energy. The different time scales could otherwise be related to the same population of emitting electrons and the 6 times longer EUV (~ 0.1 keV) time scale could be explained with the synchrotron cooling of the same electron population emitting in the *Beppo-SAX* range ($\sim 3 - 4$ keV) according to the synchrotron cooling formula:

$$t_{\text{syn cooling}} \sim E \sim \nu^{-2}$$

Some models able to predict the lightcurves shape of BL Lacs have been developed (§ 15.3) but none of them still predicts the shape and features of the power spectrum and a quantitative comparison is not possible nowadays.

- The third result of the variability analysis is that MRK 421 emission is not stationary as the slope of the power spectrum changes with time (§ 14.2.1), complicating even further the modeling of the source variability.

We were able to reproduce the structure function of MRK 421 with the superposition of exponentially decaying flares with characteristic time scale of ~ 3 days.

The analysis provided in this thesis on MRK 421 showed the presence of gas in the proximity of the central engine as evident from an absorption feature at $\sim 71 - 75$ Å and showed that MRK 421 EUV emission is non-stationary but has a characteristic time scale of ~ 3 days. Even though a physical interpretation of the shape of MRK 421 structure function (power spectrum) has to wait for the prediction of theoretical modeling based on several physical parameters, we were able to reproduce the shape of MRK 421 structure function with a superposition of exponentially decaying flares with characteristic time scale of ~ 3 days.

Chapter 17

Summary and conclusions

We used for this work the reservoir of still unexploited scientific possibilities of study contained in public data for the investigation of extreme and rare sources. We briefly review in this chapter the main results of this thesis, referring the reader to the appropriate sections for a more detailed discussion.

17.1 Part I: *ROSAT* blank field sources

We called blank field sources the *ROSAT* bright unidentified X-ray sources with faint optical counterparts, with $O > 21.5$ on the Palomar Sky survey. The extreme X-ray over optical flux ratio of blank field sources is not compatible with the main classes of X-ray emitters except for BL Lacertae objects at $f_X/f_V \leq 35$. The possibilities regarding the nature of blank field sources are discussed in § 2.1 and include, isolated neutron stars, failed clusters, high redshift and luminous clusters of galaxies, obscured AGNs, ADAFs, GRB afterglows or other extremely variable sources. From the analysis of *ROSAT* archival data we found evidence for only three sources, out of 16, needing absorption in excess of the Galactic value (§ 3.1.1), and no indication of variability (§ 3.1.3). We also found evidence for an extended nature for only one of the 5 blanks with an HRI detections (§ 3.2), thus suggesting a high redshift cluster nature for this source (1WGA J1226.9+3332), later confirmed by a *Chandra* observation (§ 6.2).
Optical and IR imaging of the 16 blank field sources revealed the presence of a red ($R - K \geq$??) counterpart in the X-ray error circle for 5 **(check this with R-K)** of them and a K-band number count excess for 3 of them (§ 4.3). One of these red sources with

excess of counts is the already mentioned z=0.89 cluster of galaxies 1WGA J1226.9+3332; one was identified in the SHARC survey (Romer et al. 2000) as a z=0.45 cluster and we propose the third one as a high ($0.5 \leq z \leq 1$) redshift cluster of galaxies candidate (§ 5.1.2). Another source, 1WGA J1103.5+2459 is likely to be a high redshift ($z \sim 1$) cluster of galaxies.
The extreme $f_X/f_V > 100$ found for 1WGA J1340.1+2743 is explained by the combination of the lineless spectrum taken by Lamer, Brunner & Staubert (1997) and of a *Chandra* observation showing the source $\sim$ 10 times fainter than in *ROSAT*: this object is likely to be an extreme BL Lacertae object, similar to the sources presented in Costamante et al. (2001).

Among blank field sources we note the presence of 5 AGN-like objects (§ 7.3) which seem to form a well defined group: they present type 1 X-ray spectra and red Palomar **and R-K???** counterparts. We discuss the possible explanations to the discrepancy between the indication coming from X-ray and optical data in § 7.3, among which: a suppressed BBB emission (ADAF or shifted BBB as in RE J1034+396), an extreme ($\sim$ 40 – 60 the Galactic ratio) dust to gas ratio value and a high redshift ($z \geq 3.5$) QSO nature. These AGN-like blanks seem to the the bright analogs of the being found in deep *Chandra* observations (Hornschemeier et al. 2001; Fiore et al. 2000). The continuously increasing number of sources with extreme f_X/f_V observed by *Chandra* and *XMM-Newton* will help us to understand the optical weakness/disappearance of the AGN in these X-ray bright sources.

Other sources (§ 7.6) have a still unknown nature; while two of them might be related to a nearby galaxy and be X-ray binaries, for the remaining three sources we can only exclude a bursting nature and, for the lack of red counterparts, the high redshift cluster of galaxies and the obscured AGNs possibilities (§ 7.6).

17.2 Part II: The BLEIS project

In this part of the thesis we present the pilot study for the selection of a faint optical blazar sample to test unified and evolutive models. Cross-correlating the public data from the ESO Imaging Survey Wide (EIS-Wide) Patch B with the NVSS we obtain a sample of 15 candidates whose broad band spectral index (α_{ro}) is consistent with the observed distribution of radio selected BL Lacs, FSRQ and partially with radio

galaxies and X-ray selected BL Lacs (§ 9.1.4). We attempt an optical classification using the color-color diagram presented in Zaggia et al. (1999) and compare the results to models predictions in § 10.

This was a pilot study for a larger work and we note that indeed a larger statistics, i.e. the extension of the work to the whole 16 deg^2 covered by the EIS-Wide, and a spectroscopic classification of the candidates is needed for conclusive results.

17.3 Part III: MRK 421

This part of the thesis deals with the accurate spectral and timing analysis of the $\sim$ 1000 ks of public data available in the *EUVE* archive for the BL Lacertae object MRK 421. The aims of the work were:
- check previous reports of absorption lines in the *EUVE* spectrum of MRK 421 (Kartje et al. 1997), based on the extrapolation of the X-ray spectrum and on the use of an inappropriate effective area;
- perform a detailed variability analysis by means of power spectrum and structure function techniques to constrain emission mechanisms.

The main result of the spectral analysis is that, despite the correction of the inaccurate calibrations and extrapolations performed in Kartje et al. (1997) an absorption feature is still present in the $\sim 71 - 75$ Å range with FWHM varying from 0.2 to 6 Å (§ 12.5). The absorption feature (interpreted in the context of the Konigl et al. (1995) model as a superposition of Mg VIII and Mg IX absorption lines) is so far the strongest proof of the presence of absorption, and thus of gas near the central engine, in BL Lacs.

The variability analysis performed on MRK 421 *EUVE* lightcurves showed that:
- the slope of the power spectrum is on average -2.14 ± 0.28, consistent with a red-noise model due to the superposition of exponentially decaying/rising flares;
- there is a low frequency turnover in the power spectrum around ~ 3 days. This is the first indication of the presence of a characteristic time scale in the emission of this BL Lac; a similar flattening in the power spectrum has been found at ~ 0.5 days in the X-ray band for the same object by Takahashi et al. (2001).
- The third result of the variability analysis is that MRK 421 emission is not stationary as the slope of the power spectrum changes with time

(§ 14.2.1), complicating even further the modeling of the source variability.

Even though a physical interpretation of the shape of MRK 421 structure function (power spectrum) has to wait for the prediction of theoretical models, we were able to reproduce the shape of MRK 421 structure function with a superposition of exponentially decaying flares with characteristic time scale of ~ 3 days.

17.4 Future work

Both the projects presented in the first and second part of the thesis leave unanswered questions, mainly regarding the nature of the so far unidentified sources. We obtained 5 more *Chandra* and 2 more *XMM-Newton* observations for the *ROSAT* blank field sources and they will be soon available; their good accurate positions, coupled with the deeper multicolor imaging we recently obtained (the data is not reduced yet and is not presented in this thesis) will identify the real counterpart among the $\sim 3-7$ sources present by chance in each X-ray error circle. Spectroscopical classification of the counterparts will possibly provide the reason for the discrepancy between X-ray brightness and optical faintness for the AGN-like sources and unveil the real nature of the cluster candidates and of the sources with an unknown nature.

Spectroscopic follow-up is also essential for the candidates blazars, quasars and radio galaxies selected in the BLEIS pilot sample. This will provide a classification and a redshift; the number counts, the redshift distributions and the luminosity function for the various classes of objects will constrain unified and evolutive models of blazars.

Write thanks to people here.

scientific:

and personal:

Bibliography

[] Akiyama, M. et al. 2000, PASJ, 52, 577, *Deep-Imaging Observations of a Candidate of an Absorbed QSO at z=0.653, AX J131831+3341*

[] Antonucci, R., 1993, ARA&A, 31, 473, *Unified models for active galactic nuclei and quasars*

[] Antonucci, R. R. J. & Miller, J. S., 1985, ApJ, 297, 621 *Spectropolarimetry and the nature of NGC 1068*

[] Bade, N., Fink, H. H., Engels, D., Voges, W., Hagen, H.-J., Wisotzki, L. & Reimers, D., 1995, A&AS, 110, 469, *AGN from the ROSAT all-sky survey*

[] Borgani, S. & Guzzo, L., 2001, Nature, 409, 39, *X-ray clusters of galaxies as tracers of structure in the Universe*

[] Boyle, B. J., McMahon, R.G., Wilkes, B. J. & Elvis, M., 1995, MNRAS, 272, 462 *The Cambridge-Cambridge ROSAT Serendipity Survey - I.X-ray-luminous galaxies*

[] Boyle, B. J., Almaini, O., Georgantopoulos, I., Blair, A. J., Stewart, G. C., Griffiths, R. E., Shanks, T., Gunn, K. F., 1998, MNRAS, 297, 53, *ASCA observations of deep ROSAT fields - III. The discovery of an obscured Type 2 AGN at z=0.67*

[] Cagnoni, I., Elvis, M., Kim, D.-W., Mazzotta, P., Huang, J.-S. & Celotti, A., 2001, ApJ in press (astro-ph/0106066) *1WGAJ1226.9+3332: a high redshift cluster discovered by Chandra*

[] Chen, X., Abramowicz, M. A., Lasota, J.-P., Narayan, R. & Yi, I., 1995, ApJ, 443, L61, *Unified description of accretion flows around black holes*

[] Colpi, M., Turolla, R., Zane, S. & Treves, A., 1998, ApJ, 501, 252, *The Elusiveness of Old Neutron Stars*

[] Comastri, A., Fiore, F., Vignali, C., Matt, G., Perola, G.C. & La Franca, F., 2001, MNRAS in press (astro-ph/0105525) *The BeppoSAX High Energy Large Area Survey HELLAS, III: testing synthesis models for the X-ray background*

[] Costamante, L., Ghisellini, G., Giommi, P., Tagliaferri, G., Celotti, A., Chiaberge, M., Fossati, G., Maraschi, L., Tavecchio, F., Treves, A. & Wolter, A., 2001, A&A, 371, 521, *Extreme synchrotron BL Lac objects. Stretching the blazar sequence*

[] Della Ceca, R., Scaramella, R., Gioia, I. M., Rosati, P., Fiore, F. & Squires, G., 2000, A&A, 353, 498, *BeppoSAX observations of two high redshift clusters of galaxies: RXJ 0152.7-1357 and MS 2053.7-0449*

[] Di Matteo, T., Quataert, E., Allen, S. W., Narayan, R.& Fabian, A. C., 2000, MNRAS, 311, 507, *Low-radiative-efficiency accretion in the nuclei of elliptical galaxies*

[] Ebeling, H., Jones, L. R., Perlman, E., Scharf, C., Horner, D., Wegner, G., Malkan, M., Fairley, B. W. & Mullis, C. R., 2000, ApJ, 534, 133, *The WARPS Survey. III. The Discovery of an X-Ray Luminous Galaxy Cluster at z=0.833 and the Impact of X-Ray Substructure on Cluster Abundance Measurements*

[] Esin, A. A.; Narayan, R.; Cui, W., Grove, J. E.; Zhang, S.-N., 1998, ApJ, 505, 854 *Spectral Transitions in Cygnus X-1 and Other Black Hole X-Ray Binaries*

[] Fabian, A.C. & Iwasawa, K., 1999, MNRAS, 303, L34, *The mass density in black holes inferred from the X-ray background*

[] Fanaroff, B. L. & Riley, J. M., 1974, MNRAS, 167, 31, *The morphology of extragalactic radio sources of high and low luminosity*

[] Fiore, F., Elvis, M., Giommi, P. & Padovani, P., 1998, ApJ, 492, 79, *X-Ray Spectral Survey of WGACAT Quasars. I. Spectral Evolution and Low-Energy Cutoffs*

[] Fossati, G., Maraschi, L., Celotti, A., Comastri, A. & Ghisellini, G., 1998, MNRAS, 299, 433, *A unifying view of the spectral energy distributions of blazars*

[] Franceschini, A., Bassani, L., Cappi, M., Granato, G. L., Malaguti, G., Palazzi, E. & Persic, M., 2000, A&A, 353, 910, *BeppoSAX uncovers a type-2 QSO in the hyperluminous infrared galaxy IRAS 09104+4109*

[] Frontera, F., Amati, L., Costa, E., Muller, J. M., Pian, E., Piro, L., Soffitta, P., Tavani, M., Castro-Tirado, A., Dal Fiume, D., Feroci, M., Heise, J., Masetti, N., Nicastro, L., Orlandini, M., Palazzi, E. & Sari, R., 2000, ApJS, 127, 59, *Prompt and Delayed Emission Properties of Gamma-Ray Bursts Observed with BeppoSAX*

[] Gilli, R., Risaliti, G. & Salvati, M., 1999, A&A, 347, 424, *Beyond the standard model for the cosmic X-ray background*

[] Gilli, R., Salvati, M. & Hasinger, G., 2001, A&A, 366, 407, *Testing current synthesis models of the X-ray background*

[] Gioia, I.M. & Luppino, G. A., 1994, ApJS, 94, 538, *he EMSS catalog of X-ray-selected clusters of galaxies. 1: an atlas of CCD images of 41 distant clusters*

[] Giommi, P. & Padovani, P., 1994, MNRAS, 268, L51, *Bl-Lacertae Reunification*

[] Greiner, J., Hartmann, D. H., Voges, W., Boller, T., Schwarz, R. & Zharikov, S. V, 2000, A&A, 353, 998, *Search for GRB X-ray afterglows in the ROSAT all-sky survey*

[] Haberl, F. 1996????

[] Haberl, F., Motch, C., Buckley, D.A.H., Zickgraf, F. & Pietsch, W., 1997, A&A, 326, 662, *RXJ0720.4-3125: strong evidence for an isolated pulsating neutron star*

[] Haberl, F., Motch, C. & Pietsch, W., 1998, Astron. Nachr., 319, 97, *Isolated neutron stars in the ROSAT Survey*

[] Haberl, F., Pietsch, W. & Motch, C., 1999, A&A, 351, L53, *RX J0420.0-5022: an isolated neutron star candidate with evidence for 22.7 s X-ray pulsations*

[] Halpern, J. P., Turner, T. J. & George, I. M., 1999, MNRAS, 307, 47, *Are there any Type 2 QSOs? The case of AXJ0341.4-4453*

[] Henry, J.P., 2000, ApJ, 534, 565, *Measuring Cosmological Parameters from the Evolution of Cluster X-Ray Temperatures*

[] Huang, J.-S., Thompson, D., Kümmel, M. W., Meisenheimer, K., Wolf, C., Beckwith, S. V. W., Fockenbrock, R., Fried, J. W., Hippelein, H., von Kuhlmann, B., Phleps, S., Röser, H.-J. & Thommes, E., 2001, A&A, 368, 787, *The Calar Alto Deep Imaging Survey: K-band Galaxy number counts*

[] Janka, H.-T. & Ruffert, M., 1996, A&A, 307, L33, *Can neutrinos from neutron star mergers power gamma-ray bursts?*

[] Lacy, M. Laurent-Muehleisen, S. A., Ridgway, S. E., Becker, R. H. & White, R. L., 2001, ApJ, 551, 17 *The Radio Luminosity-Black Hole Mass Correlation for Quasars from the FIRST Bright Quasar Survey and a "Unification Scheme" for Radio-loud and Radio-quiet Quasars*

[] La Franca, F. Fiore, F., Vignali, C., Comastri, A., Pompilio, F. & HELLAS consortium, 2001, Proc. of the Conference "the New Era of Wide-Field Astronomy", held in Preston (UK), 21-24 August 2000 (astro-ph/0011008), *The evolution of AGN in the Hard X-rays from HELLAS*

[] Livio, M., Xu, C. & Frank, J., 1998, ApJ, 492, 298, *On the Magnetic Field Evolution in Isolated Neutron Stars*

[] Lu, Y. & Yu, Q., 1999, ApJ, 526, L5, *Two Different Accretion Classes in Seyfert 1 Galaxies and QSOS*

[] Maccacaro, T., Gioia, I. M., Wolter, A., Zamorani, G. & Stocke, J. T., 1988, ApJ, 326, 680, *The X-ray spectra of the extragalactic sources in the Einstein extended medium sensitivity survey*

[] Madau, P. & Blaes, 0., 1994, ApJ, 423, 748, *Constraints on Accreting, Isolated Neutron Stars from the ROSAT and EUVE Surveys*

[] Maiolino, R., Marconi, A., Salvati, M., Risaliti, G., Severgnini, P., Oliva, E., La Franca, F. & Vanzi, L., 2001, A&A, 365, 28 *Dust in active nuclei. I. Evidence for "anomalous" properties*

[] Maoz, E., Ofek, E.O. & Shemi. A., 1997, MNRAS, 287, 293, *Evidence for a new class of extreme ultraviolet sources*

[] McMahon, R.G. & Irwin, M.J., 1992, in Digitized Optical Sky Surveys, ed. H.T. MacGillivray & E.B. Thomson (Dordrecht: Kluwer), 417

[] Miyaji, T., Hasinger, G. & Schmidt, M., 2000, AdSpR, 25, 827, *Evolution of AGNS and A Model of the X-Ray Background*

[] Motch, C., Harbel, F., Zickgraf, F., Hasinger, G. & Schwope, A.D., 1999, A&A, 351, 177, *The isolated neutron star candidate RX J1605.3+3249*

[] Narayan, R. & Yi, I., 1994, ApJ, 428, L13, *Advection-dominated accretion: A self-similar solution*

[] Narayan, R., Mahadevan, R., Grindlay, J. E., Popham, R. G. & Gammie, C., 1998, ApJ, 492, 554, *Advection-dominated accretion model of Sagittarius A*: evidence for a black hole at the Galactic center*

[] Neuhauser, R., Thomas, H., Danner, R., Peschke, S. & Walter, F. M., 1997, A&A, 318, L43

[] Nicastro, F., Fiore, F. & Matt, G., 1999, ApJ, 517, 108, *Resonant Absorption in the Active Galactic Nucleus Spectra Emerging from Photoionized Gas: Differences between Steep and Flat Ionizing Continua*

[] Nonino, M., Bertin, E., da Costa, L., Deul, E., Erben, T., Olsen, L., Prandoni, I., Scodeggio, M., Wicenec, A., Wichmann, R., Benoist, C., Freudling, W., Guarnieri, M. D., Hook, I., Hook, R., Mendez, R., Savaglio, S., Silva, D. & Slijkhuis, R., 1999, A&AS, 137, 51, *ESO Imaging Survey. I. Description of the survey, data reduction and reliability of the data*

[] Peebles, P., 1980, *The large scale structure of the Universe*, Princeton: Princeton University Press

[] Popov, S., Colpi, M., Treves, A., Turolla, R., Lpunov, V. M. & Prokhorov, M. E., 200, ApJ, 530, 896, *The Neutron Star Census*

[] Prandoni, I., Wichmann, R., da Costa, L., Benoist, C., Méndez, R., Nonino, M., Olsen, L. F., Wicenec, A., Zaggia, S., Bertin, E., Deul, E., Erben, T., Guarnieri, M. D., Hook, I., Hook, R., Scodeggio, M.& Slijkhuis, R., 1999, A&A, 345, 448, *ESO imaging survey. III. Multicolor data near the South Galactic Pole*

[] Press, W.H. & schchter, P., 1974, ApJ, 187, 425, *Formation of Galaxies and Clusters of Galaxies by Self-Similar Gravitational Condensation*

[] Puchnarewicz, E. M., Mason, K. O., Siemiginowska, A. & Pounds, K. A., 1995, MNRAS, 276, 20, *The high-temperature big blue bump in the Seyfert galaxy RE J1034+396*

[] Puchnarewicz, E. M., Mason, K. O., Siemiginowska, A., Fruscione, A., Comastri, A., Fiore, F. & Cagnoni, I., 2001, ApJ, 550, 644, *Constraining the Black Hole Mass and Accretion Rate in the Narrow-Line Seyfert 1 Galaxy RE J1034+396*

[] Rees, M.J., 1984, ARA&A, 22, 471 *Black Hole Models for Active Galactic Nuclei*

[] Risaliti, G., Marconi, A., Maiolino, R., Salvati, M. & Severgnini, P, 2001, A&A, 371, 37

[] Rosati, P., della Ceca, R., Norman, C. & Giacconi, R., 1998, ApJ, 492, L21, *The ROSAT Deep Cluster Survey: The X-Ray Luminosity Function Out to z=0.8*

[] Rosati, P., Stanford, S. A., Eisenhardt, P. R. Elston, R., Spinrad, H., Stern, D. & Dey, A., 1999, AJ, 118, 76, *An X-Ray-Selected Galaxy Cluster at Z = 1.26*

[] Sanders, D. B., Phinney, E. S., Neugebauer, G., Soifer, B. T., Matthews, K., 1989, ApJ, 347, 29, *Continuum energy distribution of quasars - Shapes and origins*

[] Schmidt, M., Hasinger, G., Gunn, J.; Schneider, D., Burg, R., Giacconi, R., Lehmann, I., MacKenty, J., Trumper, J. & Zamorani, G., 1998, A&A, 329, 495, *The ROSAT deep survey. II. Optical identification, photometry and spectra of X-ray sources in the Lockman field*

[] Schwope, A.D., Hasinger, G., Schwarz, R., Haberl, F. & Schmidt, M., 1999, A&A, 341, L51, *The isolated neutron star candidate RBS1223 (1RXS J130848.6+212708)*

[] Shakura, N. I. & Sunyaev, R. A., 1973, A&A, 24, 337, *Black holes in binary systems. Observational appearance*

[] Stanford, S.A., Holden, B., Rosati, P., Tozzi, P., Borgani, S., Eisenhardt, P. R. & Spinrad, H., 2001, ApJ, 552, 504, *The Intracluster Medium in z>1 Galaxy Clusters*

[] Stark, A. A., Gammie, C. F., Wilson, R. W., Bally, J., Linke, R. A., Heiles, C. & Hurwitz, M., 1992, ApJS, 79, 77, *The Bell Laboratories H I survey*

[] Stickel, M., Fried, J. W., Kuehr, H., Padovani, P. & Urry, C. M., 1991, ApJ, 374, 431, *The complete sample of 1 Jansky BL Lacertae objects. I - Summary properties*

[] Stickel, M., Meisenheimer, K. & Kuehr, H, 1994, A&AS, 105, 211, *The optical identification status of the 1 Jy radio source catalogue*

[] Stocke, J.T, Wang, Q.D., Perlman, E.S., Donahue, M.E. & Schachter, J.F., 1995, AJ, 109, 1199, *Discovery of a candidate old, isolated neutron star in the field of a galactic cirrus cloud*

[] Tozzi, P. & Norman, C., 2001, ApJ, 546, 63, *The Evolution of X-Ray Clusters and the Entropy of the Intracluster Medium*

[] Treves, A., Turolla, R., Zane, S. & Colpi, M., 2000, PASP, 112, 297, *Isolated Neutron Stars: Accretors and Coolers*

[] Seyfert, C., 1943, ApJ, 97, 28

[] Tucker, W.H., Tananbaum, H. & Remillard, R.A., 1995, ApJ, 444, 532, *A search for 'failed clusters' of galaxies*

[] Urry, C. M., Padovani, P. & Stickel, M., 1991, ApJ, 382, 501, *Fanaroff-Riley I galaxies as the parent populations of BL Lacertae objects. III - Radio constraints*

[] Urry, C. M, & Padovani, P., 1995, PASP, 107, 803, *Unified Schemes for Radio-Loud Active Galactic Nuclei*

[] Ueda, Y., Ishisaki, Y., Takahashi, T., Makishima, K., and Ohashi, T., "The ASCA Medium Sensitivity Survey (the GIS Catalog Project): Source Catalog", 2001, ApJS, in press.

[] Walter, F. M., Wolk, S. J. & Neuhauser, R., 1996, Nature, 379, 233, *Discovery of a nearby isolated neutron star*

[] White, N., Giommi, P. & Angelini, L., 1995, WGACAT, http://heasarc.gsfc.nasa.gov/W3Browse/all/wgacat.html

[] White, S.D.M. & Frenk, C.S., 1991, ApJ, 379, 52, *Galaxy formation through hierarchical clustering*

[] Wolter, A., Gioia, I. M., Maccacaro, T., Morris, S. L. & Stocke, J. T., 1991, ApJ, 369, 314, *The number count distribution for X-ray-selected BL Lacertae objects and constraints on the luminosity function*

[] Wolter, A., Caccianiga, A., della Ceca, R. & Maccacaro, T., 1994, ApJ, 433, 29, *Luminosity functions of BL Lacertae objects*

[] Zaggia, S., Hook, I., Mendez, R., da Costa, L., Olsen, L. F., Nonino, M., Wicenec, A., Benoist, C., Deul, E., Erben, T., Guarnieri, M. D., Hook, R., Prandoni, I., Scodeggio, M., Slijkhuis, R. & Wichmann, R., 1999, A&AS, 137, 75, *ESO Imaging Survey. IV. Multicolor analysis of point-like objects toward the South Galactic Pole*

[] Caccianiga, A. et al. 1999, ApJ, 513, 51

[] Caccianiga, A. et al. 2000, A&AS, 144, 247

[] Caccianiga, A. et al., 2001, in "Blazars demogrphics and physics", ASP Conference Series, ??, ??, ed. P. Padovani & M.C. Urry (astro-ph/0009388)

[] Cagnoni, I., Celotti, A. & Poccecai, D., 2000, ???? (astro-ph/?????)

[] Da Costa et al. 1999 The Messenger ???

[] Di Serego Alighieri, S., Danziger, J., Morganti, R. & Tadhunter, C., 1994, MNRAS, 269, 998

[] Elvis et al. 1992 slew survey

[] Fleming, T. A., Green, R. F., Jannuzi, B. T., Liebert, J., Smith, P. S. & Fink, H., 1993, AJ, 106, 1729

[] Fossati, G., 2001 in "Blazars demogrphics and physics", ASP Conference Series, ??, ??, ed. P. Padovani & M.C. Urry (astro-ph/0009388)

[] Giommi, P. & Paolo, P., 1994, MNRAS, 268, L51

[] Giommi, P., Menna, & Padovani, P., 1999, MNRAS, 310, 465

[] Giommi, P., Pellizzoni, A., Perri, M. & Padovani, P., 2001, in "Blazars demogrphics and physics", ASP Conference Series, ??, ??, ed. P. Padovani & M.C. Urry (astro-ph/0012075)

[] Green et al. 1986

[] Hook, I. M., McMahon, R. G. & Shaver, P. A., 1999, in "Looking Deep in the southern sky", ed. R. Morganti & W. J. Couch (Heidelberg: Springer-Verlag), 211

[] Jackson, C. A. & Wall, J. V. 2001, in "Blazars demogrphics and physics", ASP Conference Series, ??, ??, ed. P. Padovani & M.C. Urry (astro-ph/0012075)

[] Laurent-Meuhleisen ???

[] Marchã, M. J. M., Browne, I. W. A., Impey, C. D., Smith, P. S., 1996, MNRAS, 281, 425

[] Moles, M., García-Pelayo, J. M., Masegosa, J. & Aparicio, A., 1985, ApJS, 58, 255

[] Nonino, M. et al., 1999, A&AS, 137, 51

[] Padovani, P. & Urry, C. M., 1992, ApJ, 387, 449

[] Padovani, P. & Giommi, P. 1995, ApJ, 444, 567

[] Padovani, P., 1997, in "Very high energy phenomena in the Universe", ed. Y. Giruaud-Héraud & J. Trân Thanh Vân (Paris: Ed. Frontières), 7

[] Padovani, P., 2001, in "Blazars demogrphics and physics", ASP Conference Series, ??, ??, ed. P. Padovani & M.C. Urry (astro-ph/0012355)

[] Perlman, E. S., et al. 1996, ApJS, 104, 251

[] Rector, T. A., Stocke, J. T. Perlman, E. S., Morris, S. L. & Gioia, I. M., 2000, ApJ in press (astro-ph/0006215)

[] Sambruna, R. M., Maraschi, L. & Urry C. M., 1996, ApJ, 463, 444

[] Shaver, P. A., Wall, J. V., Kellermann, K. I., Jackson, C. A. & Hawkins, M. R.S., 1996, Nature, 384, 439

[] Stickel, M., Padovani, P., Urry, C. M., Fried, J. W., & Kühr, H., 1991, ApJ, 374, 431

[] Stickel M., Meisenheimer K. & Kuhr H., 1994, A&AS, 105, 211

[] Stocke, J. et al. 1991, ApJS, 76, 813

[] Urry, C. M. & Padovani P., 1991, ApJ 371, 160

[] Urry, C. M. & Padovani, P., 1995, PASP, 107, 803

[] Wall, J. V. & Peacock, J. A., 1985, MNRAS, 216, 173

[] Wolter, A., 1994

[] Wolter, A. & Celotti, A., 2001 ????

[] Zaggia, S. et al. 1999, A&AS, 137, 75

[] Abbott, M. et al. 1996, ApJS, 107, 451

[] Bevington, P. R., 1969, "Data reduction and error analysis for the physical sciences", New York: McGraw-Hill

[] Bowyer, S.& Malina, R. F., 1991, in Extreme Ultraviolet Astronomy, ed. R.F. Malina & S. Bowyer (New York: Pergamon Press), 397

[] Brinkmann, W. et al, 2001, A&A, 365, 162

[] Brinkmann, W. et al. 1994, A&A, 288, 433

[] Buckley, J. H. et al. 1996, ApJ, 472, 9

[] Canizares, C. R. & Kruper, J., 1984, ApJ, 278, 99

[] Celotti, A., Maraschi, L. & Treves, A., 1991, ApJ, 377, 403

[] Chatfield, C., 1989, "The analysis of time series: an introduction", Chapman and Hall

[] Chiaberge, M. & Ghisellini, G., 1999, MNRAS, 306, 551

[] Deeming, T.J., 1975, Ap&SS, 36, 137

[] Elvis, M., Wilkes, B. J. & Lockman, F. J., 1989, AJ, 97, 777

[] Fossati, G. et al., 2000, ApJ in press**update this!**

[] Fossati, G. et al., 2000, ApJ in press**update this!**

[] Fossati, G., & Haardt, F. 1997, Scientific Report on Low Energy Absorption Features Detected by BeppoSAX LECS in Bright Blazar Targets. Rept. no. Ref. SISSA 146/97/A; preprint (astro-ph/9804282)

[] Fruscione, A. 1996, ApJ, 459, 509

[] Fruscione, A., Bowyer, S., Konigl, A. & Kahn, S. M., 1994, ApJ, 422, 55

[] Fruscione, A., Bruhweiler, F., Cheng, K.P., Hall, C.R., Kafatos, M., Ramos, E. & Kondo, Y., 1996, in UV and X-ray Spectroscopy of Astrophysical and Laboratory Plasmas, ed. K. Yamashita & T. Watanabe (Tokyo: Universal Academic Press), 351

[] Georganopoulos, M. & Marscher, A. P., 1998, ApJ, 506, 621

[] George, I.M., Warwick, R. S. & Bromage, G. E., 1988 MNRAS 232, 793

[] George, I. M., Warwick, R. S. & McHardy, I. M., 1988, MNRAS, 235, 787

[] Ghisellini, G., 1989, MNRAS, 236, 341

[] Ghisellini, G. Maraschi, L. & Treves, A., 1985, A&A 146, 204

[] Giommi, P., Barr, P., Garilli, B., Maccagni, D. & Pollock, T., 1990, ApJ, 356, 432

[] Giommi, P. et al. 1998, A&A, 333, L5

[] Guainazzi, M., Vacanti, G., Malizia, A., O'Flaherty, K. S., Palazzi, E. & Parmar, A. N., 1999, A&A, 342, 124

[] Hettrick, M.C. & Bowyer, S., 1983, Appl. Opt., 3921

[] Kartje, J.F., Konigl, A., Hwang, C.Y. & Bowyer, S., 1997, ApJ, 474, 630 (K97)

[] Kerrick, A. D. et al. 1995, ApJ, 438, 59

[] Konigl, A., Kartje, J. F., Bowyer, S., Kahn, S. M. & Hwang, C.-Y., 1995, ApJ, 446, 598

[] Konigl, A., 1989, ApJ, 340, 162

[] Krolik, J. H., Kallman, T. R., Fabian, A. C. & Rees, M. J., 1985, ApJ, 295, 104

[] Macomb, D. J. et al. 1996, ApJ, 459, L111

[] Macomb, D. J. et al. 1995, ApJ, 449, 99

[] Madejski, G. M., Mushotzky, R. F., Weaver, K. A., Arnaud, K. A. & Urry, C. M., 1991, ApJ, 370, 198

[] Madejski, G. M. et al. 1994, in "BBXRT, a preview to astronomical X-ray spectroscopy in the 90's", ed. P. Serlemitsos & S. J. Shrader, Greenbelt: NASA, 63

[] Madejski, G. M., Takahashi, T., Tashiro, M., Kubo, H., Hartman, R., Kallman, T. & Sikora, M., 1996, ApJ, 459, 156

[] Makino, F. et al. 1987, ApJ, 313, 662

[] Malina, R. et al. 1994, AJ, 107, 751

[] Maraschi, L. et al. 1999, ApJ, 526, L81

[] Marshall, H. L., Fruscione, A. & Carone, T. E., 1995, ApJ, 439, 90

[] Marshall, H. L. et al. 1999 in preparation

[] Mastichiadis, A. & Kirk, J. G., 1997, A&A, 320, 19

[] Maza, J., Martin, P. G. & Angel, J.R.P., 1978, ApJ, 224, 368

[] Morrison, R. & McCammon, D., 1983, ApJ, 270, 119-122

[] Mufson, S.L., Hutter, D.J. & Kondo, Y., 1989, in "BL Lac Objects": proceedings of a workshop held in Como, Italy, September 20-23, 1988. Editors, L. Maraschi, T. Maccacaro, M.-H. Ulrich; Publisher, Springer-Verlag, Berlin, New York, NY, 1989, p.341

[] Mufson, S.L., Hutter, D.J., Kondo, Y., Urry, C. M. & Wisniewski, W. Z., 1990 ApJ, 354, 116

[] Mushotzky, R. F., Boldt, E. A., Holt, S. S. & Serlemitsos, P. J., 1979, ApJ, 232, 17

[] Nicastro F., Fiore F. and Matt G., 1999, ApJ, 517, 108

[] Nicastro F., Elvis M., Fiore F., Matt G. and Savaglio S., 2000, Proceedings of the "X-ray Astronomy '99", 1999, September 6-10, Bologna, Italy, astro-ph/0007050

[] Nicastro, F. , Fruscione, A., Elvis, M., Siemiginowska, A., Fiore, F. & Bianchi, S., 2001, proceeding of the "X-Ray Astronomy 2000" conference (Sept. 2000, Palermo, Italy), PASP Conference Series, ed. R. Giacconi, L. Stella and S. Serio, astro-ph/0102455

[] Papadakis, I. E. & Lawrence, A., 1993, MNRAS, 261, 612

[] Papadakis, I. E. & Lawrence, A., 1995, MNRAS, 272, 161

[] Pounds, K. A. et al. 1993, MNRAS, 260, 77

[] Punch, M. et al. 1992, Nature, 358, 477

[] Pye, J. P. et al. 1995, MNRAS, 274, 1165

[] Richetts et al. 1976, Nature, 259,546

[] Rumph, T., Bowyer, S. & Vennes, S., 1994, AJ, 107, 6, 2108-2114

[] Sambruna, R. M., Barr, P., Giommi, P., Maraschi, L., Tagliaferri, G. & Treves, A., 1994, ApJS, 95, 371

[] Sambruna, R. M. et al. 1997, ApJ, 483, 774

[] Sambruna, R. M. & Mushotzky, R. F., 1998, ApJ, 502, 630

[] Simonetti, J.H., Cordes, J.M. & Heeschen, D. S., 1985, ApJ, 296, 46

[] Sirk, M.M., internal EUVE memo MMS/EUVE/0084/94

[] Sirk, M.M., Vallerga, J.V., Finley, D.S., Jelinsky, P. & Malina, R.F., 1997, ApJS, 110, 347

[] Tagliaferri, G., Stella, L., Maraschi, L., Treves, A., & Celotti, A., 1991, ApJ, 380, 78

[] Takahashi, T et al. 1996a, 1996, ApJ, 470, 89

[] Takahashi, T. et al. 1996b, Mem. SaIt. 67, 533T

[] Takahashi, T., Madejski, G. & Kubo, H., 1999, ApJ, 11, 177

[] Takahashi, T. et al. , 2000, ApJ, 542, L105

[] Tashiro, M., Makishima, K., Ohashi, T., Inda-Koide, M., Yamashita, A., Mihara, T. & Kohmura, Y., 1995, PASJ, 47, 131

[] Ulrich, M.-H., Kinman, T. D., Lynds, C. R., Rieke, G. H., & Ekers, R. D 1975, ApJ, 198, 261

[] Urry, M. C. & Padovani, P., 1995, PASP, 108, 803

[] Welsh, B.Y., Vallerga, J.V., Jelinsky, P., Vedder, P.W., Bowyer, S. & Malina, R.F., 1990, Opt. Eng., 29, 752

[] Zhang, F. J. & Baath, L. B., 1990, A&A, 236, 47

[] Zhang, Y. H. et al. 1999, ApJ, 527, 719

[] Zweerink, J. A. et al. 1997, ApJ, 490, 141

AGN Active Galactic Nucleus
BLEIS BLazar - ESO Imaging Survey
DXRBS Deep X-ray Radio Blazar Survey
EIS ESO Imaging Survey
EMSS Einstein Medium Sensitivity Survey
ESO European Southern Observatory
FSRQ Flat Spectrum Radio Quasar
HFSRQ High energy peaked Flat Spectrum Radio Quasar
IR Infra Rosso
LMSy2 Low Mass Seyfert 2
REX Radio Emitting X-rays
SED Spectral Energy Distribution
SSRQ Steep Spectrum Radio Quasar
QSO Quasi Stellar Object
UV UltraViolet